Developing Computational Tools to Investigate Stress Granules In-vivo

CARL MATTHEW JONES

Developing Computational Tools to Investigate Stress Granules *In-vivo*

Carl Matthew Jones

A thesis submitted for the degree of Doctor of Philosophy

Department of Biosciences

Durham University

December 2020

Developing Computational Tools to Investigate Stress Granules *In-vivo*

Carl Matthew Jones

Abstract

The classical picture of an organelle is membrane-bound and stable, but in recent years we have been able to identify a number of membraneless organelles that may be dynamically assembled and disassembled in response changes in the cellular environment. These condensates exhibit liquid-like behaviour and as such, can flow and merge. Despite this seemingly transient nature, these membraneless organelles perform a complex role in the cell, and in several instances, these roles may depend on the interactions between several species of membraneless organelle. Stress granules are such an example and arise from liquid-liquid phase separation triggered by oxidative, temperature or osmotic stress. Stress granules are composed of RNA and proteins that condense out of the cytoplasm. While stress granule composition and function has been a subject of intense work recently, many biophysical aspects remain poorly characterised. In this work, we present two computational tools that are backed by state-of-the-art microscopy data. The first is a reaction-diffusion based model of granule formation and growth that accurately captures the count and size distribution of granules throughout the cell with time, providing us with insight into the dynamics of granule assembly.

Secondly, we introduce flicker spectroscopy as a method to measure the surface tension of granules in live cells directly and apply it to stress granules induced by different chemicals and genetic backgrounds. The measured surface tensions agree well with the current estimates used in the literature. Additionally, we quantify bending rigidity across the surface of the droplet, which to our knowledge has not yet been characterised for cellular droplets.

Finally, we present an open-source, user-friendly software package for performing flicker spectroscopy, to encourage the application of this method to other biological condensates.

Table of Contents

Acknowledgements . . . vi
Statement of Copyright . . . vii
Publications . . . viii
Glossary . . . x
Symbols . . . xi

1 Introduction

1.1 Organisation and Structures in Biology . . . 3
1.1.1 Liquid-liquid phase separation . . . 4
1.1.2 Role in the cell . . . 6
1.1.3 Conditions for LLPS . . . 7
1.1.4 Formation of stress granules . . . 12
1.1.5 Composition . . . 14
1.1.6 Internal structure . . . 14
1.1.7 Time evolution of biological compartments . . . 17
1.1.8 Dissolution of granules . . . 19
1.1.9 Thesis aims . . . 20

2 Materials and Methods

2.1 Cell Culture and Imaging . . . 23
2.1.1 Maintaining cells . . . 23
2.1.2 Stressing cells . . . 24
2.1.3 Image acquisition . . . 25

2.2 Image Analysis . . . 31
2.2.1 Locating granules . . . 31
2.2.2 Estimation of granule shape . . . 34

3 Modelling Granule Growth

3.1 A Model to Describe Granule Growth and Formation . . . 39
3.1.1 Potential Models . . . 39
3.1.2 Implementation . . . 41

3.2 Results **49**
3.2.1 Exploring the parameter space 49
3.2.2 Attrition modes 52
3.2.3 Biased Walks 55
3.2.4 Attrition scaling 56

3.3 Discussion **59**
3.3.1 Similar packages for modelling reaction-diffusion 59
3.3.2 Model conclusion 59
3.3.3 Future Directions 60
3.3.4 Use in Vietri et al. 61

3.4 Appendix to Chapter 3 . . . . . **63**
3.4.1 Generating random points on disks and spheres 63
3.4.2 Implementing Vetri et al. 66

4 Measuring Stress Granule Properties Using Flicker Spectroscopy

4.1 Theoretical Description of Shape Fluctuations of LLPS Droplets **71**
4.1.1 Measuring surface tension 72
4.1.2 Flicker Spectroscopy 73
4.1.3 Outline 78

4.2 Verification of the Flicker Spectroscopy Method for Applications in LLPS droplets **79**
4.2.1 Simulating a fluctuating droplet 79
4.2.2 Rotation of rigid bodies 88
4.2.3 Fixed cells 94

4.3 Image Analysis **97**
4.3.1 Edge Detection 97
4.3.2 Measuring properties 104

4.4 Granule Explorer **111**
4.4.1 Features of the package 111
4.4.2 Reproducible research 115
4.4.3 Publishing the package 117

4.5 Experimental Results **119**
4.5.1 The base shape of the stress granule must be accounted for 119
4.5.2 Surface tension alone is not enough to explain granule shape 121
4.5.3 Comparison between granule treatments 122
4.5.4 Additional treatments 123

4.6 Discussion **129**
4.6.1 Comparison to current estimates 129
4.6.2 Sources of bending rigidity 130
4.6.3 Possible improvements 130
4.6.4 Limiting factors in data acquisition 131
4.6.5 Conclusion 132

4.7 Appendix to Chapter 4 . . . . . **135**
4.7.1 Spectrum derivation for a flat interface 135
4.7.2 Stencils 138
4.7.3 Supplementary figures 140

5 Discussion

6 Appendix

A Conventions **149**
A.1 Spherical Coordinates 149
A.2 Spherical Harmonics 149

Bibliography **151**

Acknowledgements

Firstly, I would like to thank my supervisors, Sushma Grellscheid and Halim Kusumaatmaja. Their combined expertise and support were invaluable in overcoming the challenges such an interdisciplinary project presents, and making this PhD such a worthwhile experience.

I'd also like to thank: Maha Al-Rushadi, Tom Stevenson, Linda Hjørnevik and too many others to list, for helping a somewhat clueless theoretician navigate a biology lab, and dealing with all the question and difficulties that entails. Tim Hawking, Joanne Robson at Durham along with Hege Dale at the MIC, Bergen for their help with sorting out all of the microscopy challenges I could bring them. David Dolan for his *unerring encouragement* for me to finish this thesis.

I also want to include everyone at the Computational Biology Unit at Bergen for being such a wonderful environment to work in for these last two years. Finally, I would like to thank my parents, as without their support throughout the years, none of this would be possible.

Statement of Authorship

I certify that all work described in this thesis is my own research unless otherwise acknowledged in the text or by references and has not been previously submitted for a degree in this or any other university.

This work was supervised by Sushma Grellscheid at the Department of Biosciences and Halim Kusumaatmaja at the Department of Physics.

Statement of Copyright

Publications

Publications arising from work in this thesis

- Carl Jones, Sushma Grellscheid, Halim Kusumaatmaja "A reaction diffusion based model for granule growth" This paper contains the work discussed in Chapter 3. *Manuscript available upon request.*

- Carl Jones, Thomas M. Stevenson, Matthew Turner, Halim Kusumaatmaja, Sushma Grellscheid "Fluctuation analysis of in-vitro condensates" This paper contains the work discussed in Chapter 4. *Manuscript available upon request.*

- Marina Vietri, Sebastian W. Schultz, Aurélie Bellanger, Carl M. Jones et al. "Unrestrained ESCRT-III drives micronuclear catastrophe and chromosome fragmentation", *Nature Cell Biology*, **22** (2020).
  The author made major contributions to this work, performing the in-silico experiments which relied on the extension of Chapter 3.

Other Works

- Carla B. Mellough, Roman Bauer, Joseph Collin, Birthe Dorgau, Darin Zerti, David W. P. Dolan, Carl M. Jones, et al. "An integrated transcriptional analysis of the developing human retina", *Development*, **146** (2019).

- Katarzyna Chyżyńska, Kornel Labun, Carl Jones, Sushma N. Grellscheid, Eivind Valen. "Deep conservation of ribosome stall sites across RNA processing genes". *NAR Genomics and Bioinformatics*, **3** (2021)

Glossary

Liquid-liquid phase separation The reversible un-mixing of a fluid into two or more separate phases.

Biomolecular condensate Small droplets within the cell that are typically enriched in specific proteins and mRNA, that arise from LLPS. Also know as **membraneless organelles**.

Growth An initial stage of LLPS where the mean size of granules increases as material is sequestered from the background cytoplasm into the droplets.

Coarsening A later stage of LLPS where the mean size of granules continues to grow despite depleting available material from the cytoplasm.

Translation The synthesis of proteins inside a cell. Information from genes in the DNA is transcribed into messenger RNA, which are then translated by ribosomes into proteins..

mRNP Messenger ribonucleoprotein: A mixture of mRNA bound to protein.

Polysomes During translation, many ribosomes may attach to a single mRNA in a structure known as a polysome or polyribosome.

Confocal microscopy An optical microscopy technique, where a pin-hole aperture is placed to block light between the sample and sensor. This serves to block out-of-focus light from the sample, increasing resolution and the imaging of a single thin cross section of the sample.

Fluorophore A protein or chemical compound that emits light after excitation via higher frequency light. An example fluorophore used commonly in this work GFP (Green fluorescent protein). Flourophores are bound to a protein of interest and then imaged via microscopy.

Laser scanning microscope A class of confocal microscope where a raster image is created by scanning a laser across the sample pixel by pixel..

z-stack It is convention in confocal microscopy that the imaging plane is given as the xy plane. A 3d view of the sample may be created by taking multiple images along the z-axis.

Commonly used symbols and constants

k_B	**Boltzmann constant**: for a system at temperature T, each degree of freedom carries an energy $k_\mathrm{B}T/2$. $k_\mathrm{B} = 1.380\,649 \times 10^{-23}\,\mathrm{J/K}$.
F	**Free energy**: the energy available to the system to do work $F = E - TS$.
κ	**Bending rigidity**: the energy required to change the curvature of the surface away from its spontaneous curvature.
$\bar{\sigma}$	**Reduced surface tension**: a dimensionless parameter derived from the surface tension, $\bar{\sigma} = \sigma R^2/\kappa$.
σ	**Surface tension**: an energy penalty per unit area for the interface between two unfavourable regions.
T	**Temperature**: Assumed to be $310.15\,\mathrm{K} = 37\,^\circ\mathrm{C}$ unless stated otherwise.
$\mathcal{U}_{l,m}$	**3D perturbation magnitudes**: the strength of the corresponding spherical harmonic, $Y_{l,m}$, term in the granule surface.
$u(\theta, \phi, t)$	**Surface Perturbation**: the distance between the granule surface, S, and a uniform sphere at a given angle (θ, ϕ) and time t.
$\mathcal{V}_q$	**2D perturbation magnitudes**: the strength of the q mode in the observable granule on the imaging plane. Can be separated into fluctuating $\mathcal{F}_q$ and constant components $\mathcal{C}_q$.
$Y_{l,m}$	**Spherical harmonics of degree l and order m**: A linear combination of these functions allows us to describe a 3d stress granule. Normalisation and angle convention given in sec. A.2.

Chapter 1

Introduction

1.1 Organisation and Structures in Biology

Biology is a story of many scales and levels of complexity. In the central dogma of molecular biology, DNA in the nucleus contains all of the information required to make an organism by encoding instructions to make proteins; this information is then transcribed onto messenger RNA and brought to ribosomes in the cytoplasm where they are translated into proteins. Clusters of these proteins form protein complexes which then build organelles, which form the cells, tissues and eventually full organisms.

Each of these steps represents an emergent behaviour: organelles perform a wide variety of roles in the cell, far beyond what is possible in any single protien complex. The structure and organisation of these proteins is what allows for this complex behaviour, and is arguably what separates living systems from simple chemistry.

In this work, we focus on organelles, these are small subcompartments in the cell that perform specific functions. The classical model of a cell is based around membrane-bound organelles, the most prominent examples of which are the nucleus, endoplasmic reticulum and mitochondria [1, 2]. The membrane provides both structure and clear division between the organelle and the surrounding cytoplasm, providing a mostly impermeable barrier between the organelle and its surroundings, with the flow of material controlled by transport machinery.

However, there have been numerous cellular compartments identified that do not have a membrane. In the literature, these are referred to as biological condensates or memebraneless organelles. The first of these regions was observed in the 1830s in the nucleus, but it would be another century before it was recognised as the nucleolus [3, 4]. Over the last two decades, there has been a renewed interest in these compartments, with many other examples discovered in both the cytoplasm and the nucleus, including stress granules [5], P bodies [6] and Cajal bodies [7]. In fig. 1.1.1 we include a cartoon of the currently identified compartments in the cell. We find that the proteins in these compartments typically have some common features such as RNA recognition motifs and intrinsically disorderd regions that are covered more in section 1.1.5.

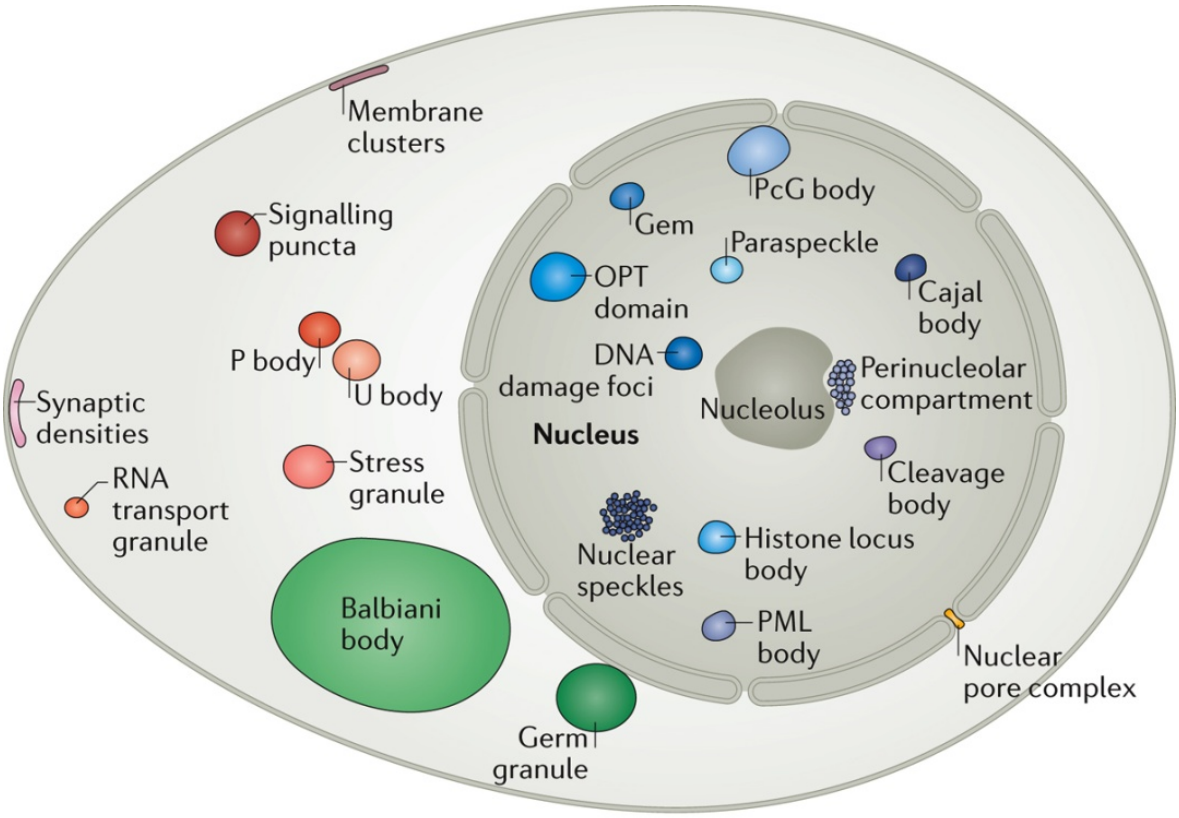

Figure 1.1.1: Cartoon of LLPS condensates found within the cell. Some condensates occur only in specific cell types. In this work we are focused primarily on stress granules. From [8].

Membraneless organelles can be created dynamically by the cell and can last for hours or even days, before mixing back mix into the surrounding material once the conditions for their formation have ended [8]. The most pressing questions at the time when these condensates were discovered were how these compartments remain separated from the rest of the cell, despite the lack of membrane and what biological role these compartments play in the cell.

1.1.1 Liquid-liquid phase separation

The nature of these compartments remained poorly characterised until seminal work by Cliff Brangwynne, Tony Hyman and Michael Rosen demonstrated that these compartments behave as liquid droplets rather than solid entities [9, 10, 11]. It has been shown that organelles continuously change shape and can flow when force is applied [12]; two organelles can coalesce into single larger droplet [13] and they can wet on surfaces on the cell [9]. Photo-bleaching experiments have revealed, that unlike the membrane-bound organelles, they are in dynamic equilibrium and rapidly exchange material both internally and with the surrounding area [9, 8, 14].

This behaviour demonstrated that these compartments are an LLPS (liquid-liquid phase separation) system: two (or more) liquid species that spontaneously separate from each other. These systems are prevalent in both organic and inorganic systems, with the most commonly known example being oil in water (or vinegar in olive oil). Fundamentally, LLPS is the phenomenon of particles self-organising in order to minimise the free energy of the system. This self-assembly is responsible for not only membraneless organelles, but also the lipid bilayer membranes and more complex structures such as vaults and viruses [15]. The oil and water system separates as the water molecules are strongly bound to other water molecules, and similarly, the oil molecules can interact through van der Waals forces along the length of the long tails. However, there are no meaningful bonds between the oil and water molecules. This means it is energetically favourable to maximise the water-water and oil-oil contact in order to minimise the oil-water contact, and this is achieved by oil and water separating into droplets.

This idea of separation generalises well to other systems, and a useful way to rationalise this by considering the so-called free energy, F, [16, 17],

$$F = E - TS \ , \tag{1.1.1}$$

where E is the internal energy of the system, T is the temperature and the entropy S. The internal energy of the system, E, is given by the sum of the interactions between the particles. In complex systems of many components, it may be non-trivial or even impossible to form an analytical solution. However, if for now, we only consider a simple system of two components A and B then we have only three pairs of interactions to consider: the similar pairs AA, BB and the interactions between mixed pairs AB, with energy E_{AA}, E_{BB} and E_{AB} respectively. It is convention that the interactions energies between particles are given as a negative value, with stronger bonds having more negative energy, and so is favourable, as we might expect.

The condition for unmixing is that the change in free energy of unmixing is negative, $\Delta F_{\text{unmxing}} < 0$. This change is energy is given by,

$$\Delta F_{\text{unmixing}} = F_{\text{unmixed}} - F_{\text{mixed}} \tag{1.1.2a}$$

$$\Delta F_{\text{unmixing}} = E_{\text{unmixed}} - E_{\text{mixed}} - T\Delta S_{\text{unmixing}} \ . \tag{1.1.2b}$$

Usually, the entropy will be higher in a mixed system $\Delta S_{\text{unmxing}} < 0$, and so favour mixing.

Naturally, when unmixing, we increase the number of bonds between the same components and decrease the number of bonds between the opposite pairs.[1] If the AB interactions are stronger than the AA and BB interactions, then both the enthalpy and entropy favour mixing, so the system will mix in all cases.

Of more interest are the cases when the interactions between the same pair interactions are stronger than the unlike pair, as this sets up a balance between the entropy and internal energy that allows the system to unmix and phase separate under certain conditions. In the separated system this leaves an interface between the two regions, for which there is still an energy penalty. The energy cost per unit area for this contact is defined as the surface tension, σ. As we explore further we see that surface tension controls much of the dynamics of the droplets and the interactions between other species of biological compartments.[2] Relating this to our oil and water example, there is strong hydrogen bonding between the water molecules, E_{AA}, and van der Waals interactions between the long oil molecules, E_{BB}, but only very weak interactions between the two, E_{AB}. At room temperature, this dominates over the entropy, and the oil and water will separate.

Equation (1.1.2b) implies that increasing the temperature of the system increases the contribution from the entropy term and so encourages mixing. This is not often considered in eukaryotic cells, as they are typically held at a regulated temperature by the organism and will suffer deleterious effects with relatively small changes in temperature. However, it has been demonstrated by Lee and Putnam that increasing the temperature from 20 °C to 30 °C in *C. elegans* embryos will cause the dissolution of already formed P granules [18, 19]. This highlights another important factor of LLPS compartments, that once the conditions for their formation are removed they mix back into the cytoplasm.

1.1.2 Role in the cell

We see in the above section that condensates serve to draw a given component into a small area, which can lead to a tremendous increase in the concentration of the component, that can reach as high as 3,000 fold. In this section, we consider the effects of this compartmentalisation and how it may be advantageous in the cell.

1. We make a number of simplifications here. For instance, there is some complexity due to the number of interactions between each of the particles.
2. In a liquid-liquid system, the contact region is better characterised as an interface, rather than a surface. Meaning that interfacial tension is a more apt term than surface tension; however, surface tension is the more prevalent term in the literature, and we will continue to use it in this work.

We find that compartments serve three primary roles. The most apparent consequence of which is as a reaction crucible [20]. Standard reaction kinetics (or enzyme-based Michaelis-Menten kinetics) predicts that increasing the concentration of reactants in this manner would lead to a corresponding increase in reaction rate. This allows reactions that were previously prohibitively slow, due to the sparse components, to proceed in a robust manner.

A second consequence is that compartments may draw material away from regions where they may have unwanted or deleterious effects. Thedieck, Grellscheid et al. illustrated that stress granules inhibit the mTORC1 pathway required for translation by sequestering key mTORC1 components, which aids translational arrest [21].

Finally, these membraneless organelles provide a means for the cell to organise material and reactions [22]. In a case of particular interest, *C. elegans* localises the formation of P granules to the posterior of the cell by setting up a concentration gradient of Mex-5, a protein that favours P granule dissolution [9, 11]. As a further example, the membraneless organelle, the centrosome, can only nucleate around a centriole. So by only creating a pair of centrioles, the cell is able to limit the number of centrosomes formed.

1.1.3 Conditions for phase separation

The cell has some mechanism for controlling when and where the compartments form, so let us now consider the conditions required for compartment formation and how the cell might exploit them. We have seen two different ways in which phase separation is triggered. Centrosomes are an example of the first case, where there is a external nucleation site that is required. P bodies are example of the second, where only a change in concentration is required for formation.

In non-biological LLPS systems, the temperature of the system is also a significant factor in phase separation, but as already covered, this typically remains fixed in a biological system. Conversely, in many in-vitro systems we can assume that concentration of components is fixed, but in a cell, there are numerous active processes occurring that may change the concentration of the phase separating components.

Let us now consider what LLPS theory allows us to predict about condensate formation. We see that eq. (1.1.2b) gives a condition for compartments to form, but besides the temperature dependence, it does not give much insight into how external nucleation or concentration changes will lead to formation, so we instead make use of the Cahn-Hillard model. This is a powerful theoretical model that captures the basic essence of many (binary) phase separating systems.

We start by giving a convenient notation for describing the concentration of material at a point. If, for now, we have two components A and B we define an order parameter $\phi \equiv \frac{[A]-[B]}{[A]+[B]}$ so that $\phi = 1$ for a pure A region, $\phi = -1$ for a pure B region and $\phi = 0$ corresponds to an equally mixed region. We then give the total energy of the system, F, as,

$$F[\phi] = \int \left(f(\phi) + \frac{K}{2}(\boldsymbol{\nabla}\phi)^2 \right) \mathrm{d}\vec{\mathbf{r}} \ , \tag{1.1.3}$$

where $f(\phi)$ is the free energy per unit volume at a given point in the system and, as we shall see, the $(\boldsymbol{\nabla}\phi)^2$ term corresponds to an energy penalty—leading to to the notion of surface tension, σ—at the interface between the regions [23]. K is a parameter controlling the magnitude of this effect.

A oft-used description of the free energy is given by,

$$f(\phi) = \phi \ln \phi + (1-\phi)\ln(1-\phi) + \chi\phi(1-\phi) \ , \tag{1.1.4}$$

the first two terms are the entropy contribution and the third term is the interaction energy in term of an interaction parameter χ which directly captures difference in energy between mixing or self interaction [15, 24]. However, this form vastly complicates the following derivations, while not offering any greater insight, so instead we preform a Taylor expansion, where we are able to neglect the odd powers by our choice of ϕ to give a simpler form of the free energy [25],

$$f(\phi) \approx \frac{a}{2}\phi^2 + \frac{b}{4}\phi^4 \ . \tag{1.1.5}$$

a is a control parameter related to the energy of the interactions or the entropy of the system. For instance, this may be substituted for temperature, interaction strength, pH or even ATP concentration in a biological system.[3] The ϕ^4 term corresponds to the entropy contribution, with a magnitude parameter b [26].

As the free energy, $f(\phi)$, scales with the volume of the system, this dominates the large scale behaviour of the system. However, we will see that the gradient term, $\boldsymbol{\nabla}\phi$, is also important

3. This is actually far more general than it may seem at first; while this particular form is for a fully symmetric system, in an asymmetric system we are able to transform $\phi \to \phi - c^2/3b$ and $a \to a - c^2/3b$ to remove cubic terms. While this changes the position on the phase diagram, the underlying physics remains the same. Any linear term would just introduce an additive constant to $F[\phi]$ which has no effect on the overall behaviour.

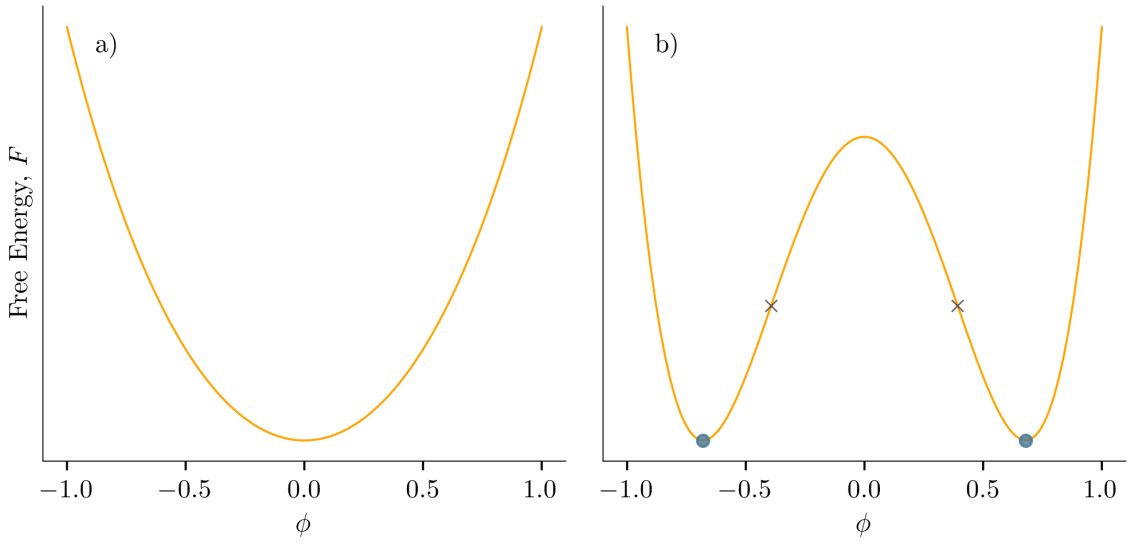

Figure 1.1.2: Free energy of the system given by eq. (1.1.5) depending on the sign of a. In **(a)** mixing is energetically favourable ($a > 0$) there is only a single minima and mixing will always occur. For **(b)** mixing is unfavourable ($a < 0$) causing two minima, given by blue dots, known as binodals and two spinodal points as crosses.

in the evolution of the system.

1.1.3.1 Trivially mixing systems

It is important to explore what eq. (1.1.5) implies in more detail. In a mixed system we start with an average concentration $\bar{\phi}$ and if the system phase separates it will split into two regions: one enriched in A (at concentration $\bar{\phi} + \Delta\phi$) and the other depleted ($\bar{\phi} - \Delta\phi$)[4]. Therefore, to phase separate, the total free energy must decrease.

The first case we will consider is the case where $a > 0$, namely AB pairs are preferred over AA or BB interactions. When we plot the total free energy, F as function of concretion in fig. 1.1.2.a. We see that the lowest energy state is at an even mixture of A and B ($\varphi = 0$). For a system starting here, any increase or decrease in concentration in this region will raise the free energy of the system and so the system will remain mixed.

Furthermore, we find that any starting concentration, $\bar{\phi}$, will be unable to separate. If we start with, say, a system enriched in A $\bar{\phi} > 0$, any small region can reduce its energy by decreasing the local concentration of A, however, the total amount of material in the system must be conserved and so increase the concentration is other regions of the systems. As the

4. In an oil and water mixture the regions may entirely exclude each other; quickly going from an even mixture $\phi = 0$ to two regions: $\phi = +1$ for oil only and $\phi = -1$ for water only. However, in more general cases, the expected concentrations are the binodal points, $\pm\phi_b$, as introduced later, so in general we do not expect that a compartment will entirely deplete its constituents from the cytoplasm.

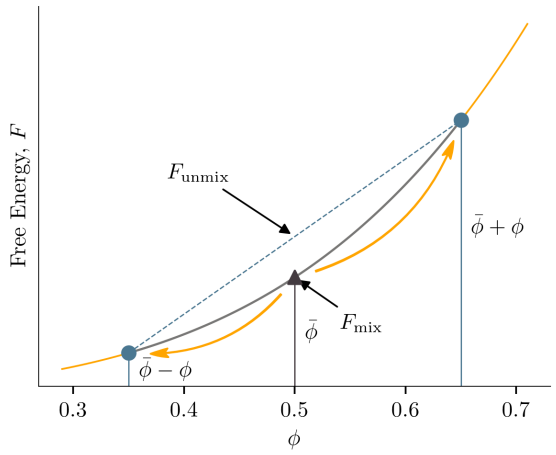

Figure 1.1.3: Demonstration of free energy increase with positive curvature. Upon separation, a starting mixture of $\bar{\phi} = 0.5$ splits into two regions $\bar{\phi} \pm \phi_s$. While the unenriched region at $\bar{\phi} - \phi_s$ is energetically favourable, the corresponding energy increase in the enriched region is greater. The mean energy of the phase separated system is given by the indicated point on the dashed blue line connecting the two points above the starting concentration, and is higher than the energy of the mixed system. Therefore there are no conditions under which this system will separate.

curvature of the free energy is always positive, $\partial^2 f/\partial\phi^2 > 0$, the energy benefit for the reduced region is less than the energy penalty for the corresponding energy cost elsewhere, so the system will always remain mixed. An example of this is shown in fig. 1.1.3, the energy of the mixed system is given by the point on the curve at $\bar{\phi}$ (black triangle), and the total energy of the mixed system is given by the line connecting the two split states at $\bar{\phi} \pm \phi_s$ (blue circles). Regardless of the starting position, the average energy of the two split states will always be higher.

1.1.3.2 Binodal separation

Of more interest are the systems where the mixing is energetically unfavourable, for which, $a < 0$. The *bionodal points*, ϕ_b, are defined to be the points between which it is energetically favourable for phase separation to occur. For the model given in eq. (1.1.5), this corresponds to the condition[5] $f'(\phi_b) \equiv 0$ [26, 15] leading to,

$$\phi_b = \pm\sqrt{-\frac{a}{b}}\,, \tag{1.1.6}$$

and are given as the blue dots in fig. 1.1.2.b. When $|\phi| < \phi_b$, the system is able to phase separate, however this behaviour is divided into two stability regions. These stability regions are defined by the *spinodal points*, the points at which the curvature of the free energy goes from negative to positive, $f''(\phi_s) \equiv 0$. From eq. (1.1.5) these are given[6] as,

$$\phi_s = \pm\sqrt{-\frac{a}{3b}}\,. \tag{1.1.7}$$

5. In general this condition is that $f'(\phi_1) = f'(\phi_2)$, but these conditions are equivalent in our symmetric system.

6. We also make use of the fact that the curvature is negative at the origin: $f''(0) < 0$

and are shown as black crosses in fig. 1.1.2.

Between these two spinodal points, the curvature of the free energy is negative and any un-mixing will lower the free energy yielding a distinctive spinodal decomposition where the entire system will spontaneously split into small enriched or depleted areas that will then coarsens into larger regions.

Outside of these spinodal regions the total energy of the system is lower in a phase separating state, but the mixed state is locally stable against small perturbations. We can interpret this as an "activation energy" or barrier that must be overcome before the system can separate.

In order to start phase separating, there must be a small enriched region that serves as a nucleation site about which the phase-separated region will continue to grow. These sites can be heterogeneous, seeding formation on the surface of some external nucleation site. This provides a mechanism for the cell to organise the compartments within the cell. Examples include centrioles being used to nucleate centrosome formation [27], misfolded proteins can serve as a nucleation site for stress granules [28], with further examples in [29]. Alternatively, the thermal motion of the molecules may happen to create a small enriched region about which formation can continue, in a process known as homogeneous nucleation. However, homogeneous nucleation is much slower than hetrogenous nucleation and provides little means for the cell to control where the compartment is formed. It is a currently open question for most of the compartments in the cell on which of the two nucleation methods are used. We cover this in more detail in section 1.1.5, when discussing the required biological components for stress granule formation and nucleation is a central question in Chapter 3.

By plotting the separation type as a function of starting concentration, $\bar{\phi}$, and control parameter, a, we can create a phase diagram, as shown in fig. 1.1.4. We again note that the control parameter may correspond to different changes in the system enviroment, such as temperature or pH, as indicated on the right axis. In the orange region, the system will undergo binodal separation, and in the inner region, the system will undergo spontaneous spinodal separation. Outside of these regions the system will mix. From the phase diagram we find that there is a critical point (indicated by the critical temperature, T_C in fig. 1.1.4) above which phase separation is not possible.

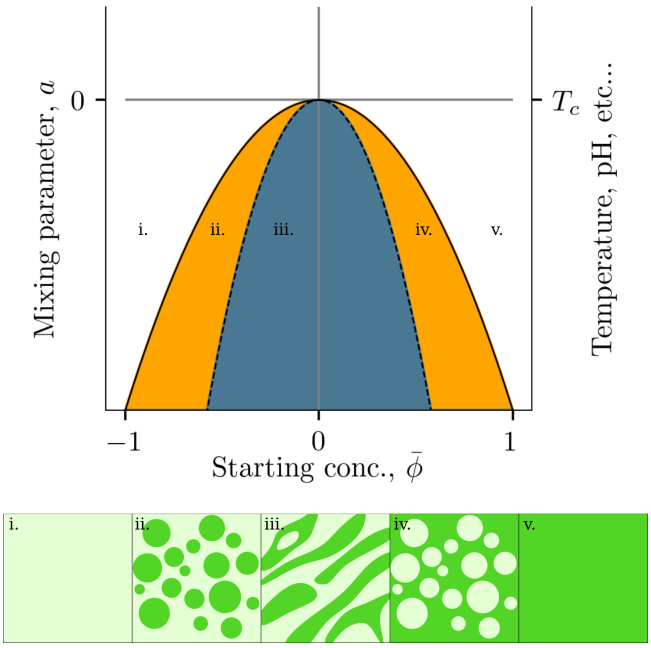

Figure 1.1.4: Phase diagram of a phase separating system, with cartoons of the regions underneath. **(i)** and **(v)** Outside of the coloured regions no phase separation will occur, and the system will remain mixed. This is the case for all systems above the critical temperature T_C. **(ii)** and **(iv)** Inside the solid line is the bionodal region, where the mixture can phase separate around nucleation sites. **(iii)** Within the inner dashed line the system will undergo spontaneous spinodal separation.

1.1.4 Formation of stress granules

Stress granules are the membranesless organelles of particular interest in this thesis. These are pools of mRNA and protein mixture (mRNP) in the cell that separate out from the cytoplasm in response to stress; and once this stress is removed the components mix reversibly back into the cytoplasm. Stress granules were first discovered in 1998 and were initially proposed as simple sites of storage for mRNA transcripts during the stress response and translational arrest.

However, they perform a richer role, Kedersha coined the term "mRNA triage" [12], as granules have been shown to have some mechanism in order to selectively filter for valuable transcripts to remain in the stress granule and while others are passed on for degradation [30]. Intriguingly, this filtering is dependent on the characteristic stress, for instance, transcripts for the heat shock protein HPS27 are not recruited into stress granules during heat stress [31].

Stress granules also exhibit the other two behaviours of general membranes-less organelles discussed in sec. 1.1.2. It has been demonstrated that stress granules can sequester away apoptosis signals to prevent cell death [32, 33], and Takahashi shows stress granule inhibiting reactive oxygen production [34]. Stress granules are frequently found in contact with processing bodies (PB) [30, 35] to enable transcripts to be passed directly from the stress granule to the PBs for degradation. This highlights an example of the organisation and interaction of multiple species of LLPS that will become increasingly important in understanding the role of biological condensates.

The canonical pathway for granule formation is given as follows [31, 36, 37]: in the presence of a stress stimuli the cell will release a relevant serine/theonnie kinase which catalyses the phosporylation of eIF2α at serine 51 [38]. This increases eIF2α's affinity for eIF2B, binding it antagonistically and leaving it unable to form the eIF2-GTP-Met-t_i^{RNA} complex required to place the 43S pre-initiation complex at the start codon [39], and causing translational arrest, leading to polysome disassembly and flooding the cytoplasm with mRNA and hence making phase separation favourable.

Translational arrest serves multiple purposes, the first of which is preserving resources during the stress response, but it also serves as an anti-viral response. Stress granules were first discovered in the context of viral response [40], and this translational lockdown stops the viral hijacking of the translation machinery. Nevertheless, viruses can overcome this attempt, and stress granule formation may be inhibited or even exploited [41, 42], and it is of particularly timely interest that this includes the SARS-CoV-2 [43, 44].

Stress granule formation is "both redundant and adaptable", the canonical pathway discussed above may be adapted depending on the applied stress [28, 45]. As we might expect, it may even be bypassed entirely by directly increasing RNA concentration by triggering polysome disassembly by using eg, puromycin [46] or over-expressing certain stress granule proteins [31, 47].

In the literature, it is typically reported [38, 42, 48] that stress granules begin to form about 15 minutes after the initial stress stimuli. However, there is some ambiguity in this definition, as granules grow from a nucleation site, the granules—and hence the fluorescent tags—would initially form very small and dim puncta that would be indistinguishable from microscopy noise. It is likely that this quoted time merely reflects the time at which the granules have accumulated enough material to be visible via microscopy. More recently, following improvements in the sensitivity and imaging rate of microscopes, small points can be seen forming much before this time as shown by [49] and in our own experimental observations.

It is unclear at what size the stress granules begin to have a biological role in the cell. Interesting paths of investigation are if the composition of mRNA of proteins changes in these proto-granules or when the more advanced RNA triage effects can be observed. In Chapter 4, we investigate the physical properties of granules as a function of granule size, but we are only able to study granules visible by microscopy, and it seems no current method is able to give insight into the structure or composition of these proto-granules.droplets.

1.1.5 Composition

In order to phase separate, there must be a preference for material inside the compartment to bind to other material in the compartment rather than that in the cytoplasm in general. This leads us to ask: What properties do the molecules within the compartments share?

Compartments are mixtures of mRNA and protein. A common factor of proteins related to granule formation are RNA recognition motifs (RRMs) and intrinsically disordered regions (IDRs) [46]. IDRs are areas of seemingly arbitrary sequences that do not produce structured protein regions. Instead, they form weak electrostatic and hydrophobic interactions with other IDR regions [37] that allows for aggregation between identical or other IDR rich proteins [50, 51]. However, we do find that many compartments have a dependency on a given protein, for instance, stress granules formation is consistently suppressed when G3BP is knocked out. G3BP (Ras GTPase-activating protein-binding protein) refers to two proteins, G3BP1 and G3BP2 [47, 52, 53] and even blocking small regions in the proteins, such as the FGDF motif is enough to stop formation [12, 54] .

While there is a great deal of interest in the composition of stress granules in the literature, it can be challenging to get a clear and consistent understanding, due to the seemingly inconsistent nature of the granules. Several proteins have been identified as critical to stress granule formation, however, these may become dispensable in another cell line or under different stress stimuli. TIAR and TIA-1 are a good illustration, as they are required for granule formation under many conditions [46, 55, 56, 57] but stress granules may form still in its absence, for example, under heat shock [58].

There are over 200 proteins that are found to co-locate with stress granules [59, 60], however, as these surveys only reveal which proteins co-locate in granules, it is unclear which of these are functional and which are merely sequestered. Moreover, this is complicated further as the composition of granules varies depending on the resultant stress, such as heat shock, oxidative stress, osmotic stress, nutrient starvation and UV irradiation [61, 62].

1.1.6 Internal structure

Due to the complex composition observed for stress granules, we might expect that the simple two-component theory in sec. 1.1.3 may be unable to describe membraneless organelles fully. A fundamental limitation is that the theory is currently only able to describe uniform

droplets; however, experimentally, we can see instances of ternary structure within membraneless organelles. Germ granules can be seen forming distinct components using phase-contrast microscopy [63]. In a more complex example, Feric et al. showed the three-phase structure of nucleoli in-vivo using microscopy [2], each with a distinct composition and functional role: with the outermost layer responsible for ribosome assembly; the middle layer rRNA processing and the innermost layer handling rDNA transcription.

We can approach modelling this by extending the current model to a three-component system [64], which in this case we might interpret as a background cytoplasm, C, and droplets of species A and B. The interactions of these droplet regions are controlled by the relative surface tension of the regions [20]. With the introduction a new component there are now three surface tensions to consider $\sigma_{AB}, \sigma_{AC}, \sigma_{BC}$, which are the surface tensions between the two droplets and each droplet and the background respectively.

There are several possible cases that we might consider. (i) is the trivial case, if the surface tension between the droplets is higher than the surface tension between either droplet and the cytoplasm, then these droplets will not co-localise. In case (ii), the largest surface tension is between B and C, and so to minimise this contact, the droplet of B will be enveloped by a droplet of A. Naturally, the converse case can occur when A and C is the highest surface tension. It is this scenario that is expected to give rise to much of the structure of complex membraneless organelles. Case (iii) also arises from this extension and occurs when all three surface tensions are similar, in which case the droplets will interact, but not engulf each other.

Case (iii) is a means for the cell to organise distinct membraneless organelles, bringing stress granules and p-bodies together so that the SG may pass transcripts on for degradation [12] or similarly, locating B-snurposomes next to the larger Cajal body, where transciption and processing components are preassembled in the Cajal body, before being transferred. [7]. Schematics of these cases are given in fig. 1.1.5.

This section further illustrates the importance of surface tension in phase separating systems and the importance of tools for measuring it, as we introduce in Chapter 4.

1.1.6.1 Stress granule structure

Two complementary models approach the question of stress granule structure; these are the shell-core and scaffold-client model. Jain et al. proposed the shell-core model which considers the spacial structure of the granules. They propose denser core regions in the granule that are

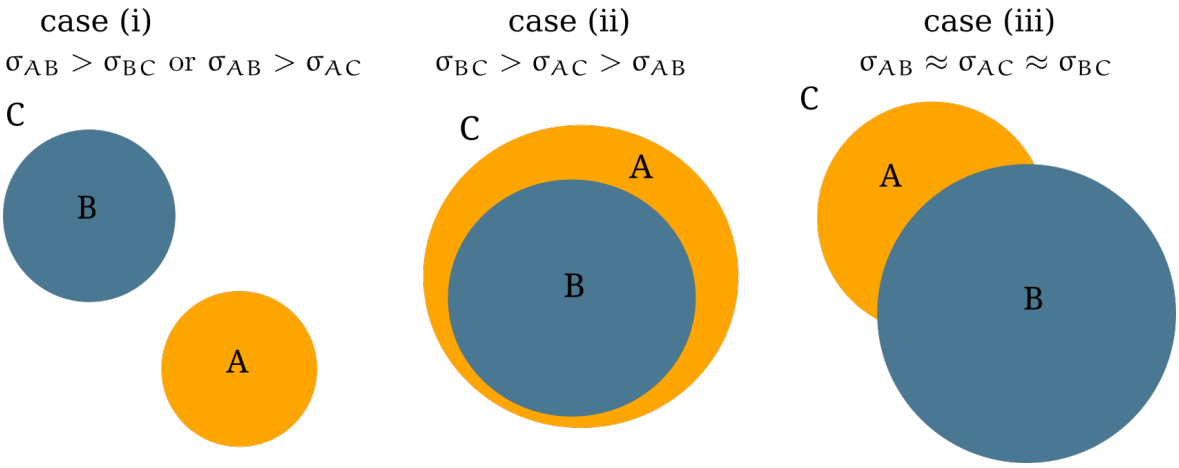

Figure 1.1.5: The relative surface tension between the droplets and the background controls interactions between different droplet species.

surrounded by a less dense shell region [65], and it is motivated by the detection of electron-dense regions within the stress granule during election microscopy [66]. Direct verification of the shell-core model was previously seen as infeasible due to the size of the structures being below the classical diffraction limit of microscopes. Still, a combination of stimulated emission depletion (STED) microscopy for super-resolution imaging and expansion microscopy [67, 68] allowed direct imaging of small regions that contain UBAP2L but not G3BP1 within the granule [69].[7] This is an example of the case (ii) ternary structure given above.

Banani et al. introduced the scaffold-client model to consider the interactions between components within the organelle [70]. The majority of stress granule components, including TIA-1, TIAR and TDP-43 rapidly recover from photobleaching, which suggests that they are exchanged to and from the cytoplasm, [12, 46, 71], however other proteins such as FXR1 do not recover [72]. The slowly recovering proteins are then labelled as a scaffold. Generally, client proteins are largely dispensible for granule formation, whereas scaffolds are required. Not all proteins are divided cleanly into these two groups, however. G3BP1 is commonly required for granule formation, but recovers from photobleaching, albeit slowly and so is typically regarded as a scaffold. Recent work by Shinna [71] attempts to account for this by extending the model to include both "rough" and "smooth" scaffold. The latter is a more mobile scaffold component, and includes G3BP1 and TDP-43 whereas rough components are less mobile and includes components such as FUS, FMR1 and FXR1.

7. STED microscopy is a very powerful super resolution microscopy method, that claims a resolution of 30 nm in comparison to 140 nm for green light in the classical limit using the best lenses currently available. Expansion microscopy isotropically expands the sample in order to make smaller structures visible by STED allowing for a combined resolution that was previously only available by EM.

1.1.7 Time evolution of biological compartments

A point of interest is to investigate how membraneless organelles change with time. In the section 1.1.1 on page 4, we stated that phase separation aimed to minimise the contact between the two separating regions, and while this is achieved well when the system separates out into droplets, the total energy would be minimised further in a single large droplet. While this may be observed in-vitro, it is not seen in living cells. We therefore investigate the mechanisms by which the granules can grow and how these might be limited. A question related to this is: Do biological reactions in the organelle cause a change in the physical properties with time?

1.1.7.1 Growth

Once the nucleation site is formed, the granule will continue to grow by recruiting material from the cytoplasm. This would seem contrary to our intuition of diffusion, where the material is expected to flow from an area of high concentration to one of lower concentration.

The derivative of the free energy, eq. (1.1.5), with respect to concentration, ϕ, gives the chemical potential, $\mu \equiv \delta f/\delta\phi$. The chemical potential is proportional to the energy required to replace a particle of A with a particle of B, it is therefore favourable for particles to flow from an area of high chemical potential to one of lower chemical potential. The rate of material flow, $\vec{\mathbf{J}}$ is proportional to the gradient of the chemical potential $\vec{\mathbf{J}} \propto -\boldsymbol{\nabla}\mu$ [15, 26].

In typical liquid-liquid systems, with mixing components, entropy dominates, and the material flows down the gradient, going from regions of high concentration to low concentration. However, in a phase separating system, the energy term dominates, causing the sign of the chemical potential to switch, $\mu > 0$, and hence drive material in a "reverse diffusion" from areas of low concentration to a higher concentration.

This growth will continue until the material within the cytoplasm reaches a minimal equilibrium level and μ is approximately even across the system. As previously mentioned in sec. 1.1.3.2, this does not necessarily mean that material is entirely depleted in the cytoplasm. This matches our observations from photobleaching, material is still flowing to and from compartments. After this stage, phase separation theory—supported by in-vitro observations—predicts that, despite the no net loss in material from the background, the average size of the droplets will continue to grow in phenomenon known as coarsening, reducing the overall energy penalty for the contact between the droplet and background.

1.1.7.2 Coarsening

The most intuitive mechanism for coarsening is for two droplets to merge—or coalesce—into a single larger droplet. This behaviour is observed in biological compartments, including stress granules, and indeed was one of the behaviours that suggested the liquid-like nature of membraneless organelles. This mechanism is, of course, limited by the ability of the organelles to come into contact with each other; this is less of a problem in-vitro, but the cytoplasm is host to many other structures that may impede the movement of compartments, for instance, the endoplasmic reticulum, cytoskeleton or the nucleus. Moreover, the cytoplasm is incredibly viscous and densely packed with other proteins.

There is also a second mechanism by which droplets may continue to grow: Ostwald ripening, this is a more subtle effect where we find that larger droplets continue to grow at the expense of smaller droplets. If we consider a single droplet, the energy penalty due to surface tension may be reduced by compressing the droplet and directly decreasing surface area. This must be balanced by an increased pressure in the droplet relative to the surrounding region, ΔP, giving us $\Delta P \, \mathrm{d}V = \sigma \, \mathrm{d}A$, which when assume a spherical droplet, gives a pressure difference[8],

$$\Delta P = \sigma \frac{2}{R} \, , \tag{1.1.8}$$

known as the Laplace pressure and causes an increase in chemical potential at the surface of the droplet. As the Laplace pressure is higher for smaller droplets this sets up chemical potential gradients, and therefore a flow of material from small to large droplets, even though, the level of the material in the background remains the same.

This leads to a critical radius, R_c, below which the granule will shrink, and above which the granule will continue to grow. This can be seen by plotting the change of granule radius with time, $\dot{R}$, as a function of radius, R in fig. 1.1.6. We see that this shows a positive-feedback loop: granules that are smaller than the critical radius decrease in size, which further increases the Laplace pressure and the rate of material lost. This process will continue until there is only a single large droplet [26].

Both of these coarsening mechanisms are complementary methods, and Berry et al. demonstrate that the coarsening of nuclei is due to a combination of these effects [24]. These mechanisms are an intrinsic property of LLPS systems, and so we would expect that, according to

8. V, A, R being the volume, area and radius of the spherical droplet respectively.

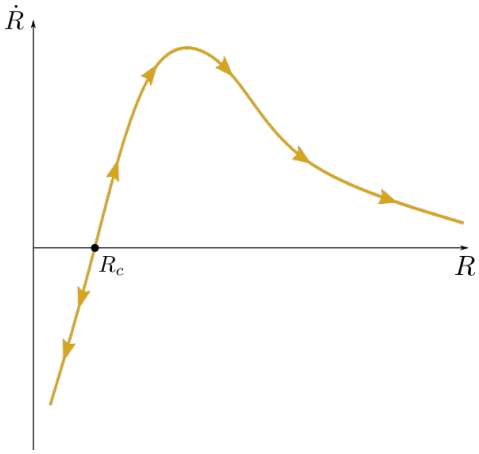

Figure 1.1.6: Rate of granule growth with time, $\dot{R}$, as a functiona of granule size R. Due to Ostwald ripening, granules above a critical radius, R_c will continue to grow, whereas droplets below this size will shrink at their expense.

this theory, that coarsening should be observed in biological compartments as well; however, this has been studied very little in the literature, and so we investigate, how these mechanisms apply to biological systems in Chapter 3 and if some mechanism might be proposed to stop coarsening.

1.1.8 Dissolution of granules

In the theory laid out in sec. 1.1.3, we see that a phase separating system should mix back into the cytoplasm when the conditions for formation are removed. Stress granules formation is reversible once stress stimuli is removed [31], or when polysomes are stabilised, for example, by treatment with emetine [46, 73].

However, LLPS theory does not give a complete picture of stress granule disassembly. Although granules are typically positive for the organism, there have been links between the ability to form stress granules and neurodegenerative diseases such as amyotrophic lateral sclerosis (ALS) and frontotemporal dementia (FTD) [74, 75, 76]. Optogenetic experiments show repeated formation and disassembly of granules can lead to the build up ordered fibril-like regions that are not removed with the rest of the granule, and will continue to aggregate [52]. Work this year by Marmor-Kollet et al. suggests that there is a class of disassembly engaged proteins (DEP) that are required for the dissolution of stress granules, suggesting the aid of other biological mechanisms [72]. In Chapter 3 we model material lost from stress granules back into the cytoplasm and in Chapter 4 we introduce a method to investigate the physical properties of granules as a function of size or time, that may be used study granules as they mature.

1.1.9 Thesis aims

In this thesis, our overall aim is to develop and harness advanced computational tools to improve our understanding of stress granules and biological LLPS systems in general. This is particularly pertinent given recent developments in state-of-the-art microscopy techniques and the datasets they can now generate.

Our first goal is to create an analysis pipeline to reliably extract stress granule characteristics, such as the mean granule area and the number of granules per cell, from our microscopy data, as described in Chapter 2. We further develop these methods for high resolution single granule characterisation in Chapter 4.

In Chapter 3 we develop a simulation approach for the formation and growth of stress granules across the cell. Our corpus of experimental data can be used to refine the model parameters, such as the reaction rate constants, to accurately capture the size and time distributions observed in the cell. By varying the key assumptions in the model and contrasting the outcomes against experimental observations, we further aim to gain insight into the mechanisms underlying granule growth.

Chapter 4 develops flicker spectroscopy as a powerful method to directly measure the surface tension of stress granules in-vivo. We rigorously verify the theory and model implementation, and we apply the method to study stress granules induced by different chemicals and in different genetic backgrounds. We also create an open-source software package to allow other groups to extend this analysis to other LLPS systems.

Finally, in Chapter 5, we discuss the success of these goals, further possible applications of the developed tools, and their potential extensions.

Chapter 2

Materials and Methods

2.1 Cell Culture and Imaging

2.1.1 Maintaining cells

Throughout this work, we will make use of U2OS cells, these are an immortalised cell line taken from a human bone cancer (Osteosarcoma) sample that is a commonly used and well-established line. As we covered in the introductory chapter, G3BP (Ras GTPase-activating protein-binding protein) refers to the proteins G3BP1 and G3BP2, which are regarded as a critical stress granule component, we therefore use G3BP1 as a target for fluorescence tagging. Unless stated otherwise, we use a ΔΔ17-U2OS-GFP-G3BP1 cell line created by Nancy Kederesha. These cells have had endogenous G3BP1, G3BP2a and G3BP2b removed and a fluorescent GFP-G3BP1 added. The endogenous G3BP1 is removed in order to avoid over expression. G3BP2 must also be removed as it will begin to over express to compensate for the loss of G3BP1. We also make use of the related cell lines, ΔΔ17-U2OS-GFP-G3BP2a and ΔΔ17-U2OS-GFP-G3BP2b that have fluorescent G3BP2a and G3BP2b respectively.

We followed the established protocol in the lab: cells are grown within T75 and T25 flasks containing DMEM (Dulbeco's Modified Eagle Medium) [1], with 10% FBS (fetal bovine serum), 1% penicillin-streptomycin, and 1% L-glutamine added by volume. The cells were stored in a 37 °C incubator held at 5% CO_2. The cell population will continue to grow exponentially, and so a fraction of the population must be removed periodically (passaged). This was achieved by first removing the old DMEM, and then twice washing the cultures in 37 °C PBS (phosphate-buffered saline) before being incubated in 0.25 % trypsin[2], in order to detach the cells from the flask, so that they may be transferred. This typically needed to be performed twice a week.

1. Sigma No. D5671
2. Sigma No. T4049

2.1.2 Stressing cells

Cells are prepared for imaging in 35 mm glass dishes[3]. For arsenite treatment, 1 ml of 400 µM sodium arsenite diluted in DMEM is added to 1 ml of untreated DMEM on the cells for a resultant concentration of 200 µM. For the clotrimazole treatment, all DMEM is replaced with 200 mM clotrimazole diluted in the serum free Opti-MeM[4].

2.1.2.1 Fixing cells

In addition to the live cell analysis, we also make occasional use of fixed cells; this process preserves the cell by covalently cross-linking the proteins. Cells were washed twice with 37 °C PBS, before being fixed in 4% paraformaldehyde for 10 minutes and then washed twice again in PBS.

2.1.2.2 Transfecting cells

When an established cell line is not available, the cells lines have to be transfected. This is the insertion of the desired DNA—typically fluorophore tagged—from a bacterial plasmid into the cells. The exogenous genes are introduced into the nucleus, where they are taken into the DNA of the cell, leading to the production of the new protein by the cell.

Transfections are notoriously inconsistent, many cells do not respond at all, and in those cells where the transfection takes, the expression strength may vary by orders of magnitude. In order to improve consistency between cells, we perform FACS (fluorescence-activated cell sorting) upon the transfected cells, this allows us to filter the cells by the expression of a given fluorescent protein. This dramatically improves the number of granules that we can analyse per experiment.

The transected vector will also typically contain resistance to a given antibody, thus allowing us to remove untransfected cells by treating the cells with this antibody. However, the vectors we have are mostly resistant to neomycin which requires 1-2 weeks of treatment and is typically unreliable. This is complicated further as the ΔΔ17-U2OS-GFP-G3BP1 cell line already has resistance to 3 antibodies, due to the two knockouts and the GFP-G3BP1 add back.

The transfection was performed by Tom Stevenson of the Grellscheid group. The cells are chemically transfected with 1 µg of DNA at a ratio of 1:1 per Lipofectamine. Transfection

3. µ-Dish 35mm high Glass bottom, IBIDI Cat. No. 81158
4. Thermofisher Cat No. 31985062

was used to express FXR1-YFP (yellow florescent protein) in the FXR1 over-expression experiments in chapter 4.

2.1.3 Image acquisition

2.1.3.1 Equipment used

For the long time scale observation of granule formation in Chapter 3, we make use of a DeltaVision OMX blaze SR microscope, this is a 3D SIM (structured illumination microscopy) super resolution system located at the Department of Biosciences, Durham University. We used an Olympus TIRF 60x ApoN (NA=1.49) oil lens and took a 3d stack every 2 minutes for 60 minutes.

For the fluctuation analysis in Chapter 4, we used an Andor Dragonfly 505 spinning disk confocal microscope located at the Molecular Imaging Centre, University of Bergen. We take a time series of 1,000 images on each field of view. Finite burst mode was used to collect the frames as rapidly as possible. We aimed to reduce the exposure time of the microscope images in order to minimise the blurring of the rapidly moving stress granule boundary. In order to account for the reduction in signal to noise ratio, high laser power was used, allowing us to achieve an exposure time of 10 ms while still measuring maximum pixel intensity in the 20,000 - 65,536 region in order to make use of the full 16-bit depth resolution of the sensor. When available a 100X 1.49 NA CFI SR HP Apo TIRF oil immersion lens with a 1.5X magnification objective or a 60X 1.40 NA CFI apochromat Lambda oil immersion lens with 2X magnification objective is used on a 1024×1024 pixel iXon 888 Life EMCCD camera.

2.1.3.2 Photo-bleaching and photo-toxicity

In both of these situations, we must consider photo-bleaching, which is the gradual, irreversible degradation of the fluorophores with repeated activation. During the long time scale experiments, we make use of 3D SIM, this requires that a stack of images must be taken–typically 16–each of which contributes to the bleaching. The high laser power used in the fluctuation analysis also causes significant bleaching, and is the limiting factor in how many images we can collect. Due to the nature of the spinning disk microscope, care has to be taken that cells in the surrounding area are not also illuminated and bleached, we, therefore, pick the smallest possible illumination aperture to cover the area of interest. Illumination mode PD2 is also used for this reason.

Repeated laser exposure can also cause the release of reactive oxygen species that can oxidise DNA, proteins or un-saturated lipids, leading to deleterious side-effects in the cell, in a phenomena known as phototoxicity [77]. This is of particular concern during the extended time scale imaging as this toxicity will accumulate with time. Complicating this further, phototoxicity can trigger a stress response and granule formation [unpublished experiments]. Consequently, phototoxicity is the limiting factor in how frequently we can image during the long time scale observations. We performed a control run of imaging with cells in untreated DMEM to ensure that the imaging frequency and light levels used do not cause a stress response, or other deleterious effects in the cells. This is less of a concern in the fluctuation analysis, as we only image the same region of cells once, over a short period of time.

Both of the microscopy methods we have chosen are CCD based, where the entire image is captured at once on a camera-like sensor. This is in comparison to line scan microscopy (LSM), where a laser is rastered across the sample, building the image pixel by pixel. While LSM does offer exciting super-resolution methods, such as Airyscan and STED, we explore why these proved to be unsuitable.

2.1.3.3 Imaging considerations

As explored in the introduction, granules start at a small nucleation site and continue to grow until they are of the order of 1 µm, therefore it is worthwhile to consider what are the optical limits of a microscope. When a point source of light is imaged through a microscope, it will result in a Airy disk, as pictured in fig. 2.1.1.a. This effect is due the limited diameter of the lens aperture, D, and the distance between the maximum intensity point and the first minimum, d is given by,

$$d = 1.22\frac{f\lambda}{D}, \tag{2.1.1}$$

where λ is the wavelength of the light and f is the focal length of the lens[5]. This length defines an "Airy unit" (AU). The Rayleigh criterion [78] states that two objects cannot be distinguished if they are closer than one Airy unit.

It is convenient to characterise the optical properties of a lens by the numerical aperture,

5. The numerical constant is more precisely 1.21966989..., the value of the first minima of the Bessel function of the first kind, order one J_1 divided by π.

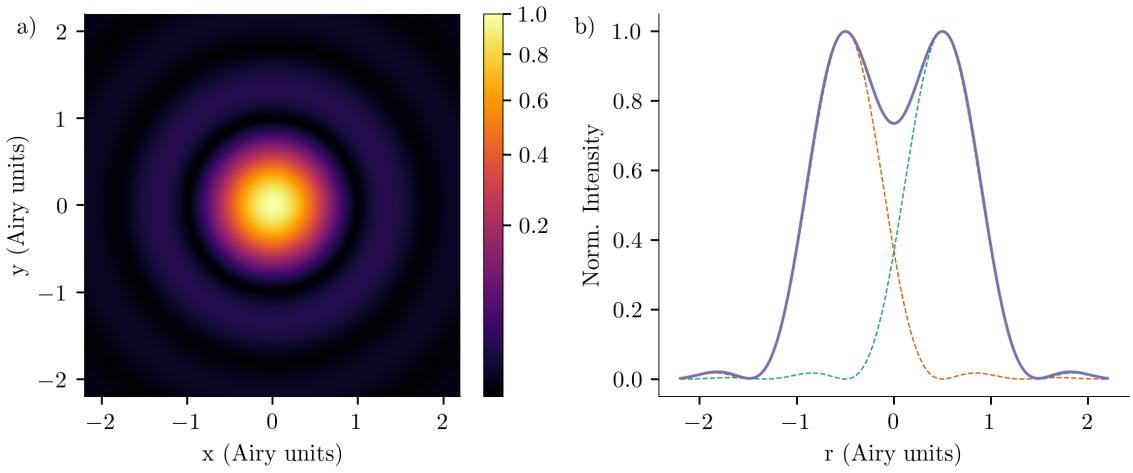

Figure 2.1.1: (a) Simulated image of the observed airy disk when imaging a point source of light. Note the non-linear colour map to highlight the outer rings. An Airy unit is defined to be the distance between the central maximum and the first minimum ring. **(b)** Two point source (dashed lines) separated by 1 AU and the resultant image (solid line). From the Rayleigh criterion this is the limit at which the two sources cannot be resolved.

NA [79]. This allows us to give the diffraction limit as,

$$d = \frac{\lambda}{2\mathrm{NA}} \ . \tag{2.1.2}$$

Currently NA = 1.49 for the highest quality lenses. Assuming a wavelength of 510 nm[6], we get a minimum distance we can resolve as approximately 170 nm. For practical reasons, it is not always possible to choose the smallest value of λ, violet lasers are much less common and violet flourophores are not commonly available.

We are able to overcome the resolution limit by using super resolution methods. Typically these methods are computational super-resolution, and involve taking many images—either in time or the z-dimension—and performing post-processing to calculate the centre of the point spread function. Examples of these methods include deconvoultion, SRRS [80] or hyvolution [81]. However, if we assume that the time taken between images[7] is comparable to the (inverse) frequency of the vibration modes of the surface of the granule, then taking multiple images will only blur the interface and make the reconstruction of the region impossible. This problem is particularly significant during the fluctuation analysis as the rapidly moving interface hinders the restoration step and introduces major artefacts into the resultant image.

Two approaches avoid this problem, STED microscopy and airyscan [82]. In exceptional

6. The peak emission wavelength of the eGFP flourophore most often used in our cells.
7. Notably, this is different from the total exposure time of the image. In CCD cameras, there can be a significant read out time before the camera can take a new image.

cases, STED can achieve an incredible resolution of 8 nm [83] by introducing a second, toroidal laser that acts to deplete the fluorophores around the primary laser, ensuring that the light intensity for given pixel comes only from a very small, well-defined area (see [84] for an overview on the method). However, we find in practice that this method is experimentally challenging in live cells, only offering a slight increase in resolution at the cost of requiring specific fluorophores and introducing a great deal of noise and artefacts in the image.

The Airyscan method works by improving on the pin-hole aperture placed before the sensor in confocal microscopes. This pin-hole blocks out of focus light from the sample, and therefore only light emitted from the focal plane in the sample is recorded, allowing for the confocal microscope to take "slices" through the sample. Reducing the size of this pinhole can improve the resolution limit given in eq. (2.1.2) at the cost of decreasing the signal-to-noise ratio (SNR) of the image by limiting the total light reaching the sensor. Typically a pin-hole of 1 AU is taken; this resolution can be improved by up to a factor of $\approx 1.4\times$ by limiting the pin-hole to 0.2 AU, but doing so blocks 95% of the light from the sample reaching the sensor [82]. Airyscan replaces the pinhole with an array of sensors, each of which are approximately 0.2 AU in diameter and cover a total of 1.2 AU, which allows the sensor array to achieve the higher resolution of a smaller pin-hole while gathering more light than a traditional confocal. Deconvolution from these sensors improves the resolution further. As the images are recorded simultaneously across the sensors, this avoids the moving the interface between frames, and so would be a good candidate for imaging in both experiments. However, we find that the Airyscan is still limited by its LSM nature, as the laser has to be scanned across the FOV, the time to acquire an image increase with the area of the FOV.

For the large-field of view, long-time period imaging required for the granule formation analysis, we found that to get a suitable quality 3D image would typically take 2 minutes, in comparison to a matter of seconds on the DeltaVision 3D SIM microscope. This introduced number of problems: as we aimed to collect an image every two minutes, the 3D SIM could use the extra time to move to another area and collect several time series in parallel. More importantly, however, the near-constant imaging on the airyscan introduced significant photo-bleaching and photo-toxicity that limited the number of images we could take of a given set of cells discussed more .

During the fluctuation analysis the size scaling works in the LSM's favour for small FOVs, for a single granule the airyscan can capture a frame much more rapidly than a spinning

disk, approximately 1 ms instead of 5 ms. However, during the same time, the spinning disk is able to capture granules across multiple cells, which greatly increases the amount of data gathered. While the FOV can be increased on the LSM, the total time to take a frame becomes prohibitively slow as it approaches the FOV of the spinning disk.

2.2 Image Analysis

2.2.1 Locating granules

Once we have the images from the microscope, we must extract the location and shape of the granules. Due to the florescence tag the stress granules are bright blobs on a dark background. This background includes G3BP1-GFP that remains in the cytoplasm, as well as the dark regions between cells. An example image is shown in fig. 2.2.1.a.

2.2.1.1 Threshold based detection

Perhaps the most intuitive method of locating granules is a by introducing a threshold, where the pixels are divided into either foreground (granules) or background. Any pixel brighter than or equal to a threshold intensity, T, is classed as foreground, otherwise they belong to the background.

While the threshold value may be chosen arbitrarily, it is typically chosen to maximise some criteria. In our first implementation we used the commonly chosen Otsu's method, which minimises the variation between the two regions,

$$\sigma_\omega^2(t) = \omega_0(t)\sigma_0^2(t) + \omega_1(t)\sigma_1^2(t) \ , \tag{2.2.1}$$

where 0 and 1 are the background and foreground regions respectively. The variance in the regions, σ_i is calculated as $\mu_1(t) - \mu_T$ where μ_T is the mean intensity of the image. These values are then weighted by the factors, ω_i, as given by Otsu et al. [85].

Thresholding methods are computationally inexpensive and perform well in simple situations, however, they work best when the intensity histogram is bimodal. This is typically the case in the later stage of granule formation when most of the cytoplasmic G3BP1 is in granules, causing the granules to be far brighter than the surround cytoplasm. However, when the cells are starting to form the granules, a majority of the G3BP1-GFP is still in the cytoplasm, and therefore there is much less contrast with the granules. This lack of contrast

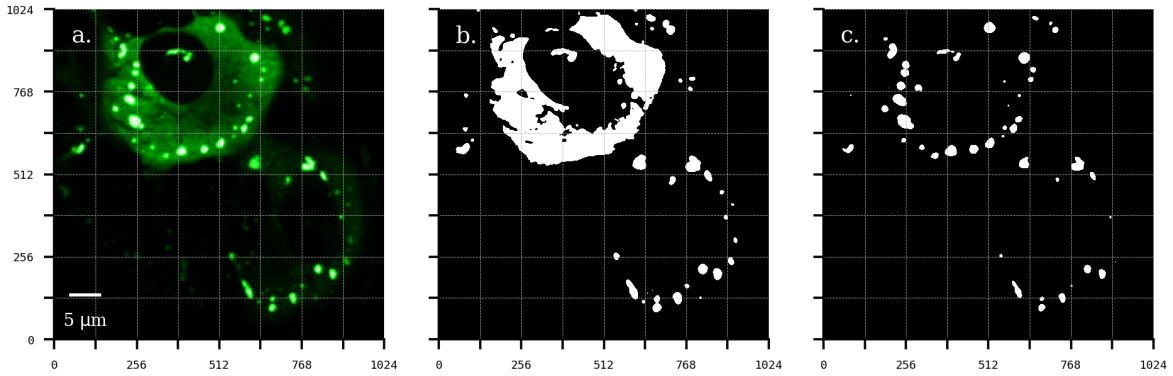

Figure 2.2.1: Comparison of thresholding methods. **(a)** Image as taken from the microscope. This is a particularly challenging image to threshold due to the much brighter cell at the top of the image **(b)** Granules selected by the Otsu method. We see that the threshold returns the rough shape of the granules, but notice that a large region of the brighter cell has been misidentified as single granule. While this will be removed in further analysis, it means we are unable to analyse any of the granules within this region. **(c)** Yen's method is better able to identify the granules in this case, but there are still a number of granules in the dimmer cell that are not recognised.

is also compounded by photo-bleaching.

If the threshold value chosen is too low, then parts of the background will be mis-identified as granules, as shown in fig 2.2.1.b. While we are able to remove the large erroneous area from further analysis, we are unable to get any information about the granules in this area. There are several other algorithms for choosing the threshold intensity, and while a manual comparison of these methods reveal that some approaches, such as Yen's method [86], do give an improvement over the Otsu method, the threshold level in this case is too high to isolate some of the granules in the dimmer cell, as we can see in fig. 2.2.1.c. This is preferable to the previous method, but still not ideal.

In images of multiple cells it may happen that the cytoplasm in one cell is brighter than some granules in another cell. This means that it is impossible to choose a global threshold value, T, that will isolate all of the granules without false-positives elsewhere. This is particularly relevant in the case of transfected cells, where the brightness may vary by orders of magnitudes. Adaptive threshold methods [87] attempt to overcome this problem by instead using a local threshold, where a threshold is calculated for each pixel based on the surrounding area. A simple implementation of this may be based on the mean of the surrounding pixels, for instance, if a pixel is brighter than the mean of the pixels in the surrounding area then it is classed as foreground. This method tends to return a large number of false positives in the cytoplasm, and while this effect can be reduced by increasing the size of the local region considered, this becomes increasingly computationally expensive and starts to exhibit the same problems as

the global threshold, where brighter cytoplasm regions will obscure granules in the area. This leaves the method brittle: a set of parameters that work well in one group of images may not work well in another group.

2.2.1.2 Laplacian of Gaussian

A more robust method is the Laplacian of Gaussian (LoG) method. This is a more computationally expensive approach that is better able to detect blobs against a complex background. The Laplacian operator, $\nabla^2 \equiv \Delta$ calculates the sum of the second derivatives at each point in the image, namely,

$$\nabla^2 = \frac{\partial^2}{\partial x^2} + \frac{\partial^2}{\partial y^2}. \tag{2.2.2}$$

This operator is strongly negative around maxima (blobs). It is however very sensitive to noise and so the image, $I(x, y)$, is first convolved with a Gaussian kernel of width σ,

$$g(x, y, \sigma) = \frac{1}{\sqrt{2\pi\sigma^2}} \exp\left(-\frac{x^2 + y^2}{2\sigma^2}\right) \tag{2.2.3a}$$

$$\equiv \frac{1}{2\pi t} \exp\left(-\frac{x^2 + y^2}{2t}\right) . \tag{2.2.3b}$$

This smooths the image and greatly reduces noise. $t = \sigma^2$ is common substitution in the literature that is mathematically more convenient.

The resultant image is part of a 3-dimensional *scale space representation*, $L(x, y, t) = g(x, y, t) * I(x, y)$.[1] The operator $\nabla^2 L$ is strongly negative for blobs of radius $r \approx \sqrt{2}t$. To locate granules of different sizes we repeat this convolution for a range of values of t. As smaller blobs give a stronger response[2], a normalisation factor is applied,

$$\nabla^2_n L(x, y, t) \equiv t\nabla^2 L(x, y, t) \ , \tag{2.2.4}$$

to define a scale-invariant response, $\nabla^2_n L(x, y, t)$.

A blob is then defined as any point (x_b, y_b, t_b) for which $\nabla^2_n L(x_b, y_b, t_b)$ is greater than all of its 27 neighbours. We therefore, not only get the location of the granule (x_b, y_b) but also an estimate of the granule size (t_b). As the microscope metadata includes the size of each

1. While in theory all three variables are continuous, in practice x and y are the discreet pixels in the image and σ will be evaluated at set number of discreet values.

2. For two areas of the same intensity, the magnitude of the second derivative will be greater for the smaller region.

pixel in relation to the physical sample, we are able to link the size of t to the physical size of the granules. However, the Laplacian operator is computationally expensive and significantly slows the LoG method.

Difference of Gaussian

To remove the dependence on the Laplacian operator, in the Difference of Gaussian (DoG) method we make use of the relation [88], [3]

$$\frac{1}{2}\nabla^2 L = \frac{\partial L}{\partial t} \ . \tag{2.2.5}$$

Using this with the definition of the derivative and eq. (2.2.4), we may give the normalised Laplacian as

$$\nabla_n^2 L = \lim_{\delta t \to 0} \frac{t}{\delta t}[L(x, y, t + \delta t) - L(x, y, t)] \tag{2.2.6}$$

$$\nabla_n^2 L \approx \frac{t}{\Delta t}[L(x, y, t + \Delta t) - L(x, y, t)] \ . \tag{2.2.7}$$

The DoG therefore approximates the $\nabla_n^2 L$ as the difference of two Gaussian smoothed images. This approximation makes DoG much faster but does not hold as well for smaller blobs. For this reason, the LoG method is used in Chapter 3, where it is important to detect the smaller granules. However, in Chapter 4, these smaller granules are unsuitable for fluctuation analysis and 1,000 frames are analysed per series, so the DoG approximation is used.

2.2.2 Estimation of granule shape

As can be seen in fig. 2.2.1, threshold based methods return a set of pixels that define each granule. These can be used to estimate properties of the granule, such as the area, perimeter or roundness. These can either be used directly or may be used to filters the granules that will go on for further analysis. However, the LoG and DoG methods return only the location of the granule along with a rough estimate of the size, fig. 2.2.2.b. We therefore require a flood fill step to classify the pixels that belong to each granule. In a flood fill we search the area surrounding the centre of the granule for the point with the highest intensity and label this pixel part of the granule. Using the intensity of this pixel, $I_{\max}$, we define a threshold

3. This equation is known as the diffusion equation. This form is a major motivation for the $t = \sigma^2$ substitution.

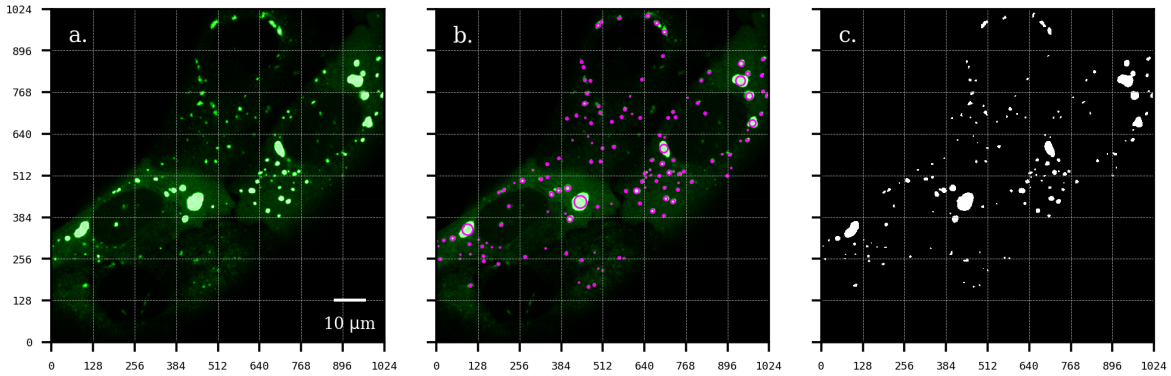

Figure 2.2.2: Example of the DoG method. **(a)** Example image from the microscope. **(b)** The detections from the DoG are overlaid in the image with a magenta ring, the radius of which corresponds to the estimated radius. **(c)** A flood-fill step is used to calculate the extent of the granules. It can be seen that this method returns even small and dim granules without any false positves.

intensity, I_T, given as, say, $I_T = 0.5I_{\max}$. Any pixel neighbouring the granule that is above this threshold is labelled as part of the granule. This step repeats until no more pixels can be added, giving us the full extent of the granule.

This process is then repeated for all blobs. While this method is rudimentary, it performs well for the granule growth analysis in Chapter 3 and as a rough estimation of the granule shape in Chapter 4 for preliminary filtering as can be seen in fig. 2.2.2.c. A more accurate method is required to locate the boundary in the fluctuation analysis, as described in sec. 4.3.

Besides the increased accuracy, an advantage of these methods over the threshold based approach is that all of the extent of all the granules is calculated independently, if one granule is detected poorly it can be removed from further analysis without affecting the other granules in the area.

Chapter 3

Modelling Granule Growth

3.1 A Model to Describe Granule Growth and Formation

In the introductory chapter, we laid out the theoretical background for phase separation in a simple system. In this section, we aim to create a physical model in order to bridge the gap between the theoretical model and experiment, and using this, we want to study the formation and growth of stress granules at the level of an entire cell. The simulations are then used to measure physical parameters from the experimental data and investigate where this diverges from the simple theoretical model.

3.1.1 Potential Models

Stress granule formation is both "redundant and adaptable", many proteins critical to granule formation in one situation can be absent when granules are formed under other conditions [54, 28, 45]. Indeed, by over-expression of proteins like G3BP, Caprin1 or FAST [38, 89, 90, 91] stress granules can form spontaneously, bypassing the requirement for polysome disassembly, which leads to granules formation independent of mRNA levels.

Over 900 proteins are found to co-localise within granules [59, 38, 60], with the exact function of many remaining unclear. It is unclear which of these are merely sequestered into the granule, or which have a functional role in phase separation. Compounding this problem, stress granule composition changes depending on the activating stress [92, 14].

This uncertainty in the composition of the stress granules limits the amount of detail that we can include in our model. The most detailed way of simulating interactions between proteins is a molecular dynamics simulation which considers the interactions between all atoms in the system. Besides the infeasible computational expense, typically requiring days to simulate nano-seconds of model time, we lack the information on the structure and distribution of proteins within stress granules—or the rest of the cell—in order to initialise such a model.

At the opposite end of the spectrum, phase fields models exist that could be used to imple-

ment the phase separation theory covered in chapter I directly [93, 94, 95]. These models break space down into voxels, and calculates the concentration ϕ_i of component i in each of these voxels. These models can gain much insight into the phase separation mechanics of two [27] or more [96] phases. However, the number of voxels required to model the cell in appropriate detail to capture the dynamics of small granules soon becomes prohibitively computationally expensive. Further, while many of the behaviours such as diffusion and coalescence can be described naturally by these models, it can challenging to describe some biologically active processes in this framework [25].

Another approach to model stress granules is to abstract away much of the complexity of the proteins involved, but keep the notion of "particles" at some coarse grained level. One popular level of complexity treats the proteins as flexible strings connecting binding sites "beads", from which it is possible to investigate, for instance, the balance of stronger specific interactions or weaker non-specific regions or which factors limit coarsening [97, 98, 35, 99]. While powerful, these methods are typically limited to considering only a single granule.

In order to examine the behaviour of stress granules at the level of an entire cell, we have to abstract the complexity away further and consider a more coarse-grained model. We, therefore, introduce a reaction-diffusion model to investigate the interactions between mRNP particles as they diffuse and grow to form stress granules.

There are three main actions that the particles undergo in the simulation. The first step is diffusion, where the droplets move randomly around in the cytoplasm. Second, this movement may cause collisions between two droplets, leading to coalescence and the formation of a single larger droplet. Finally, granules are also dynamic, material moves from the droplet and back into the cytoplasm, in a process which we refer to as attrition. In the next section, we discuss the implementation of each of these actions in more detail, including how they are parameterised and linked to physically observable values.

3.1.1.1 Goal of the model

The three actions above allow us to capture the behaviour of the physical system. There are three primary areas we wish to investigate with these reaction-diffusion steps:

1. The cytoplasm of the cell is very viscous and is interlaced with an actin filament network that we might expect to hinder granule diffusion, especially as the granules grow. Is diffusion enough to explain granule growth, or is there some active process that drives

transport?

2. As introduced in the introduction, Ostwald ripening is a phenomenon in LLPS systems whereby larger droplets will continue to grow at the expense of smaller droplets once material is depleted from the background. We wish to investigate what role Ostwald ripening and granule coalescence has on the size distribution in the coarsening stage of formation, once the mRNP in the background is no longer supersaturated.

3. We know that material is continuously exchanged between the granules and the cytoplasm, but what is the nature of the material lost from the granule.

We now propose an outline of the expected behaviour in the model. At the start of the simulation, many individual particles diffuse around in the model cell, and these particles frequently merge but then rapidly fall apart. These droplets can only grow further if they undergo several collisions in rapid succession. This makes the formation of clusters of multiple particles unlikely and mirrors the random nature of noise-based nucleation. Once these clusters reach a given size, $n_{\text{proto}} = 4$, they become more stable than the small clusters, at which point we refer to them as proto-granules. Proto-granules still undergo attrition as we see from FRAP results that RNP is still returned to the cytoplasm, but at a much slower rater.

We propose that these larger proto-granules are more stable due to the establishment of a scaffold-like structure from less mobile proteins such as FXR1. This effect has been observed in a number of LLPS systems [70]. As the granules continue to grow, we can change the diffusion behaviour of the particles, this may include confining the granules to a radial walk to simulate a movement on a microtubial.

3.1.2 Implementation

The most crucial step in implementing this simulation is the coalescence of two droplets. This typically involves two stages: calculating the distance between two particles to test if they are within a reaction radius and if so, checking if they interact. The first of these stages is the most computationally expensive operation in the simulation, as a naive implementation will check all pairs of particles[1]. The second step is highly non-trivial, as we have to link the reaction probability to the macroscopic rate constant and likelihood that the particles happen come into contact.

1. In the optimisation section, we cover steps that can be taken to reduce this expense.

3.1.2.1 Diffusion

From Fick's second law, we have that during a time δt, a particle with diffusion constant D will diffuse a distance δx given by $\langle \delta x \rangle^2 = 6 D_n \delta t$. To simplify the implementation of the coalescence events, we implement diffusion at each time step by allowing a particle to jump a distance, l, in a random distance with a probability,

$$P_{rw}(n) = 1 - e^{-\Delta t / \tau_n} \ , \tag{3.1.1}$$

where Δt is the simulation time-step. τ_n is the waiting time and is chosen to retain the correct rate of diffusion within the model

$$\tau_n \equiv \frac{l^2}{6 D_n}. \tag{3.1.2}$$

The jump length is required to be longer than the expected diffusion distance during a simulation timestep ($l > 6 D \Delta t$). This means that the granule does not move continuously with each timestep, but instead takes a longer jump of length l with a period corresponding to the waiting time τ. As the waiting time is still many orders of magnitude smaller than the total simulation time, T, the overall diffusion behaviour matches that of the smaller timestep case, making the coalescence step easier to implement.

The subscript n indicates that the diffusion constant, D_n, and correspondingly the waiting time τ_n, depends on the size of the RNP droplet. Generally diffusion is slower (smaller D) for larger droplets. Following the work of Oshima et al. [57], rather than assigning a different diffusion constant for each possible size of RNP droplet, we instead have separate diffusion constants for RNA droplets smaller and larger than the proto-granule limit.

Biased walks

In addition, for droplets larger than some size, n_{bias}, we will consider possible effects due to biased radial diffusion towards the centre of the cell. Once a proto-granule has exceeded n_{bias}, we consider it a full sized granule. The motivation to introduce this biased radial diffusion is two-fold. Firstly, it will become increasingly difficult for larger particles to diffuse in the crowded cytoplasm. Second, it has been debated whether active transport (e.g. as accommodated by microtubules) plays a role in the formation and growth of RNP droplets. The model parameters

used in this chapter are summarised in table 3.4.1.

3.1.2.2 Coalescence

The second component of our model is the coalescence of two RNP droplets into a single larger droplet. If we denote c_n as the concentration of RNP droplets of size n, we can write down the macroscopic chemical reaction for the coalescence of droplets of sizes m and n into those of $m+n$ as

$$\mathrm{c}_m + \mathrm{c}_n \xrightarrow{k_{m,n}} \mathrm{c}_{m+n}, \tag{3.1.3}$$

where $k_{m,n}$ is the macroscopic rate constant.

If a particle takes a diffusion step, we check if this step brings the moved particle—of size m—to within a collision radius, $r_{m,n}$, a particle of size n. If it is within the collision radius, then there is a probability that the two particles will collide and merge, given by

$$P_{\mathrm{c}}(m,n) = \frac{1}{\frac{4}{3}\pi r_{m,n}^3 N_A} \frac{k_{m,n}\,\Delta t}{2 - e^{-\Delta t/\tau_m} - e^{-\Delta t/\tau_n}}, \tag{3.1.4}$$

where N_A is the Avogadro constant, τ_m and τ_n are the waiting times of particles of sizes m and n, as defined in eq. (3.1.2). The detailed derivation of eq. (3.1.4) can be found in [100]. This reaction probability relates the rate at which the particles collide via diffusion to the expected macroscopic reaction rate $k_{m,n}$.

This approach is not fully constrained, and so we can choose a collision radius $r_{m,n}$ and use this to calculate the reaction probability $P_{\mathrm{c}}(m,n)$ [101]. In principle, the method is more accurate the smaller the reaction volume, as this follows the assumptions made in the derivation better. However, if the reaction volume is too small, the approach breaks down as this would require $P_{\mathrm{c}}(m,n) > 1$ to match the macroscopic reaction rate.

Following the works of Ohshima et al [57], we set $n_{\mathrm{proto}} = 4$ and use unique rate constants $k_{m,n}$ for possible values of $m, n = 1, 2, 3, 4$. For droplets larger than the size of the proto-granules, $n > 4$, we assume they have the same rates as those for $n_{\mathrm{proto}} = 4$ when interacting with clusters smaller than proto-granules. Finally, in the case of two larger granules merging, we set $P_c = 1$ and increase the reaction radius according to $r_{m,n} = r_{\mathrm{large}}(m^{1/3} + n^{1/3})$, to account for the increasing radius of the particles involved, while also avoiding breakdown of the model. By varying the value of r_{large} we are able to increase the merging rate of the larger

granules.

Optimisation

We can divide the coalescence step into three main sections, movement of the particles, checking for reactions and updating the cluster size. Upon benchmarking, it soon becomes clear that checking for the reactions is the time-critical step. This is because, in a naive implementation, all particles must be tested against all others, making this an $\mathcal{O}(n^2)$ step[2]. In order to avoid this, it is common to break the simulation space into a grid [102, 103, 101] of blocks and only calculating the distance between particles in the same or neighbouring cells, reducing this to $\mathcal{O}(n)$.

While this offers a significant improvement in the simulation performance, reading particle positions from memory becomes the limiting factor. To explain why, we introduce a simplified model of a computer, which consists of a processor that performs calculations, a small cache of fast memory connected to the processor and a relatively slow, but much larger memory (RAM)[3].

A typical processor works at approximately 3 billion cycles per second or around 0.3 ns per cycle. Therefore, calculating the distance between a pair of particles will typically take the order of nanoseconds. However, the particle positions are stored within the RAM, and the processor must copy a 'line' of data from the RAM to the cache before it can work on the data. The lines are a fixed size of contiguous memory, meaning that the positions of many particles are copied in each operation, however, this copy is very slow (relatively), taking the order of 100 ns.

This delay becomes problematic when we consider only the interactions between particles in the neighbouring cells, as there is no correspondence between the position of the particles in the simulated space and in the RAM. In the worst case, when calculating the distance from a given particle, each comparison particle would be on a different 'line' and so would require a cache read each time. This would mean that the processor spends much of its time idle as it waits for data.

To avoid this fragmentation problem, we require that the particles that are close to each other in the simulation space are also close together in memory. Therefore, we add a sorting

2. Big O notation gives the computational complexity of the function. For an $\mathcal{O}(n)$ function, the work scales linearly with the number of particles. For the $\mathcal{O}(n^2)$ the work scales with the square of the number of particles.

3. This is *vast* over simplification of modern processors with multiple levels of cache, but it is enough for this analogy.

step before the distance check: the simulation space is divided up into M equally spaced blocks in each direction and the particles labelled by which cell they are in. This label is then used as the sort key [104, 105, 106]. For instance, if we use a scheme where the label is given by (X, Y, Z) where X is the number of the block in the x dimension, the particles in $(0, 0, 0)$ are moved to the first group, $(1, 0, 0)$ the second and so on; once we have reached the limit in the x direction, then we start at $(0, 1, 0)$, as is shown in 3.1.1.a. Although this sorting step introduces its own computational cost[4], we find that the overall performance gains are significant, as now all the particles within a block can be brought into the cache at once and the processor can work continuously [104].

One final subtlety is the choice of the labelling system for the cells. The labelling system given above; (X, Y, Z), while simple, has a flaw, cells in the x direction will end up close together in memory, but those in the y and z are located much further away as can be seen in fig. 3.1.1.a. While the particles in a single block are grouped close together, there may still be a siginificant distance between those in neighbouring cells. Therefore, we instead use a z-ordering or morton code [107, 108] to label the cells, with an example shown in fig. 3.1.1. The (X, Y, Z) coordinates are converted to a one-dimensional Morton index by interleaving the bits in the X, Y and Z values. Other schemes, such a Hamiltonian curve, are arguably more effective at reducing the distance between the nearby blocks in memory, however they are more difficult to implement and are more computationally expensive [109]. Whereas the grid index can be converted to Morton index using simple bit operations, that are both easy to implement and can be computed rapidly.

Overall this leads to a significant improvement in run time, while the authors in [57] required 24 hours of run time for a similar simulation (on a 3.4 GHz i7-4770), we found an average completion time of 20 minutes (on a slower 2.4 GHz Xeon E5-2680). While a small variation is to be expected due to the hardware, we have over an order of magnitude decrease in the simulation run time. Due to the stochastic nature of the simulations, this improvement in performance is significant as we can run more simulations in a given time and average the random noise between runs and allows us to refine the parameters in the model more efficiently.

4. The choice of the sorting algorithm has a significant impact on the overall performance. The quicksort algorithm is typically regarded one of the "best" choices for many applications, but it performs poorly in this case, where the data is (after the first step) already mostly sorted and containing many of the same values.

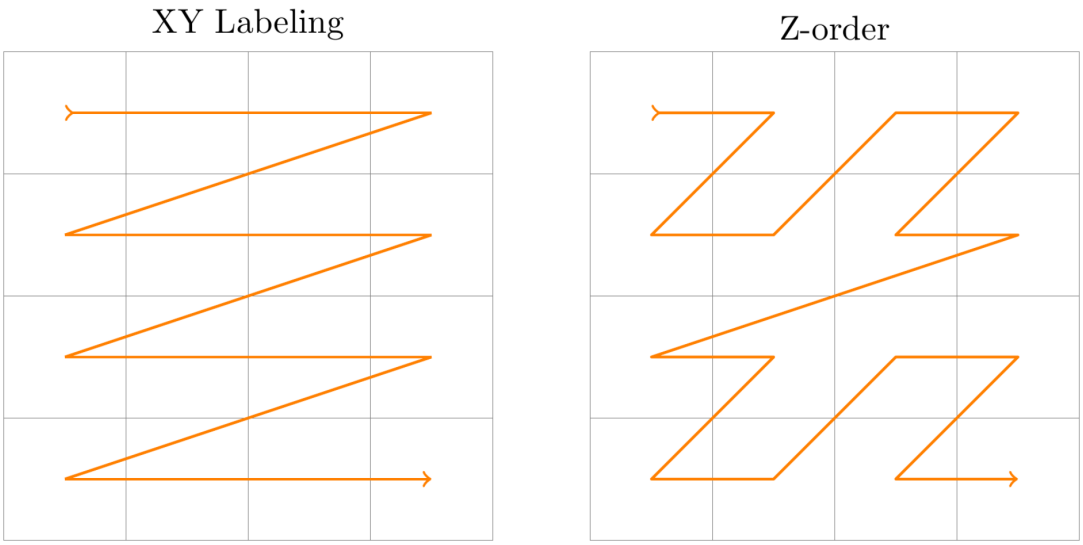

Figure 3.1.1: Example labelling scheme for the blocks in two dimensions. **(a)** In the first case the cells are labelled along the x-direction first, before incrementing in the y-direction. This means that there is a large gap in memory between the cells along the y-direction. **(b)** The average distance in-memory between the cells is decreased using the z-curve/morton code.

3.1.2.3 Attrition

Loss of material from the granule is a first order reaction characterized by a decay constant, d_n, which is the probability of decay per unit time and has units of s^{-1}. In our approach the loss of material can be represented as the splitting of a droplet into smaller parts,

$$\mathrm{c}_n \xrightarrow{d_n} \mathrm{c}_{n-m} + \mathrm{c}_m \ . \tag{3.1.5}$$

To match the decay constant, the probability of decay for a particle in a given simulation time-step is given by

$$P_\mathrm{d}(n) = 1 - \exp(-d_n \Delta t) \ , \tag{3.1.6}$$

where we have to ensure that $d_n \ll 1/\Delta t$.

During the attrition of small granules we randomly choose the value of m in eq. (3.1.5) from 1 to $n-1$, however in larger granules, we place an upper limit on the value of m, to limit the size of the material lost from the granule. As we will discuss in the results section, we consider several possibilities for this upper limit, m_max as these lead to significant changes in the behaviour of the attrition modes. In our implementation, we have used individual decay rates for small RNP droplets ($n \leq n_\mathrm{proto} - 1 = 3$) and a single attrition rate for the larger

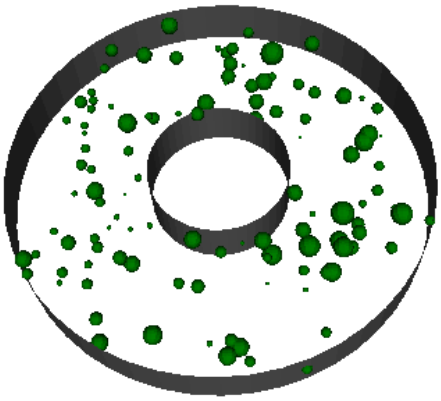

Figure 3.1.2: Our model cell with G3BP droplets pictured in the cytolpasm. The inner ring of the cell corresponds to the nucleus and granules are excluded from this region.

droplets ($n \geq n_{\text{proto}} = 4$), independent of size.

In general, this treatment of attrition leaves the model time irreversible. As two droplets of sizes greater than $m_{\max}$ can coalesce, but then cannot split into two droplets of the original sizes. This can be mitigated by either a choice of $m_{\max}$ that depends on the size of the granule or making $m_{\max}$ sufficiently large.

3.1.2.4 Model cell

We simulate the cell as a three dimensional ring or *annular cylinder*, with an outer radius of 6 µm and inner radius of 2 µm and a height of 1.5 µm as pictured in fig. 3.1.2. Particles are excluded from the inner region that corresponds to the model nucleus. The particles start distributed evenly throughout the cell as described in sec. 3.4.1.1.

3.2 Results

3.2.1 Exploring the parameter space

The presented model has a relatively large number of parameters for droplet coalescence, decay and attrition. For our case of $n_{\text{proto}} = 4$, we have 10 coalescence rates for $k_{m,n}$, with $m, n = 1, 2, 3, 4$ and 4 decay and attrition rates for d_n, with $n = 1, 2, 3, 4$. This gives a total of fourteen parameters, in addition to two diffusion coefficients for large and small RNP droplets. Therefore we will take steps to reduce the parameter space. This is to ensure, that we do not over-fit the experimental data and to make exploring the parameter space less computationally expensive.

In this subsection, we investigate which coalescence parameters in the model are the most important, and which ones may be removed from further analysis. To do this, we first run a set of control simulations, and then a series of repeats where each perturbed a single parameter. For each set of simulations, we run and average the results from 10 independent simulations. Fig. 3.2.1.a shows the results for granule count as a function of time, where clusters of more than twelve particles are counted as granules visible by microscopy.

We observe that perturbing the majority of the coalescence rate constants makes little change to the time distribution of the granule count. The most significant changes come from perturbing the coalescence rates between the particle monomers with other RNP droplets. To understand why this is the case, in fig. 3.2.1.c we show heat maps of the count of coalescence events in the simulation. This leads us to propose the following explanation: first, the formation of granules is determined by $k_{1,1}$, $k_{1,2}$ and $k_{1,3}$, as we see that the reaction between monomers is the most common. The dimers often decay back into monomers, but they can undergo a quick succession of collisions with other monomers to form trimers and proto-granules. Second, the growth of granules is mostly due to collisions with monomers (diffusion-limited growth). Indeed, increasing $k_{1,4}$ leads to material more rapidly accumulating on the proto-granules (larger average size), but at the same time, it depletes the surrounding background

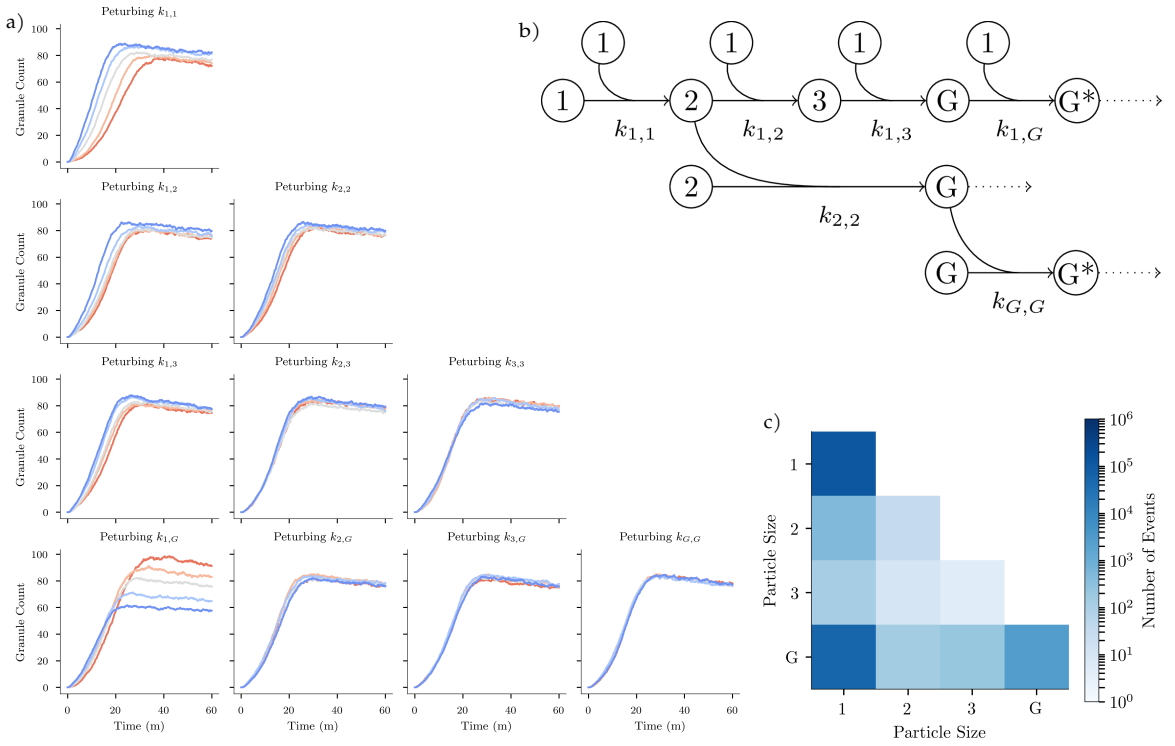

Figure 3.2.1: **(a)** By perturbing a reaction rate, k, we can examine its relative importance; the original values, given in grey are those in table 3.4.1, blue values are scaled by a factor of 1.5 and 2 and red scaled by a factor of 0.7 and 0.5. The most significant changes are shown in the reactions involving monomers. **(c)** We can see that this is due to the frequncy of the reactions of each particle type, as shown in the heatmap. The reactions between pairs of monomers and a monomer and large granule are the most dominant. Therefore we consider the simplified reaction as shown in **(b)**, the other parameters are removed from futher analysis. The particles with more than 4 components (G*) are treated in the same manner as those of size 4.

and prevents the formation of nearby granules.

Another mechanism for granules to grow is via droplet-droplet coalescence. While this does occur, in our simulations, we find it is orders of magnitude less common than the monomer-droplet interactions, but we will investigate the role this plays in later sections. In some scenarios, we find that the dimer-dimer collision rates can become relevant. However, our simulation results are insensitive to the values of the other coalescence rates, as they rarely occur. This leads us to a simplified model shown in fig. 3.2.1.b, where the dominant coalescence rates are highlighted.

Now that we have an understanding of the parameters in the model, we may use these to attempt to change the time and size distribution of the granules and compare this to our experimental results. We gather the imaging data using the OMX-blaze 3D-SIM microscope, creating a 3d image of the cells every 5 minutes. We then use a maximum projection to flatten this stack into a 2d image. An example image is shown in fig. 3.2.2 for treated and untreated

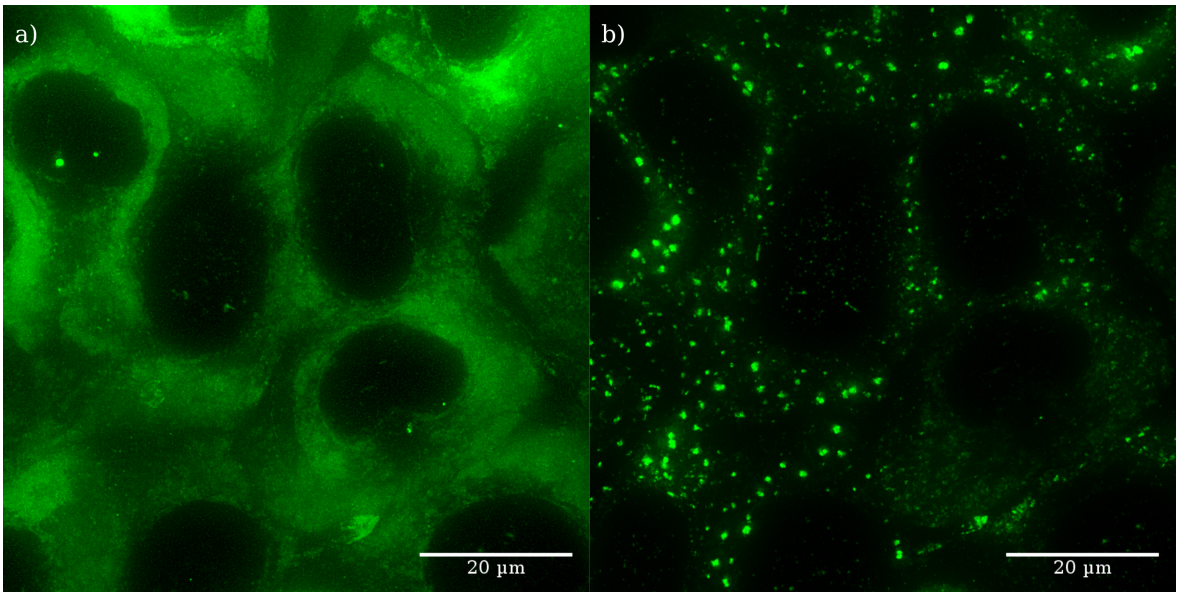

Figure 3.2.2: Examples microscope image of the cells **(a)** before and **(b)** after treatment taken from the OMX microscope used in the analysis.

cells. A Difference of Gaussian method is used to locate the granules and a flood fill algorithm is then used to draw an approximate boundary[1] as demonstrated in fig. 3.2.3. Boundaries between the cells are drawn by hand, and granules are grouped by the cell.

To obtain the best fit simulation parameters that match the experimental observation we performed a manual guided optimisation: we generate several possible parameter perturbations and simulate these in parallel, and then judge the best fitting parameters. We iterate this process until we have a good agreement with the experimental data if possible. Parameters that have no clear effect on the model were ignored. While automatic minimisation algorithms such as L-BFGS-B [110] are powerful, they require the calculation of a gradient vector (Jacobian) at each step, which involves repeatedly running the simulation while changing each of parameters in turn. As many hundreds of total steps are typically required for convergence, the long run times of the simulation (and the averaging repeats) would have lead to very slow convergence. As the simulations are stochastic, we perform multiple repeats of each run, so that we may average and reduce the noise in the size and time distribution of the granules.

Changing the rate constants and decay rates in this manner allows for some slight control over the count and size distribution of the granules. However, in order to investigate physical dynamics of the model, we require more significant changes to the model. The behaviours of the small clusters and proto-granules are below the microscopy limit and so are not observable directly, but has large impacts on the resultant distribution of the granules. By investigating

1. sec. 2.2.1.2 and 2.2.2

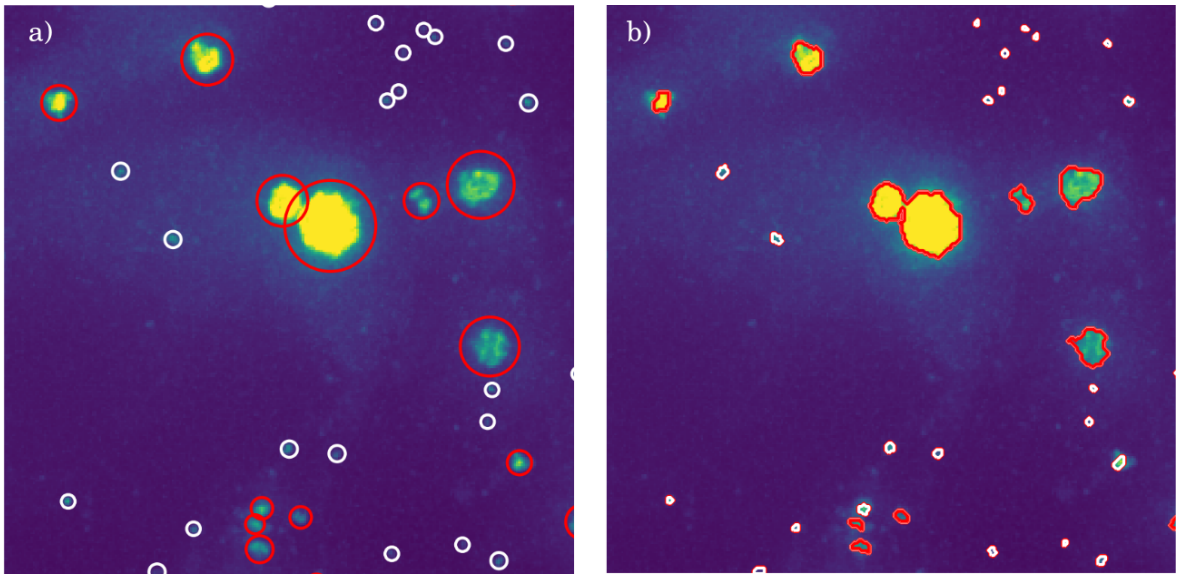

Figure 3.2.3: **(a)** Cropped image of granules located by the DoG algorithm. Smaller, uncertain detections are labelled in white. **(b)** Extent of the granule as measured using the flood-fill method gives us a rough boundary and measure of the granule area.

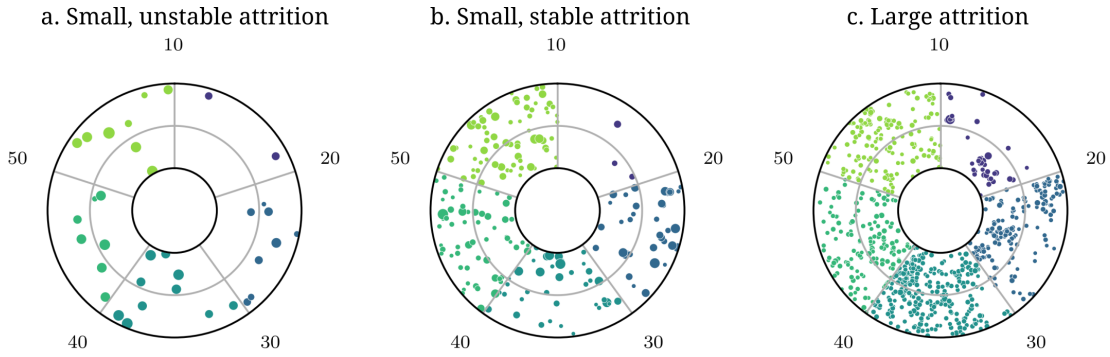

Figure 3.2.4: Top down view of our model cell. Each disk corresponds to a different exeperiment and the time advances in each segment in 10 minute intervals in a clockwise manner. In the case of the small, unstable decay ($n < 3$), we are left with a few larger granules. In the case of $n > m/2$ we have a large number of small granules. In the case of small, stable attrition we have a mixturue of granule sizes. This is explored more quantitatively in next figure.

these behaviours in the model to biological mechanisms of the cell, we can gain insight into stress granule formation in-vivo.

3.2.2 Attrition modes

While it is clear from FRAP experiments that there is material transport between the granule and the surrounding cytoplasm, it is unclear what form this material takes and if it has any influence on the surrounding granules. To investigate this, we extend the current attrition implementation of the model: by limiting the maximum possible size of the droplet lost during attrition events, we can change how the granule interacts with the surrounding area.

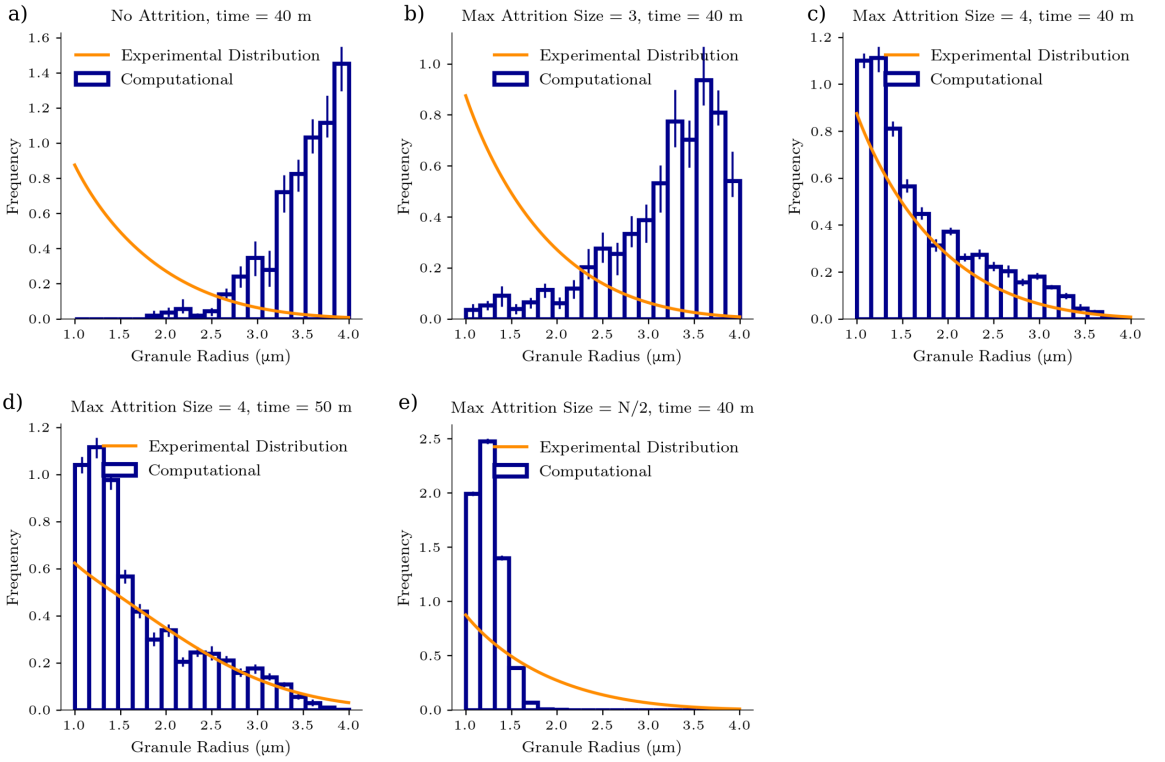

Figure 3.2.5: Match of model size distributions (blue bars with std. dev. error bars) compared to emperical data at a given time point. **(a)** When no attrition occurs the there is a strong skew to larger granules, similarly for the case of the small attrition mode **(b)**. **(c)** When we allow the granules to undergo split attriton there is strong skew towards smaller granules. **(d)-(e)** The only mode that gives a good fit to the size distribution is case when decay products may be small proto-granules, this shown at both 40 and 50 minute time points.

For a granule of size m we limit the size of the secondary particle lost to n. We find that there are four main regimes dependant on the value of n,

1. Small, unstable attrition, $n < n_{\text{proto}}$: in this case, the secondary droplets lost from the parent granule are smaller than the proto-granule limit, meaning that they are still unstable

2. Small, stable attrition, $n = n_{\text{proto}}$: the secondary droplets are possibly stable proto-granules

3. Large attrition, $n = m/2$: when the granule undergoes attrition, it may split into two equally sized granules

A comparison of how these modes progress with time is given in fig. 3.2.4, where for each experiment we show a snapshot of the granules during the simulation giving a qualitative overview of the granule size distribution and count. A quantitative size distribution, and comparison to the experimental distribution for each experiment is given in fig. 3.2.5.

In the first case, the secondary droplets lost during attrition are small and unstable and rapidly decay into background monomers. This what is typically implicitly assumed in most LLPS models, that the material is unchanged if it enters and leaves the phase-separated region. As the granule grows, it depletes material from the surrounding area and hence decreases formation rates in the local area, meaning that the there is limited inter-granule interactions. This means the granules are distributed sparsely across the cell and reach equilibrium with their surroundings, leading to large granules of roughly the same size, fig. 3.2.4.b. This is similar to the case of no attrition, but with a smaller average size, as in this case the growth soon becomes diffusion-limited instead, as seen in fig. 3.2.5.a, with the skew in the size distribution favouring larger granules.

In the second case, there is some probability that the droplets lost due to attrition are small proto-granules that act as nucleation sites that continue to grow by absorption of material from the cytoplasm. In contrast to the previous case, this means that the presence of a granule will increase the formation rate of granules in the local area, leading to a wider size distribution. However, the competition for RNP material will lead to a smaller overall average size, as shown in two time points at in fig. 3.2.5.c-d with a strong agreement with the empirical size distribution due to a mixture of granule sizes.

In the third case, rather than the granule losing a small fraction of material during attrition, it is possible for the granule to split into two granules of equal size, hence allowing for the model to be time reversible. his much more aggressive attrition further decreases the mean size of the granules. Compounding this, as secondary granules are immediately able to undergo the same attrition, this can lead to a cascade of new granules being formed in the local area. This effect is motivated by [111] whereby droplets in similar active phase separation systems may become unstable and split into two smaller droplets. The results of this splitting with max attrition size = $N/2$ are shown in fig. 3.2.5, resulting in a large number of smaller granules. Further in fig. 3.2.4.e we can see how this is due to cascading decays from the tight clusters of small granules, particularly in the early time points. Unlike the smaller, gradual attrition, these splitting events are large enough to be directly observable by microscopy, and while we have recorded these events they are exceptionally rare, further suggesting that this is not the correct attrition model.

Out of these attrition modes, only the second case gives a good fitting to the experimental size distribution. Although it does tend to underestimate the number of smaller granules.

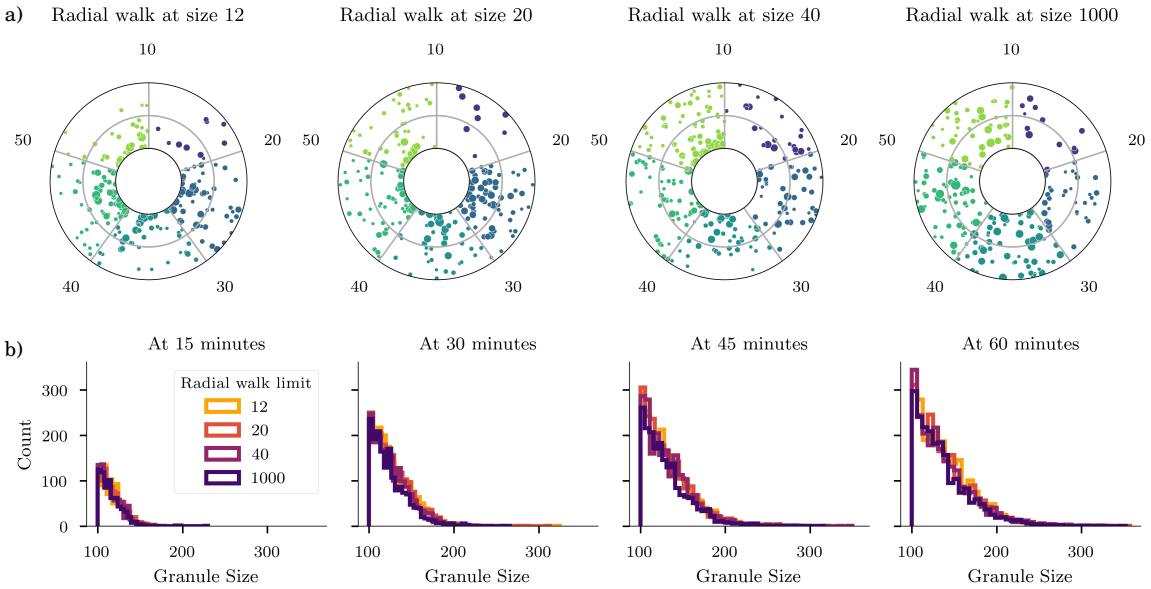

Figure 3.2.6: By changing the size at which the granules begin the radial walk we can influence the radial distribution, **(a)**, here we have used $p_n = 0.6$. The result on the far right correponds to the case where the radial walk is effectively prohibited. Although we see a large change in the radial distribution, there is little change in the size of the granules. In **(b)** we see that despite drawing the particles closer together, there is no siginificant change in the size distribution at the given time points, suggesting that the granules need not be brought closer together to promote merging.

3.2.3 Biased Walks

The cytoplasm is an incredibly viscous environment, and as the drag on granule scales with a surface area, we would expect that the random Brownian motion of the granules would become negligibly slow as the granule grows. However, granule movement has been observed experimentally, so we introduce a 1D radial random walk once the droplet gets above a specific size. This can be interpreted as the droplet attaching to a microtubule, or some other means of active transport. We also introduce a bias to this random walk, changing the probability that a granule will walk towards the nucleus, p_n. This biased walk is based on observation that microtubules may control stress granule movement [112, 48].

The role of microtubules is debated in the literature. It is unclear if the microtubules are essential in the early growth stages, where they could be used to bring the material together. Alternatively, they may play a role in the later stages, moving the granules together to aid in coalescence [57]. Finally, some authors claim flaws in the previous experimental work and that microtubules are unimportant to stress granule formation [113]. Due to the multitude of roles of microtubules in the cell, it is difficult to isolate the primary and secondary effects of microtubule disruption on stress granule formation.

We explore this effect by changing the size at which the clusters begin the radial walk, n_{radial}, with $p_n = 0.6$ in fig. 3.2.6.a. In the left-most figure, we use the default values where cluster begin to radial walk at size 12 and we can see that this causes larger granules to cluster towards the nucleus, as we intended. We then increase the size at which the granules begin the radial walk. In the right most figure, we start the radial walk at size 1000, as this is much larger than any granule formed, this prohibits the radial walk.

This biased radial walk causes a skew in the nearest neighbour distribution of the granules, making the coalescence of larger granules more likely. However, there is no significant effect on the size distribution shown in fig. 3.2.6.b across all radial walk sizes. While we are unable to rule out the effect of microtubules in the early stages of the model, we can say that coalescence of larger granules is unimportant in the size distribution of granules at later time points – while we increase the number of merging events, they remain insignificant in comparison to other growth methods.

3.2.4 Attrition scaling

The primary mode of growth in the cell is the absorption of particles from the background onto the granules, but in the later stages of the model, the background will no longer be super saturated and the granules will be in equilibrium with the surrounding area. Nevertheless, it is still possible for the mean size of the granules to increase after this stage, in a process known as coarsening.

The most obvious form of coarsening is by direct merging of the granules. However, as it is increasingly difficult for these larger granules to diffuse around the cytoplasm, combined with the limited time before the cell undergoes apoptosis from the stress response, these merging events are limited, as we have shown in the previous section.

The second coarsening effect is due to Ostwald ripening. LLPS occurs when it is energetically unfavourable for two components to mix, while the separation into droplets lowers the free energy of the system. There still exists an energy penalty due the interface between the droplets and the background. This surface tension is minimised in a system where the material is concentrated in a few large granules rather than many smaller ones, so to this effect we find that material is indirectly deposited from smaller granules onto the larger ones.

To implement this in the model, we can add a size dependence to the attrition rate. For a

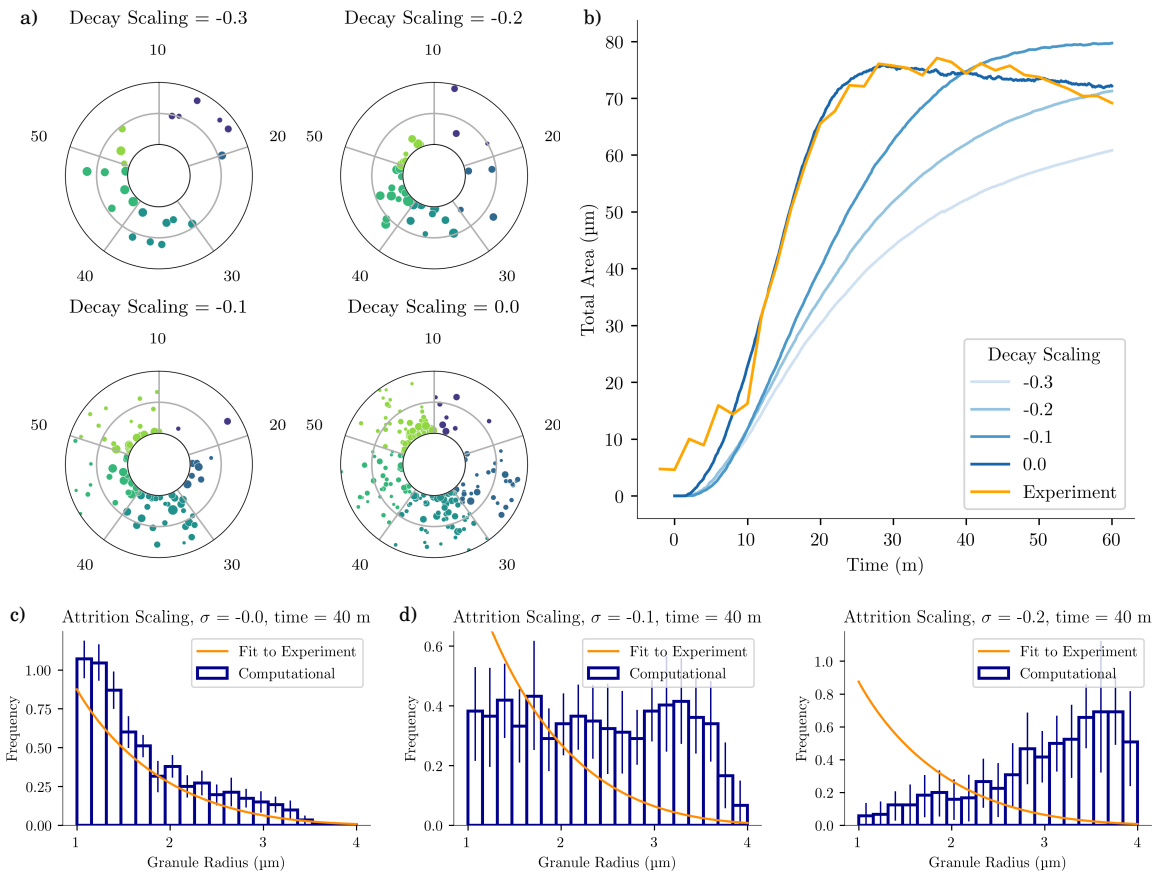

Figure 3.2.7: a) Top down views of the cell throughout the simulation for each of the attrition scaling values. As the magnitude of the attrition scaling increases the larger granules grow at the expense of the smallest granules, typical of a coarsening effect. b) We compare the (scaled) total area as a function of time. The experimental results best fit the simulations in the case of no attrition scaling. Introducing the effect causes a large disagreement. c) Size distribution of the granules at 40 minutes in the case of no attrition scaling, showing a good agreement with the experiment. d) The same experimental time point compared to cases with attrition. We see that the skew in the size distribution towards larger granules is conisitent with what we might expect with coarsening but not what with what we observe experimentally, suggesting that coarsening must be suppressed.

particle of size a, the decay rate, d_a is given by,

$$d_{\mathrm{a}} = d_0 a^{-\sigma\sim}, \tag{3.2.1}$$

where $\sigma > 0$ is a scaling factor. By increasing the magnitude of this scaling factor we are able to tip the equilibrium point further and force material to move from smaller granules to the larger granules.

As laid out in the introductory chapter, the magnitude of the Ostwald ripening scales with the radius of the granule, which would correspond to the case where $\sigma = 1/3$. This is also motivated by the idea of "sampling" of reactions allowing for a maturation of the granule. Over time the scaffold will go through many configurations and favour the stronger specific

interactions, making the older and more mature granule, more stable and less prone to attrition.

We see in fig. 3.2.7 that increasing the decay scaling leads to a skew in the size distribution towards larger granules, as they continue to grow at the expense of the smaller granules. However, any decay scaling factor leads to a poor fitting to the experimental data, suggesting that there is some effect suppressing the coarsening effects.

3.3 Discussion

3.3.1 Similar packages for modelling reaction-diffusion

There are other software packages implementing reaction-diffusion simulations. Some of the most well-used are Smoldyn [114, 115], STEPS [116] or MCell [117]. While these are robust and mature packages, we felt they were unsuitable for this work, in particular, most of these packages are designed to work with a well-defined set of reactions, not the continuous accumulation we required to model growing stress granules. Manipulating attrition is also not easily achieved and would likely require editing of the source code of the package. ReaDDy (version 2) seems to address these concerns. However the first release of this version was in April 2018 (with a second release later in the year [118]), which was too late to be used in this chapter [119]. Alternatively, reaction-diffusion may be approached numerically using the Smoluchowski equation, but this does not give us spacial information about the granule formation, and is highly non-trivial [120, 121]. Besides the computational expense, we also believe it would be non-trivial to capture the behaviour of the biased random walk for larger granules and the attrition mode changes in a phase field model.

3.3.2 Model conclusion

We see two significant divergences in our biological system from the LLPS model in a simple system. The first of which is that formation of an initial granule leads to an increase in the formation rate of granules in the local area, rather than a depletion like we might expect. Secondly, there does not seem to be significant coarsening of the granules beyond a point. Also, while we are unable to rule out the role of microtubules in the early stages of the model, we can say that coalescence of larger granules is unimportant in the size distribution of granules at later time points – while we increase the number of merging events, they remain insignificant in comparison to other growth methods.

Our model is not strictly time reversible, due to the attrition behaviour of the larger granules.

We find that the changing the decay behaviour to allow for reversible merging and splitting of larger granules is not supported by the computational model or experimental observations. Our choice of behaviour may bias the model into forming larger granules.

Suppression of coarsening is particularly surprising, as it is observed in many biological or passive LLPS systems [16]. One proposed mechanism behind the supression of Ostwald ripening in the cytoplasm is chemical interactions within the phase separating material [122, 123]. In the following section, we propose some extensions to the model that would allow us to investigate this in more detail.

3.3.3 Future Directions

We implemented an extension to the simulation to cover accumulation of multiple accumulating species which makes the model much more flexible; for instance, we might split the particles in the simulation into scaffolds or clients [70]. Proteins such as G3BP are dynamic and are replaced continuously within the granule. In contrast, some components such as FXR1 do not recover from photo-bleaching and so do not leave the granule. We might reflect this by reducing the rate of attrition of the scaffold when compared to the more dynamic first component. We could then investigate what changes this requires in the model by comparing our $\Delta\Delta$17-GFP+G3BP1 cell line to one over-expressing FXR1.

Another case of interest is that of Caprin1 and USP10, both are found to bind competitively to G3BP, respectively enabling and disabling its ability to take part in LLPS [54]. Mathematical modelling suggests that a transition between a soluble and insoluble state can suppress Ostwald ripening [124, 122]. It would be interesting to investigate if coarsening is encouraged in USP10 knockdown cells.

Therefore, we believe that there would be many interesting scenarios to investigate the two-component model: however, we found that introducing other accumulating species leads to an exponential growth in model parameters and concerns of overfitting. Not only would a second particle species require another set of parameters for the reaction rates and attrition rates, but also introduces many more parameters for the interactions between the species. Care would have to be taken to distinguish which parameters can be interpreted experimentally and which that are merely an artefact of the model.

This would require the collection of more data, the current bottleneck of which is the boundary drawing around the granules. Segmenting cells is a difficult problem, and it changes

significantly as the cytoplasmic G3BP1-GFP is drawn into granules, as we can see in the example microscope images in fig. 3.2.2 on page 51. Approaches in machine learning seem to make advancements here [125, 126], but it is still limited to cells that are mostly well separated. While this may be aided by fluorescent membrane dyes to highlight the cell boundary, this requires additional imaging that can lead to further photo-toxicity and bleaching.

Published work after this work was finished suggests that UBAP2L droplets may form the initial nucleation site of the stress granule [69], which we could account for in the model. However this is not required to match the distributions that we see. Our model also underestimates the frequency of the smallest granules and this may be improved in these more complex models.

3.3.4 Use in Vietri et al.

We were fortunate to be able to collaborate in the work of Vietri et al. [127] by performing the *in-silico* experiments. This paper covers the recovery of nuclei after membrane rupture, where it can be seen that the large primary nucleus can recover from a membrane rupture, whereas micronuclear rupture is irreversible and leads to membrane collapse. When the membrane is ruptured, ESCRT-III (endosomal sorting complex required for transport-III) forms membrane-bound filaments to help seal the rupture. For ESCRT-III to be recruited, CHMP7 must bind with LEMD2 sites on the inner nuclear membrane.

We were responsible for modelling the flow of CHMP7 protein into the nuclei upon rupture, where it binds to LEMD2 sites. The CHMP7-LEMD2 reaction is reversible and follows a binding and unbinding step, following the same implementation used in the coalescence and decay steps. We track the progress of the formation of bound CHMP7-LEMD2 sites as a function of time and the distance from the rupture as can be shown in figure 5.a,c (reproduced in fig. 3.3.1 and fig. 3.3.2 respectively) and figure 9.a-d in that paper. In the primary nucleus, we find that CHMP7 only binds around the rupture site, meaning ESCRT-III is only recruited around the rupture where it is needed, and the nucleus would be able to recover. However, in the micronuclear simulations, we find that CHMP7-LEMD2 sites rapidly begin to occupy the entire inner membrane, implying ESCRT-III begins to accumulate across the micronuclei. So instead of repairing the rupture, it distorts the membrane and leads to membrane collapse. Both of these scenarios agree well with the expected outcomes from the experimental results by the other authors. More details of these simulations are covered in the appendix.

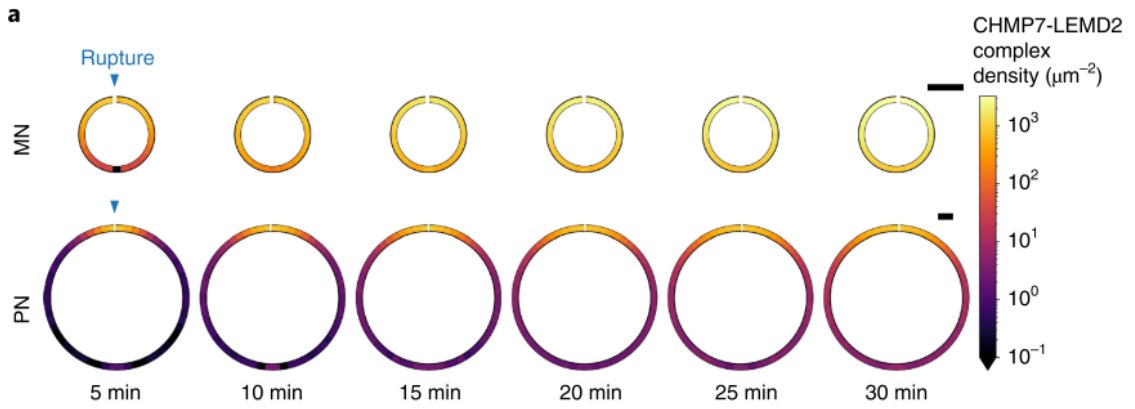

Figure 3.3.1: Figure 5.a from [127] showing the density of bound CHMP7-LEMD2 spreading along the inner nuclear membrane from a rupture. Scale bar 1 μm. In the top row we have micronuclei, where the membrane is rapidly saturated by CHMP7-LEMD2, leading to run away ESCRT-III accumulation and rupture of the micronuclei. In comparison, in the bottom row we have primary nuclei, where the LEMD2 sites are only occupied near the rupture, and ESCRT-III can repare the rupture.

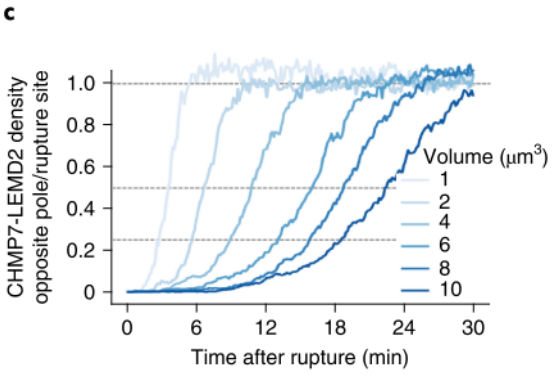

Figure 3.3.2: Figure 5.c from [127] showing the density of bound sites opposite to the rupture for micronuclei of various sizes. The density is given relative to the density of sites at the rupture. It can be seen that the smallest nuclei rapidly reach rapidily reaches equilibrium across the nuclei.

3.4 Appendix to Chapter 3

3.4.1 Generating random points on disks and spheres

A subtle point that caused significant issues when implementing the diffusion simulation involved correctly picking random points in 3D space, in particular:

1. We have to uniformly distribute the particles throughout the disk of our simulated cell when starting the simulation.
2. The particles have to move in a random direction when diffusing.
3. In the extension, we have to pick a random direction for a particle moving across the surface of a sphere.

3.4.1.1 Points on a disk

The simplest case is that of generating points on a unit disk[1]. This is used at the start of the simulation to place the particles within the cell, and it serves well to demonstrate the problem; a first approach may be to generate two uniformly distributed variables, $r \in [0, 1]$ and $\phi \in [0, 2\pi)$, and then give the position of the particles as

$$x = r \cos \phi \tag{3.4.1a}$$

$$y = r \sin \phi \ . \tag{3.4.1b}$$

However, when we generate points using this scheme, we see that this leads to particles more densely clustered around the centre of the disk, as is shown in fig. 3.4.1.a, it is essential to correct the distribution, as clustering the particles in this way leads to too many collisions at the beginning of the simulation.

1. A circle of radius 1.

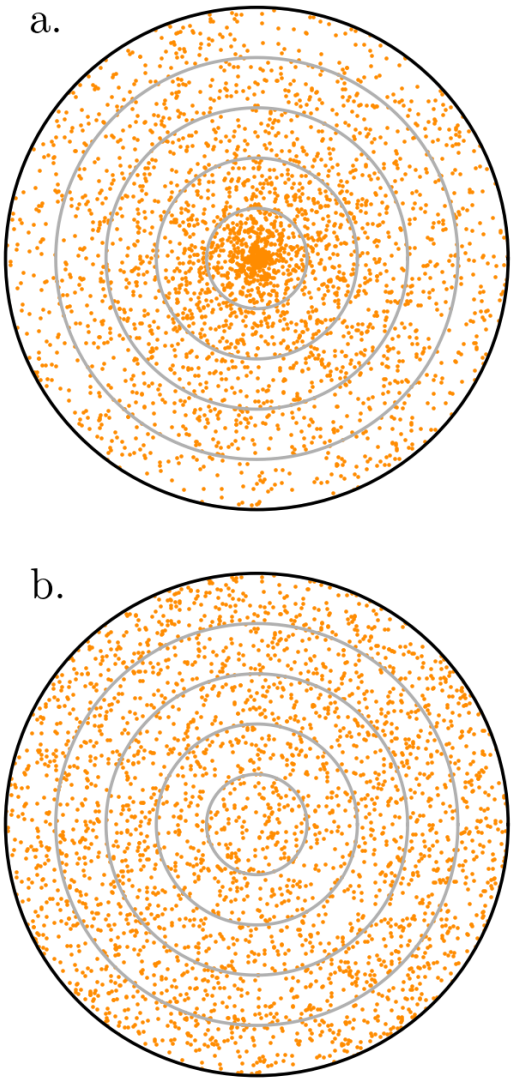

Figure 3.4.1: Choosing random points within the unit disk. **(a)** Naive scheme for generating points given in eq. (3.4.1a) causes uneven clustering of points toward the centre of the disk. **(b)** The term introduced in eq. (3.4.2a) corrects this distribution.

To see why this clustering occurs, we consider thin rings of width $\mathrm{d}r$ with areas

$$\mathrm{d}A = 2\pi r \, \mathrm{d}r \ ,$$

namely, the area of the ring grows linearly with the radius; we therefore require that the probability density function (PDF) of the chosen points should also scale with the radius. To correct for this we can integrate the PDF to give the cumulative distribution function, $\mathrm{CDF} = \int r \, \mathrm{d}r \propto r^2$. We can then apply the inverse of the CDF ($\sqrt{r}$) to the generated points:

$$x = \sqrt{r} \cos\phi \tag{3.4.2a}$$

$$y = \sqrt{r} \sin\phi \ , \tag{3.4.2b}$$

which for gives uniformly distributed points as shown in fig. 3.4.1.b.

In our model of the cell, we exclude a small region at the centre of the disk, which we take to be the nucleus. To account for this we treat it as a ring (or annulus) of outer radius, r_{out} and inner radius r_{in}. We can follow the same steps as above, to give the points

$$r' = \sqrt{\left[r_{\mathrm{max}}^2 - r_{\mathrm{min}}^2\right] r + r_{\mathrm{min}}^2} \tag{3.4.3a}$$

$$x = r' \cos\phi \tag{3.4.3b}$$

$$y = r' \sin\phi \ , \tag{3.4.3c}$$

for $r \in [0, 1]$ and $\phi \in [0, 2\pi)$ as before.

3.4.1.2 Free diffusion

When the particles jump during diffusion it moves a distance l in a random direction. This distance can be determined by picking a point on the surface of sphere.

In a similar manner to the above section, the area element of a (unit) sphere, $\mathrm{d}A = \sin\theta \, \mathrm{d}\theta \, \mathrm{d}\varphi$, is a function of $\$\theta$. This leads to clustering of points around the poles of the sphere where $\sin\theta$ is smallest [128]. However, if we make the substitution $u = \cos\theta$, so that $\mathrm{d}u = \sin\theta$, we can give the area element as $\mathrm{d}A = \mathrm{d}u \, \mathrm{d}\varphi$ which is independent of u.

If we, therefore, pick variables $u \in [0, 1]$ and $\varphi \in [0, 2\pi)$ we can convert these to Cartesian

coordinates following the definition from eq. (A.1)

$$x = \sqrt{1-u^2}\cos\theta \tag{3.4.4}$$

$$y = \sqrt{1-u^2}\sin\theta \tag{3.4.5}$$

$$z = u\ . \tag{3.4.6}$$

3.4.2 Implementing Vetri et al.

To model the nuclei, different model geometry and diffusion behaviour was required. The nucleus was modelled as a sphere with a 100 nm rupture, from which the CHMP7 may enter. The primary nucleus was a sphere of $400\,\mathrm{nm}^3$ and the micronuclei a sphere of $4\,\mathrm{nm}^3$. LEMD2 is located on the inner surface of the nucleus

Once CHMP7 binds to LEMD2, it is bound in place until the complex decays and new LEMD2 sites are introduced once a given percentage of the sites are occupied. We investigated the case of both free CHMP7 that diffuses in 3d space and CHMP7 that is bound to the nuclear membrane and can only diffuse on this surface. Both of these cases give the expected behaviour. The parameters used in this model were taken from multiple experimental sources; see Supplementary Table 1 in the paper for more detail.

3.4.2.1 Diffusion on a sphere

In the extension, we consider the movement of a particle across the surface of a sphere. As before, the particle moves a distance l, however, when the particle starts at an arbitrary position on the surface, it is difficult to calculate a non-biased random angle.

This problem is made much simpler when we consider a particle starting at the north pole of the sphere, $\mathcal{O}$, ($\varphi = 0$, $\theta = 0$) and move the particle a distance l, at random angle, along the surface of the sphere. This places the particle at a point $\mathcal{P}$ with a random azimuth φ and an altitude $\theta = l/R$.

To relate this to a jump starting at an arbitrary point on the surface $\mathcal{O}'$, there is a rotation $\mathcal{R}$ that would map the north pole on to the new starting point of the jump[2], $\mathcal{O} \to R\mathcal{O} = \mathcal{O}'$. Applying this same rotation to the particle, $\mathcal{P} \to \mathcal{R}\mathcal{P} = \mathcal{P}'$, gives a particle at position $\mathcal{P}'$ that is at a distance l from starting position of the jump at a uniform angle as we required.

2. The exact method of the rotation is not important; however, as we start the rotation at the origin this can be achieved rather simply by, say, rotating about the x-axis to the correct altitude, then rotating about the (global) z-axis to the correct azimuth.

Table 3.4.1: Table of parameters used in the simulation giving the overall best fit to experimental data.

Parameter	Value
$k_{1,1}$	$7 \times 10^4\,\mathrm{M/s}$
$k_{1,2}$	$5 \times 10^4\,\mathrm{M/s}$
$k_{1,3}$	$1 \times 10^5\,\mathrm{M/s}$
$k_{1,G}$	$2 \times 10^6\,\mathrm{M/s}$
$k_{2,2}$	$1 \times 10^6\,\mathrm{M/s}$
$k_{2,3}$	$1 \times 10^6\,\mathrm{M/s}$
$k_{2,G}$	$1 \times 10^6\,\mathrm{M/s}$
$k_{3,G}$	$1 \times 10^6\,\mathrm{M/s}$
$k_{G,G}$	$1 \times 10^6\,\mathrm{M/s}$
d_2	$1\,/\mathrm{s}$
d_3	$1 \times 10^{-1}\,/\mathrm{s}$
d_4	$3 \times 10^{-3}\,/\mathrm{s}$
D_{mono}	$1 \times 10^{-12}\,/\mathrm{s}$
D_{poly}	$1 \times 10^{-16}\,/\mathrm{s}$

Chapter 4

Measuring Stress Granule Properties Using Flicker Spectroscopy

4.1 Theoretical Description of Shape Fluctuations of LLPS Droplets

In the introductory chapter, we presented the concept of surface tension as an energy penalty for the interface between the two different liquids in a phase separating system. Surface tension plays a role in much of the behaviour in LLPS, including the early stages of droplet growth in the case of stress granules, where RNP is drawn in from the cytoplasm into droplets [129] as well as granule maturity and homeostasis between different types of membraneless organelles in the cell that are all postulated to arise as a consequence of LLPS [8]. There are several LLPS systems within mammalian cells: such as stress granules, p bodies, germ granules and aggresomes within the cytoplasm and nucleoli and Cajal bodies within the nucleus [35]. Interactions between the different LLPS bodies will become increasingly important in understanding their role in the cell. As discussed in sec. 1.1.6; in the simplest case, surface tension controls the amount of contact—or lack thereof—between two droplets. An example of this can be seen in the interactions between stress granules and p-bodies, where the contact allows transcripts to be passed from the stress granules into the p-bodies for degradation [12, 35].

It also allows for more complex ternary structures such as one droplet species engulfing the other. The theoretical background for such structure is provided [2, 20, 27] and demonstrated in-vitro with protein droplets in [130, 35] and after phase separation within RNP droplets in [131, 71]. We can also observe these similar structures in stress granules directly in-vivo, as shown in fig. 4.7.4. Examples of these different morphologies can be seen in fig. 1.1.5. There are three surface tension values to consider in the dual separating system: each of the droplets will have an independent surface tension with the background, and additionally, a surface tension penalty between the two droplets. When two droplets are in contact, the surface tension between them can be calculated by measuring the contact angles between the droplets as shown elegantly in [130]. Measuring the surface tension between a droplet organelle and

the cytoplasm in a biological system such as a live cell presents unique challenges, which we address in our work presented here.

4.1.1 Measuring surface tension

Although phase separation in biological systems is a rapidly growing field, there is a lack of quantitative data on the physical properties of stress granules—or other LLPS droplets—in the literature.

In this chapter, we focus on surface tension. A simple estimate for the surface tension is given by [132]

$$\sigma \approx k_{\mathrm{B}} T/\zeta^2 \ , \tag{4.1.1}$$

where T is the temperature of the system, which when multiplied by the Boltzmann constant, k_B, gives the thermal energy scale. The interpretation of the correlation length, ζ, is more complicated: the full derivation of this approximation is beyond the scope of this work but is given in [133, 134]; the primary assumption made is that the minimum width of a ripple across the granule surface can be no smaller than the molecules involved, and this defines the interface roughness or correlation length, ζ. However, while this interpretation may be straightforward when considering simple liquid mixtures, it is unclear how ζ would be calculated when considering a stress granule consisting of many hundreds of different proteins, all with complex interactions and folding. So this approximation can only be used to give an order of magnitude estimate of the granule surface tension. For instance, this approximation has previously been used by Brangwynne and colleagues in the estimation of the surface tension of biological LLPS organelles; giving a value of $\sigma \sim 10\,\mu\mathrm{N/m}$ for *X. laevis* oocyte nucleoli [10].

The estimated surface tension can further be used to calculate the viscosity of the droplet η. The typical timescale for two droplets to fuse after contact, τ, is related to the droplet size l, viscosity η and surface tension σ, by $\tau = l\eta/\sigma$. By analysing the merging dynamics between two droplets, if the surface tension is known, this allows us to estimate the droplet viscosity, as is done in [10] above. This leads to an estimated viscosity of $\eta \approx 1 \times 10^3\,\mathrm{Pa\,s}$.

Alternatively, if the droplet viscosity can be found using another approach, the above relation provides a way to estimate the surface tension. For example, this was done with *c. elegans*

P granules[1] to give a surface tension value of $\sigma = (1.0 \pm 0.2)\,\mu\mathrm{N/m}$, where the viscosity is measured using micro-rheology in-vitro [2].

Measurement of surface tension of droplets is possible in in-vitro systems with a high degree of accuracy. In [135], Jawerth et al. embedded two beads in a PGL-3 protein droplet. PGL-3 is a major component of P granules, and undergoes LLPS to produce droplets. Two optical traps were used to manipulate the droplet via the beads and measure its response as a function of frequency; from which they were able to measure many properties of the granule, including surface tension and viscosity.

Using this method they demonstrated a significant change in the surface tension as a function of salt concentration in the medium; demonstrating that surface tension does not depend on just granule composition, but also on the material surrounding the granule, and hence highlighting the need for a method to examine biological compartments within the cytoplasm. Unfortunately, while these methods allow us to accurately measure a number of stress granule proprieties, they are only possible in non-living systems, in highly controlled in-vitro environments.

We therefore investigate flicker spectroscopy (FS) approach to assess its suitability to be used to measure LLPS organelle properties in live cells.

4.1.2 Flicker Spectroscopy

The central idea of flicker spectroscopy is to study fluctuations in the shape of the droplet using microscopy and use them to infer material properties of the droplet. More specifically, in relation to surface tension, if there is a higher interfacial tension between the regions, the surface will be harder to deform. However, as we will see in the following sections FS provides much more insight into the properties of the granules. For instance, we find that, to explain the fluctuation spectrum of the droplet, we need to include a bending energy term.

In the rest of this chapter, we start by covering how we describe the fluctuations across the surface of a droplet and then move onto how these may be related to the surface tension and bending rigidity.

This method has been used successfully within the soft matter community to study vesicles in-vitro, but it has not been applied to biological LLPS droplets, we therefore use sec. 4.2 to discuss the steps required to adapt this model and how we used simulations and additional

1. Not to be confused with mammalian p-bodies covered elsewhere in this text.

experiments to verify our approach.

As covered in the introductory section 1.1.6, internal structure of the granules has been a topic of great interest and debate [65, 37, 71]; a strength of flicker spectroscopy is that the method is independent of possible shell-core structures within the granule.

4.1.2.1 Describing the surface

It is typical to describe the surface of a granule, S, as a small perturbation, u, on the surface of a sphere of radius, R,

$$S(\theta, \varphi, t) = R[1 + u(\theta, \varphi, t)] \ . \tag{4.1.2}$$

We may then write the perturbation as a weighted sum of spherical harmonics Y_{lm},

$$u(\theta, \varphi, t) = \sum_{l=2}^{\infty} \sum_{m=-l}^{l} Y_{lm}(\theta, \varphi) \mathcal{U}_{lm}(t) \ , \tag{4.1.3}$$

where $\mathcal{U}_{lm}(t)$ is the magnitude of the given spherical harmonic term[2]. It is by changing the values of these terms that we are able to describe our surface. l and m are the indices of the spherical harmonic terms. In general, $l \geq 0$ and $-l \leq m \leq l$. However $l = 0$ corresponds to a uniform spherical term and $l = 1$ to translations, so we are not interested in these terms.

The perturbations of the surface of a sphere are illustrated in fig. 4.1.1 for each of the spherical harmonic modes $2 \leq l \leq 5$. The increasing (angular) frequency of the perturbations can be seen as l increases.

Breaking down the surface into spherical harmonics in this manner is useful, as it allows us to calculate the energy of each of the individual spherical harmonic terms separately and then sum them to give the total energy of the system, as we cover in the following section.

4.1.2.2 Helfrich Hamiltonian

From the introductory chapter, we know that there is an energy cost per unit area, σ for the interface between the stress granule and the cytoplasm. If, in our first approach, we assume that this is the only energy contribution, then the total energy of the surface, $\mathcal{H}$, is given as

$$\mathcal{H} = \int_s \mathrm{d}A \, \sigma. \tag{4.1.4}$$

2. See appendix A.2 for the normalisation used.

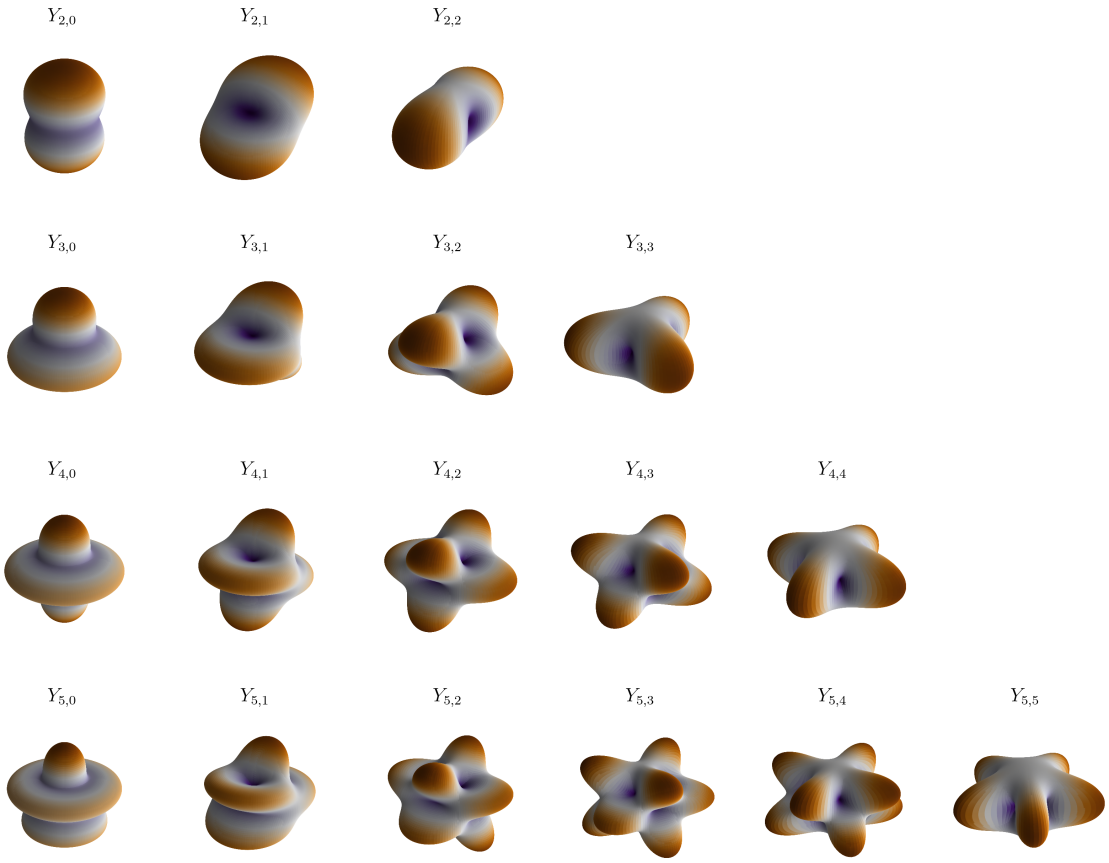

Figure 4.1.1: Spherical harmonic modes perturbing the surface of a sphere. For clarity in this figure, we normalise the spherical harmonic terms to have the same maximum magnitude. Regions that have been perturbed outwards from the original position are coloured in orange, and those that are moved inwards are coloured purple.

However, we find that this simple description is insufficient to account for the fluctuation spectra we measure in stress granules (sec. 4.5.2), and so we instead make use of the Helfrich Hamiltonian. This includes an energy cost for both deforming and stretching the surface,

$$\mathcal{H} = \int_S \mathrm{d}A \left[\frac{\kappa}{2}(H - 2c_0)^2 + \sigma\right] \tag{4.1.5}$$

where, H is the total curvature at a point and c_0 is a spontaneous curvature[3], that we will take to be zero for the rest of the analysis. κ is the bending rigidity; a measure of the difficulty of bending the surface away from its preferred, spontaneous curvature. There is also a contribution to the total energy from the Gaussian curvature, $\mathcal{K}$, however, from the Gauss-Bonnet theorem, this term is a topological constant. Therefore, it is constant for all

3. The total curvature is defined to be the sum of the principal curvatures $H = (c_1 + c_2)$. The curvatures can be measured as the inverse of the radii of circles that fit the surface shape at a given point.

shapes that we will consider, and has no further role in this analysis. The Helfrich Hamiltonian is most commonly used to discuss the mechanics of lipid bilayers. This is a very different system to our stress granules. However it can be shown that the Helfrich Hamiltonian provides the only way that the curvatures can be meaningfully combined to describe the deformation energy of a surface (to second order) [136, 137].

It can be shown that the energy required for each fluctuation mode, defined in eq. (4.1.3), is given by

$$E_l = \frac{\kappa}{2} \sum_{m=-l}^{l} |\mathcal{U}_{l,m}|^2 (l+2)(l-1)[(l+1)l + \bar{\sigma}] \ , \tag{4.1.6}$$

where $\bar{\sigma} \equiv \sigma R^2/\kappa$ is the (dimensionless) reduced surface tension. We note that there is no dependence on the order of the spherical harmonics, m. The exact derivation of eq. (4.1.6) is provided in [138, 139]. To illustrate the steps involved, we derive the equivalent spectrum for the simpler planar spectrum in appendix sec. 4.7.1.

The equipartion theorem [139] states that all of these modes should have the same energy, corresponding to the thermal energy of the system, $E_l = k_\mathrm{B}T/2$, giving an expected spectrum of

$$\left\langle |\mathcal{U}_{lm}|^2 \right\rangle = \frac{k_\mathrm{B}T}{\kappa} \frac{1}{(l-1)(l+2)[l(l+1)+\bar{\sigma}]} \ , \tag{4.1.7}$$

where we have taken the time average of the fluctuations, $\left\langle |\mathcal{U}_{lm}|^2 \right\rangle$.

4.1.2.3 Projections onto the plane

Equation (4.1.7) above contains information about the components of the 3D spherical harmonics. However, in practice we are only able to image a single plane of the granule[4] and so we must relate the magnitudes of the 3D spherical harmonic terms, $\mathcal{U}_{lm}$, into terms that we can observe directly.

If we assume that we are imaging the equatorial plane of the granule, then we see a cross section of the perturbations, $\hat{u}$, which without loss of generality, we may give as the $\theta = \pi/2$ plane, or more explicitly: $u(\pi/2, \varphi, t) \equiv \hat{u}(\varphi, t)$.

In a similar manner to before, we decompose the perturbation cross section down into

4. Attempts can be made to measure the entire granule, however, it is typical for microscopes to have much worse resolution in the "z"-axis and requires movement of the imaging stage, which slows data gathering.

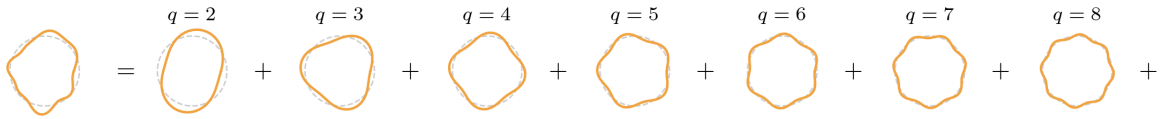

Figure 4.1.2: Decompostion of the shape peturbation in the equatorial plane into Foruier modes. The mode number, q, corresponds to the number of maxima in the mode. By controlling the amplitude of these modes, $\mathcal{V}_q$, we are able to represent any radial function.

Fourier components

$$\hat{u}(\varphi, t) = \sum_{q=2}^{\infty} \mathcal{V}_q e^{-iq\varphi} \ , \tag{4.1.8}$$

where q is the vibration mode and $\mathcal{V}_q$ is the amplitude of that mode that we can measure using microscopy. q can be interpreted as the number of maxima in the surface and q must be a positive integer to ensure circular periodicity. Further, in a similar manner to the spherical harmonics l terms; the $q = 0$ mode corresponds to a uniform increase in radius or "breathing", this can be seen as part of the uniform sphere rather than the perturbation and $q = 1$ translates the surface, and so we take terms $q > 2$ only. An example of a decomposition of a surface is shown in fig. 4.1.2 along with the definition of the vibration modes.

These terms are computed via a Fourier transform,

$$\mathcal{V}_q(t) = \frac{1}{2\pi} \int_0^{2\pi} \hat{u}(\varphi, t) e^{iq\varphi} \, \mathrm{d}\varphi \ . \tag{4.1.9}$$

Importantly, this cross section of the surface must match the definition of the full surface in eq. (4.1.3). This constraint leads to

$$\mathcal{V}_q = \frac{1}{2\pi} \int_0^{2\pi} \sum_{lm} \mathcal{U}_{lm} Y_{lm}(\pi/2, \varphi) e^{iq\varphi} \, \mathrm{d}\varphi \tag{4.1.10a}$$

$$\mathcal{V}_q = \frac{1}{2\pi} \int_0^{2\pi} \sum_{lm} \mathcal{U}_{lm} N_{lm} P_{lm}(\cos \pi/2) e^{il\varphi} e^{iq\varphi} \, \mathrm{d}\varphi \ , \tag{4.1.10b}$$

where P_{lm} and N_{lm} are the associated Legendre polynomials and a normalisation factor respectively, the definitions of which are given in section A.2.

Solving this (see e.g. [139, 140]), we get a relation between the time averaged magnitudes of the observable fluctuations, $\mathcal{V}_q$, and $\mathcal{U}_{lm}$, as

$$\left\langle |\mathcal{V}_q|^2 \right\rangle = \sum_{l=q}^{l_{\max}} \left\langle |\mathcal{U}_{lm}|^2 \right\rangle N_{lm}^2 P_{lm}^2(\cos \pi/2) \ . \tag{4.1.11}$$

This sum converges rapidly [141, 139], and we find that $l_{\max} = 75$ is sufficient for our work. Substituting, eq. (4.1.7) into eq. (4.1.11), we obtain

$$\left\langle |\mathcal{V}_q|^2 \right\rangle = \frac{k_{\mathrm{B}}T}{\kappa} \sum_{l=q}^{l_{\max}} \frac{P_{lm}^2(0) N_{lm}^2}{(l-1)(l+2)[l(l+1)+\bar{\sigma}]} \ , \tag{4.1.12}$$

this allows us to relate the experimentally observable fluctuation terms.

4.1.3 Outline

In the next section, we will investigate the theory behind the flicker spectroscopy method and, in particular, verify our implementation of the theory. Section 4.3 covers the extraction of the experimental data from the microscopy data. In section 4.4, we introduce a package, granule-explorer, that aims to allow the reproduction of this work in other groups and across other LLPS systems. Finally, we perform the analysis on experimental data in section 4.5, across a number of different treatments and mutant cell lines. The discussion of these results and the overall method is given in sec. 4.6.1.

4.2 Verification of the Flicker Spectroscopy Method for Applications in LLPS droplets

Flicker spectroscopy has not previously been applied to LLPS droplets in-vivo, and there is a lack of measurements for the surface tension of LLPS droplets in the literature that we can use to check for agreement. Therefore, here we create several benchmark simulations. We start from the base case of a flat disk and increase the complexity of each simulation until we are modelling a fluctuating droplet. This allows us to be sure that not only is each step correctly implemented in the code, but also investigate the assumptions in each step. This is particularly important when we investigate the quasi-spherical base shape of the granule, as this is not typically considered in the literature. We also investigate the conversion given in eq. (4.1.11) between the 3D spherical harmonics terms and 2D Fourier terms that we experimentally observe.

After we have verified that we can achieve the correct results from simulated data, there are two experimental challenges unique to stress granules that we must address. Granules are a much more challenging system to image than the vesicles typically investigated in the soft matter community. This is due to two main factors. First, stress granules are much smaller than vesicles. Second, the cytoplasm is a much nosier environment than an in-vitro system. We therefore wish to ensure that the fluctations we observe are indeed due to the thermal fluctuations of the granule surface, and not from microscopy noise or from incorrectly interpreting random rotations of the stress granules as their shape fluctuations.

4.2.1 Simulating a fluctuating droplet

Extracting the physical properties of the granules is done in two steps. The first steps are to measure the fluctation spectrum from each granule in the microscope images. The second set of steps is to analyse this spectrum and extract the values of surface tension and bending rigidity.

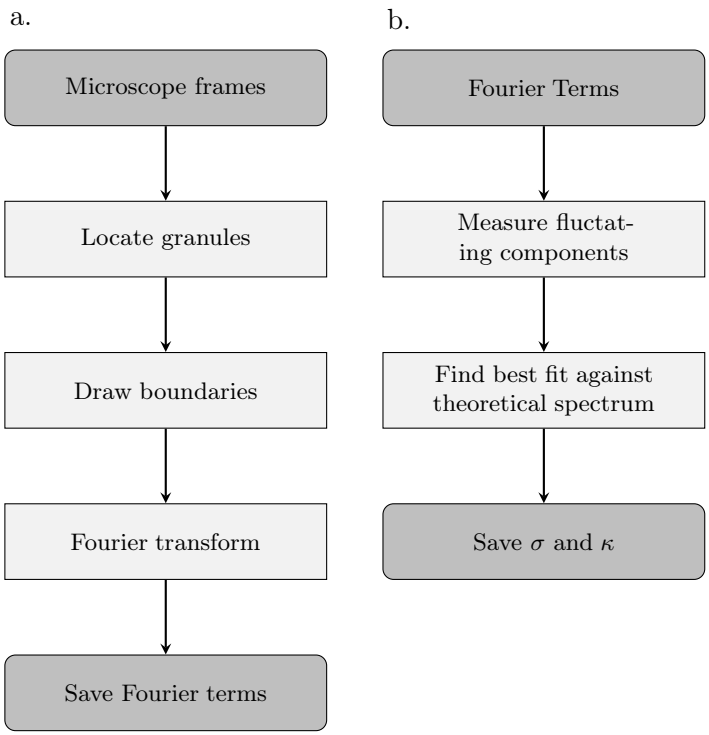

Figure 4.2.1: (a) Flowchart of the first stage of the analyis, starting with the microscope images and ending with the Fourier terms for each frame saved to disk. **(b)** From these saved Fourier terms we calculate the experimental fluctuation spectrum and compare this to the expected theoretical spectrum.

The first steps of the analysis are given in fig. 4.2.1.a. For each of the microscope frames in the time series, the granules are located using the Difference of Gaussian method[1] and the granule boundaries are located with sub-pixel resolution. We then Fourier transform the shape of each granule to identify the relevant perturbation modes.

The second steps of the analysis are given in fig. 4.2.1.b. The experimental fluctuation spectrum for each granule is calculated by aggregating the measured perturbation modes across all time points. This experimental spectrum is then compared against the theoretical spectrum given in eq. (4.1.12). The L-BFGS minimisation algorithm is used to give the best fit between the spectra as a function of surface tension and bending rigidity. The values of σ and κ giving the best fitting are taken to be the measured surface tension and bending rigidity for that granule.

The first stage of the analysis, locating the granules within the image and boundary detection can be verified well by eye and so the following simulations in this section are concerned mostly with the second stage of the analysis. We will verify that we are able to correctly recover the experimental spectrum from a fluctuating disk and the comparison of this against the

1. Materials and methods, sec. 2.2.1

theoretical spectrum.

4.2.1.1 Flat disk

Here, we focus on the Fourier transform step, in which we will typically analyse the equatorial contour of an LLPS droplet to identify the amplitudes of different fluctuation modes as described by Eq. (1.7). A simple but sufficient test is to simulate a circular disk with base radius R_0 which we perturb with the following Fourier modes:

$$R(\varphi) = R_0(1 + \hat{u}(\theta)), \tag{4.2.1}$$

where $\hat{u}$ is given by,

$$\hat{u}(\theta) = \sum_q \mathrm{Re}\left(e^{iq\theta}\mathcal{V}_q\right) \tag{4.2.2a}$$

$$= \sum_q a_q \cos q\theta - b_q \sin q\theta \ , \tag{4.2.2b}$$

where we have expanded the complex amplitude by $\mathcal{V}_q = a_q + ib_q$. In this test, we may introduce different perturbation modes and amplitudes. Importantly, the Fourier transform step in our analysis must return the same perturbation modes and amplitudes, as well as disk radius, compared to the values initially introduced.

4.2.1.2 Fluctuating disk

Any fluctuating LLPS droplet will have shape deformation that is time dependent. This time dependence can in general be very complex, and for our purpose, the key quantities to capture are the time averages of the square of the fluctuation amplitudes, $\langle|\mathcal{V}_q|^2\rangle$, as these are what we compare to the expected theoretical spectrum.

The validation test we have designed is to analyse simulation data corresponding to a circular disk fluctuating with Fourier mode q and amplitude

$$\mathcal{V}_q(t) = \mathcal{V}_{q,0}\cos(w_q t + \delta_q). \tag{4.2.3}$$

Here, w_q and δ_q are assumed to be constants. This choice is particularly useful because more complex form of $\mathcal{V}_q(t)$ can in principle be expanded as a Fourier series in the time-frequency

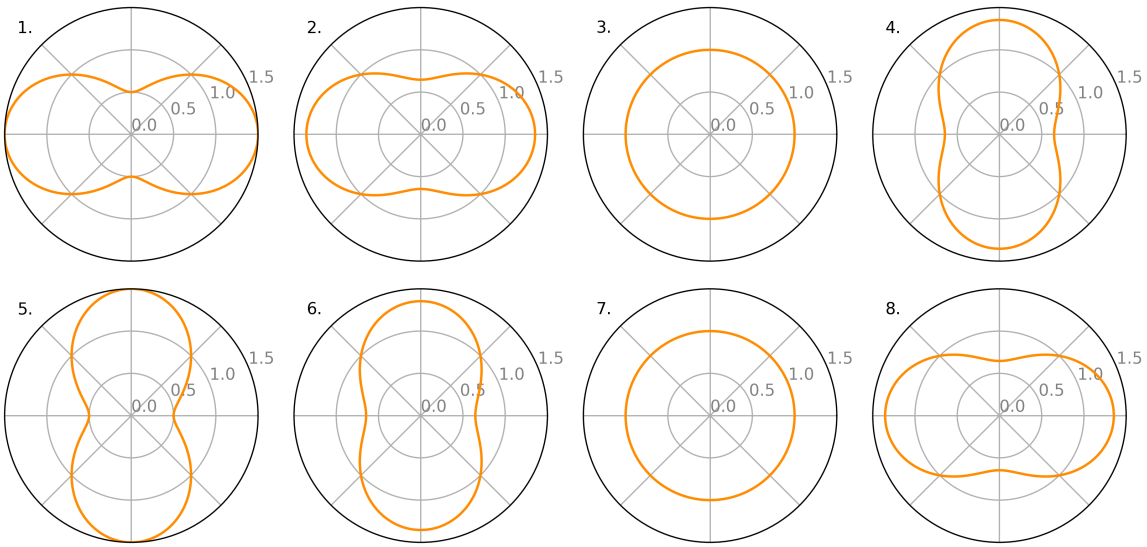

Figure 4.2.2: A round disk fluctating over a period of mode $q = 2$, as given by eq. (4.2.3). The indices (1-8) show advancing time.

domain, although detailed analysis is beyond the scope of this work.

For a typical analysis, we will assume that the data has been acquired for a time, T, much longer than the period of any relevant frequency in the problem. For the form given in eq. (4.2.3), we have

$$\langle |\mathcal{V}_q|^2 \rangle = \frac{1}{T} \int_0^T |\mathcal{V}_q|^2 \, \mathrm{d}t \tag{4.2.4a}$$

$$= |\mathcal{V}_{q,0}|^2 \frac{1}{T} \int_0^T \cos^2 \omega_q t \, \mathrm{d}t \ . \tag{4.2.4b}$$

The term in the integral, I, can be evaluated as

$$I(T) = \left[\frac{t}{2} - \frac{\sin(2\omega_q t)}{\omega_q} \right]_0^T ; \tag{4.2.5}$$

and using our assumption that $T \gg \omega_q$, we get $\lim_{T\to\infty} I = T/2$. Correspondingly, we have,

$$\langle |\mathcal{V}_q|^2 \rangle = \frac{1}{2} |\mathcal{V}_{q,0}|^2 \ . \tag{4.2.6}$$

To test our implementation, we create a disk for each time point, as shown in fig. 4.2.2, from which we then extract the Fourier terms and calculate the time average of these values. We have introduced perturbations with only one q-mode at a time, as well as multiple q-modes simultaneously. In all cases, we find that our implementation behaves as expected.

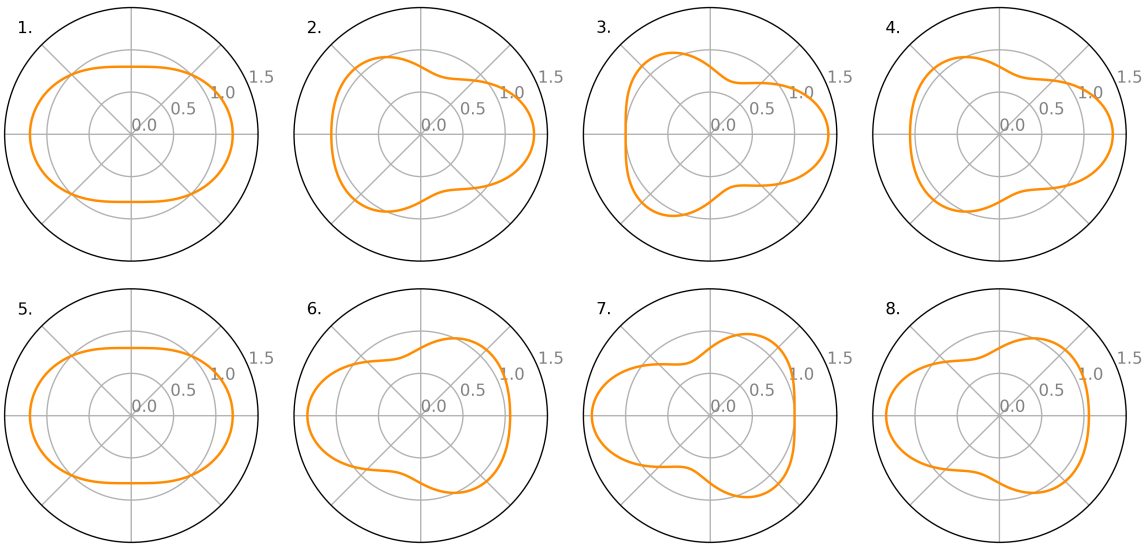

Figure 4.2.3: A disk peturbed with a fluctating $q = 3$ and a constant $q = 2$ mode. Upon applying eq. (4.2.8) we can separate out these terms.

4.2.1.3 Quasi-spherical disk

In the above subsections, we have assumed that the surface can be described as perturbations on top of a disk. Provided that we image for long enough, the mean of the perturbations will be zero. However, in our microscopy images we can see that is a poor description for a granule, as the mean shape of the boundary is far from circular. We, therefore, investigate if we can correctly recover the fluctuating terms from a disk with an irregular, or quasi-spherical, base shape.

We extend our description of the fluctuating terms in eq. (4.2.3) to include fluctuating terms, $\mathcal{F}_q$, and constant components, $\mathcal{C}_q$, that do not change with time,

$$\mathcal{V}_q(t) = \mathcal{F}_q \cos\left(\omega_q t + \delta\right) + \mathcal{C}_q \ . \tag{4.2.7}$$

An example of such a surface with a fluctuating $q = 3$ mode and constant $q = 2$ mode is shown in fig. 4.2.3.

Pécréaux et al. [142] also considers this problem in the context of quasi-spherical vesicles, and gives the mean squared magnitude of the fluctuating terms as

$$|\mathcal{F}_q|^2 = \left\langle |\mathcal{V}_q|^2 \right\rangle - |\langle \mathcal{V}_q \rangle|^2, \tag{4.2.8}$$

where the final term on the right hand side can be interpreted as square of the constant

contribution to the perturbation spectrum, $|\langle \mathcal{V}_q \rangle|^2 = \mathcal{C}_q^2$.

Example test cases are shown in table 4.2.1. In case (i), we demonstrate a disk that only has fluctuating components. This is identical to the test in the previous subsection, in which no correction is required. As expected, the total fluctuations and eq. (4.2.8) give the correct values. Case (ii) gives a granule that has no fluctuating components and case (iii) gives a granule that has both static and fluctuating components. In these cases only eq. (4.2.8) is able to correctly distinguish the static and fluctuating components.

We are therefore confident that we are correctly measuring the experimental Fourier spectrum from our simulated disk.

Table 4.2.1: Extracted Fourier terms for three sample disks: Disk (i) contains only fluctuating terms, disk (ii) does not fluctuate and disk (iii) has a combination of fluctuating and constant terms. Measuring total fluctations cannot distguish between the fluctuating and constant modes, leading us to overestimate the magnitude of the fluctating component.

		Expected		$\langle \lvert\mathcal{V}_q\rvert^2 \rangle$	eq. (4.2.8)	
Disk	Order	Fluct	Fixed	Total	Fluct	Fixed
(i)	2	0.320	0.000	0.320	0.320	0.000
	3	0.180	0.000	0.180	0.180	0.000
	4	0.080	0.000	0.080	0.080	0.000
(ii)	2	0.000	0.640	0.640	0.000	0.640
	3	0.000	0.360	0.360	0.000	0.360
	4	0.000	0.160	0.160	0.000	0.160
(iii)	2	0.020	0.250	0.270	0.020	0.250
	3	0.045	0.040	0.085	0.045	0.040
	4	0.005	0.040	0.045	0.005	0.040

4.2.1.4 Fitting to a granule-like spectrum

We have shown that we can recover the magnitudes of the fluctuating perturbation terms from a sample disk. In a physical system we expect a fluctuation spectrum that depends on the surface tension and bending rigidity of the surface. This subsection tests that we can recover information about the surface tension and bending rigidity from our fitting to the recovered fluctuation spectrum.

In the appendix sec. 4.7.1 we derive the fluctuation spectrum for a flat surface. This follows a similar spectrum as the spherical case, but avoids the complex conversion terms involved in spherical geometry. In this case, the perturbation spectrum is given by

$$\langle |\mathcal{V}_q|^2 \rangle = \frac{k_\mathrm{B}T}{\kappa q^4 + \sigma q^2} \ . \tag{4.2.9}$$

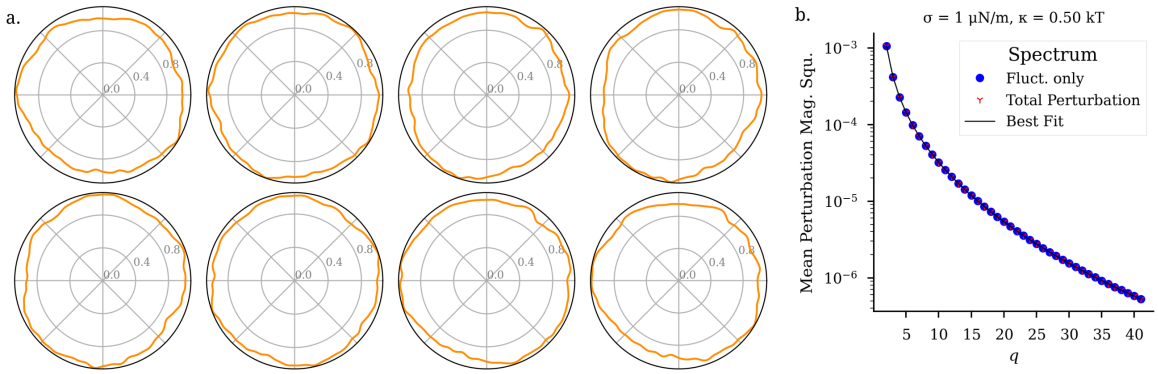

Figure 4.2.4: (a) Snapshots of a fluctuating disk corresponding to a stress granule with $\sigma = 1\,\mu\text{N/m}$ and $\kappa = 0.5k_BT$. **(b)** Analysing the fluctuation spectrum returns the expected surface tension and bending rigidity values.

We, therefore, simulate a disk with a fluctuation spectrum corresponding to eq. (4.2.9). The amplitude of each fluctuation mode, $\mathcal{V}_{q,0}$, for $q \in (2, q_{\text{max}})$ is given by $\sqrt{\langle|\mathcal{V}_q|^2\rangle}e^{i\varphi}/2$. The factor of 1/2 accounts for the time averaging, as is shown in eq. (4.2.6). $e^{i\varphi}$ is a random complex phase that prevents alignment of the perturbations.

Examples of these simulated disks are shown in fig. 4.2.4.a. From two hundred such snapshots, we take the Fourier transform of these boundaries and average them to extract the simulated "experimental" fluctuating and constant spectrum using eq. (4.2.8). We then find the best fit values of σ and κ and compare these to the values used to create the disk.

We get exact recovery of the provided surface tension and bending rigidity in all cases, with an example shown in fig. 4.2.4 for a surface tension of $\sigma = 1\,\mu\text{N/m}$ and bending rigidity of $\kappa = 0.5k_BT$. The surface tension values correspond to that of P-granules in-vitro as discussed in the Introduction, sec. 4.1.

Arbitrary constant terms may also be added to the spectrum, which significantly changes the shape of the granule, as shown in fig. 4.2.5. However, we can separate these fluctuating and fixed terms easily, leading to the correct recovery of the provided surface tension and bending rigidity as is shown in fig. 4.2.5.b.

4.2.1.5 Fluctuation spectrum of a spherical droplet

The final, and most important, simulation step is to verify that we are able to extract the expected surface tension and bending rigidity from simulated spherical droplets. The spectrum

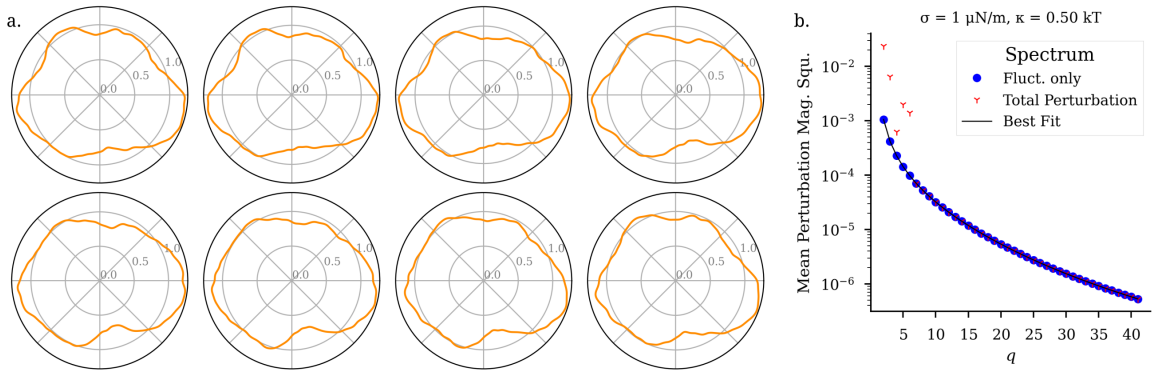

Figure 4.2.5: Introduction of constant components in the first five fluctuation modes on top of the fluctation spectrum. **(a)** The constant components significantly effect the shape of the granule. **(b)** There is a significant difference between the full perturbation spectrum (red tri-points) and the fluctuating terms (blue dots), but fitting to the fluctuating spectrum is unaffected and returns exactly the expected values.

of the 3D model, given in terms of spherical harmonics, is

$$\left\langle |\mathcal{U}_{l,m}|^2 \right\rangle = \frac{k_\mathrm{B}T}{\kappa} \frac{1}{(l-1)(l+2)[l(l+1)+\bar{\sigma}]} \ . \tag{4.2.10}$$

We are not able to observe all of these terms directly, so instead we use a conversion into the Fourier terms at the equator

$$\left\langle |\mathcal{V}_q|^2 \right\rangle = \sum_{l=q}^{l_\mathrm{max}} \left\langle |\mathcal{U}_{l,q}|^2 \right\rangle N_{l,q}^2 P_{l,q}^2(\cos(\pi/2)) \ . \tag{4.1.11 revisited}$$

This test verifies that we correctly convert from the 3D spherical harmonics into the observed fourier terms at the equatorial plane, and that we then recover the expected values of σ and κ after fitting.

Similarly to before, we create a perturbed surface, u, using a set of perturbation magnitudes, $\mathcal{U}_{l,m}$, given in eq. (4.2.10),

$$u(\varphi, \pi/2) = \sum_{l,m} \mathcal{U}_{l,m}(t) Y_{l,m}(\varphi, \pi/2) \ . \tag{4.1.3 revisited}$$

Next, we compare the fluctuation spectrum computed in two different ways. In the first approach, we create the fluctuating 3D sphere from the given perturbation magnitudes, which is then sampled around the equatorial plane to give a fluctuating boundary. At this stage we may also introduce arbitrary constant terms. For each of these frames we perform a Fourier transform to get the perturbation modes, $\mathcal{V}_q$, and we then aggregate these modes across the

frames to calculate the magnitudes of the fluctuating and constant modes, $\mathcal{F}_q$ and $\mathcal{C}_q$. This is shown by downwards path of fig. 4.2.6. In the second approach, we directly compute $\mathcal{F}_q$ and $\mathcal{C}_q$ from $\mathcal{U}_{l,m}$ using eq. (4.2.6) and eq. (4.1.11) (right path of fig. 4.2.6). It is important that these values are consistent.

Finally, we fit $\mathcal{F}_q^2$ to obtain the values of σ and κ. This is shown in fig. 4.2.7, for the example case of $\sigma = 1\,\mu\text{N/m}$ and $\kappa = 0.5 k_B T$. We see that we once again retrieve exactly the values used to create the sphere, even in the presence of constant terms that distort the base of the granule.

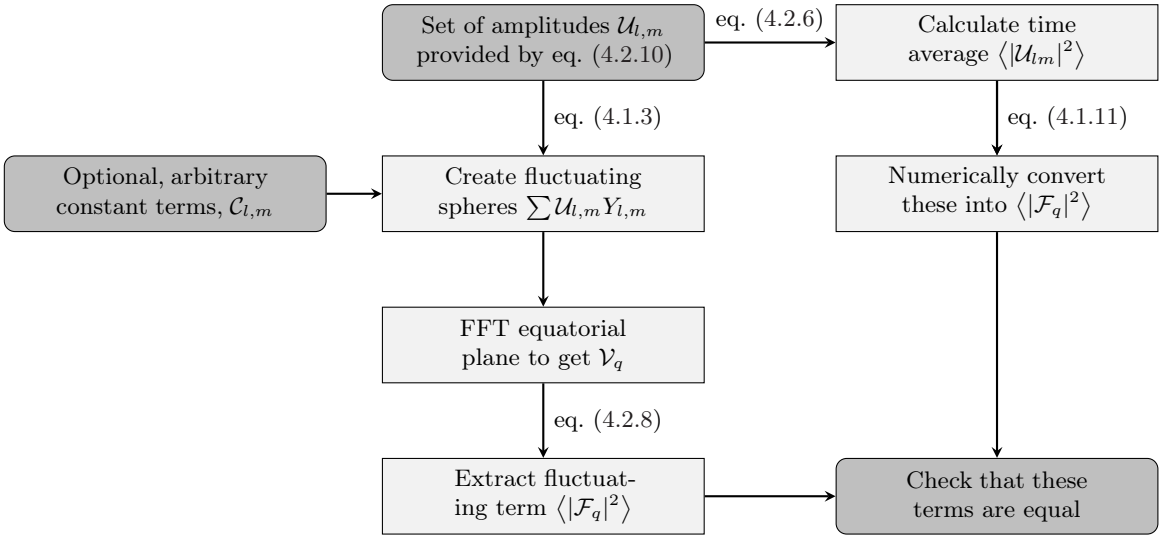

Figure 4.2.6: Flowchart to test that we are able to analyse the fluctation spectrum of a quasi-spherical droplet.

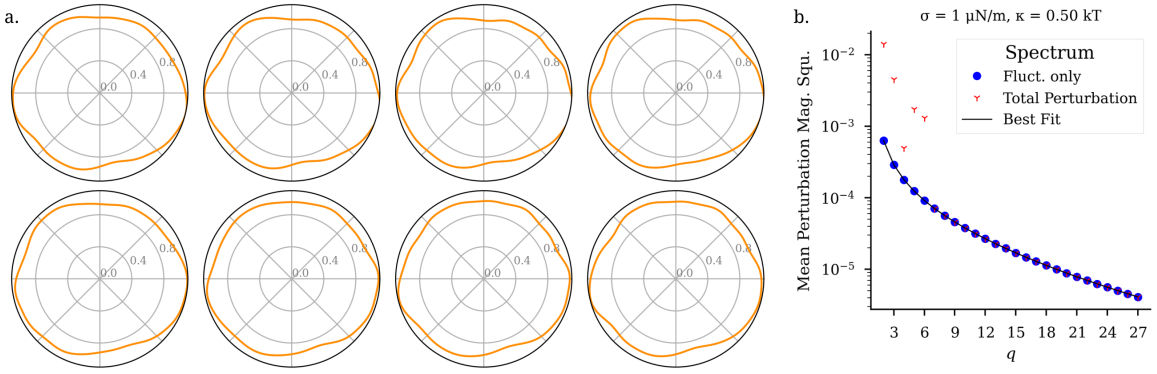

Figure 4.2.7: Recovery of physical values from the full 3d spectrum. This approach allows us to remove the constant contributions to the perturbation spectrum and accurately recover the values of σ and κ.

4.2.2 Rotation of rigid bodies

Although we are confident in the implementation of our model, we wish to be sure that the experimental data that we gather is meaningful, and is genuinely due to the thermal fluctuations of the droplet surface. A possible cause of the deceptive movement of a droplet boundary in our images could be due to a rough body that rotates rather than fluctuating.

We can extend the simulations above to investigate this scenario and what effect this has on the observed perturbation spectrum. Instead of individual perturbation modes fluctuating with time, we now allow for the entire object to rotate uniformly. Investigating these scenarios requires a detour into the mathematics behind rotations.

4.2.2.1 Methods of Rotations

For the rotations in the following section we use quaternions to rotate the rigid body. These have several useful properties and they are given in the form of

$$q = a + bi + cj + dk, \tag{4.2.11}$$

where a, b, c, d are real numbers and i, j, k are the quaternion units following the rules,

$$i^2 = j^2 = k^2 = ijk = -1\ . \tag{4.2.12}$$

It is common to represent the imaginary components as a vector, $\vec{\mathbf{r}}$, with a scalar component for the real part, namely, $q = a + bi + cj + dk = a + \vec{\mathbf{r}}$.

We introduce these because the rotation of a vector, $\vec{\mathbf{v}}$, about the axis $\vec{\mathbf{r}}$ for an angle α can easily be given in terms of quaternions as[2, 3]

$$\vec{\mathbf{v}}' = q\vec{\mathbf{v}}q^{-1}, \tag{4.2.13}$$

2. The product of two quaternions is *distributive*: every element of the first quaternion is multiplied by every element in the second; hence giving another quaternion. When considering quaternion-vector multiplication the same rule applies, with the 3-vector treated as a quaternion with no scalar component.

3. This relation only holds when $|q| = 1$, which is required for rotations. Otherwise, there is an additional factor related to the normalisation of the quaternion.

where the quaternion, q, and its conjugate, q^{-1} are given by,

$$q = \cos\frac{a}{2} + \vec{\mathbf{r}}\sin\frac{a}{2} \equiv \cos\frac{a}{2} + \begin{pmatrix} b \\ c \\ d \end{pmatrix}\sin\frac{a}{2} \tag{4.2.14a}$$

$$q^{-1} = \cos\frac{a}{2} - \vec{\mathbf{r}}\sin\frac{a}{2} \equiv \cos\frac{a}{2} - \begin{pmatrix} b \\ c \\ d \end{pmatrix}\sin\frac{a}{2}\ . \tag{4.2.14b}$$

We find that we can compose two rotations by quaternion multiplications, $q' = q_1 q_2$.

Uniformly distributed rotations

Quarterions are very convenient, as provided that we can uniformly generate rotation axes in the unit sphere, the rotations about these axes will also be uniformly distributed.

In a similar manner to section 3.4.1, care has to be taken for generating uniform rotation. To illustrate this point, consider the area element of a sphere given by

$$\mathrm{d}A = \sin\theta\,\mathrm{d}\theta\,\mathrm{d}\varphi\ . \tag{4.2.15}$$

If we generate the points uniformly in φ and θ, we find that the points are more densely packed around the poles [128]. Instead, we have to generate the points uniformly across $u = \cos\theta$[4] and φ. Translating u and φ into Cartesian coordinates,

$$x = \sqrt{1-u^2}\cos\varphi\ , \tag{4.2.16a}$$

$$y = \sqrt{1-u^2}\sin\varphi\ , \tag{4.2.16b}$$

$$z = u\ , \tag{4.2.16c}$$

where $u \in [-1, 1]$ and $\varphi \in [0, 2\pi)$.

We can then use these points to create a vector $\vec{\mathbf{r}}$ and by choosing a rotation angle $\alpha \in (0, 2\pi)$, we create a random quaternion rotation that is evenly distributed across the sphere.

4.2.2.2 Creating the rough body

We now investigate how we may model the rigid body themselves. In a similar model to the description of the granules, we assume that surface roughness of the rigid body can be described using spherical harmonics with a spectrum $\mathcal{U}_{lm}$.

4. For which $\mathrm{d}u = \sin\theta\,\mathrm{d}\theta$ accounting for this term in eq. 4.2.15

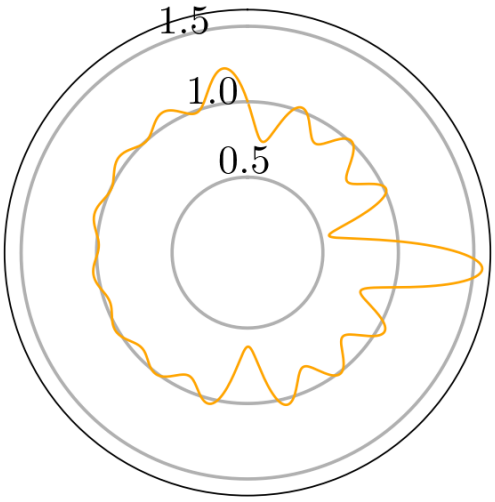

Figure 4.2.8: When the spherical harmonic terms are added with no additional phase, this often leads to shapes with large peaks, as the deformation is concentrated at the poles.

The simplest approach to create a perturbation on the surface, $u(\varphi, \theta)$, as a sum of these terms,

$$u(\theta, \varphi) = \sum_{l=2}^{l_{\max}} \sum_{m=-l}^{l} \mathcal{U}_{lm} Y_{lm}(\theta, \varphi) \ , \tag{4.2.17}$$

from which we may give the surface as $R(\varphi, \theta) = R_0[1 + u(\varphi, \theta)]$. However, we find that this creates strong deformations around $\varphi = 0$ where the maximum of the each of the spherical harmonics terms stack as shown in fig. 4.2.8.

Therefore, we introduce a random phase into these terms,

$$u(\theta, \varphi) = \sum_{l=2}^{l_{\max}} \sum_{m=-l}^{l} \mathcal{U}_{l,m} Y_{l,m}(\theta, \varphi') \ , \tag{4.2.18}$$

where $\mathcal{U}_{l,m} = |\mathcal{U}_{l,m}| e^{i\varphi'} e^{i\theta'}$. This is done by creating a vector $\vec{\mathbf{x}}$ representing the point given by (θ, φ) on the unit sphere and then rotating this vector by a random quaternion $q^0_{l,m}$ (as described in section 4.2.2.1). The results employing eq. (4.2.18) are shown in fig. 4.2.9, showing the more even distribution of the perturbations.

4.2.2.3 Results

Smooth rotations

The first case that we investigate is if the uniform rotation of a rigid body resembles the thermal fluctuations of a stress granule. From sec. 4.2.2.2 each perturbation mode is created with a random rotation given by a quaternion $q^0_{l,m}$. We then uniformly rotate the entire body

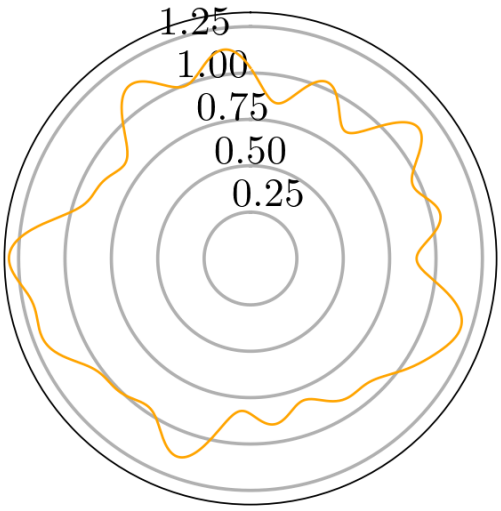

Figure 4.2.9: Rotation of the perturbation terms leads to more even distribution of perturbation leading to a more physically likely shape.

using a given quaternion q_r, giving the final rotation as $q^1_{l,m} = q^0_{l,m} q_r$.

In order to calculate the intermediate rotations between these points, we use Slerp (Spherical linear interpolation)[143]. To start, we calculate the angle subtended by the rotation, Ω, which is given by the dot product of the quaternions corresponding to the start and end points: $\Omega = q^0 \cdot q^1$. Then the interpolation is given by

$$\mathcal{S}(q_0, q_1, t) = \frac{\sin([1-t]\Omega)}{\sin\Omega} q_0 + \frac{\sin(t\Omega)}{\sin\Omega} q_1 \ , \tag{4.2.19}$$

where $0 \geq t \geq 1$ is the interpolation parameter between the start and end points. Values of $t > 1$ continue this rotation. This method is used as it guarantees that the rotation proceeds at a uniform rate with t. In the special case where $\Omega = \pi/2$, we can simplify[5] the above expression, by introducing $\theta \equiv t\pi/2$ to give the following

$$\mathcal{S}(q_0, q_1, \theta) = q_1 \cos\theta + q_1 \sin\theta \ . \tag{4.2.20}$$

To verify the correct working of this approach, we show in fig. 4.2.10 the simple case of a rotation about an axis out of the plane. This can be seen as a confocal slice of a granule rotating while keeping the same region visible, just changing the orientation. These rotations will change only the phase of the Fourier terms and not the magnitude. In a more general case, the granule may rotate about another axis, meaning that the slice seems to fluctuate as material rotates in and out of the visible plane. This is shown in fig. 4.2.11.

5. Making use of the fact that $\sin(\pi/2 - t\pi/2) = \cos(t\pi/2)$.

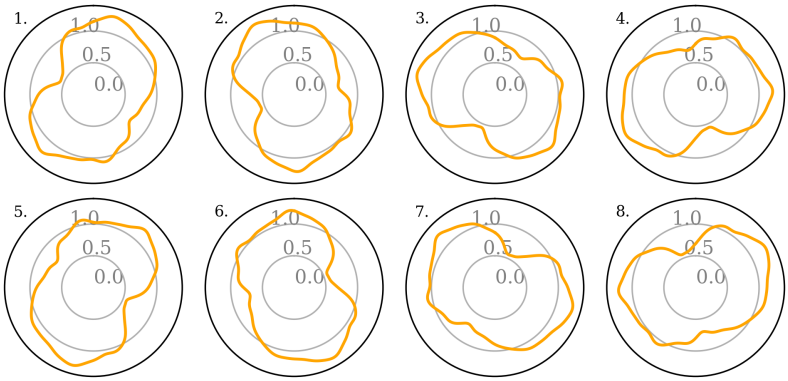

Figure 4.2.10: We verify the correct modelling of a rotation of a rigid body in the simple case of a counter-clockwise rotation in the visible plane. Time advances with the indices (1-8).

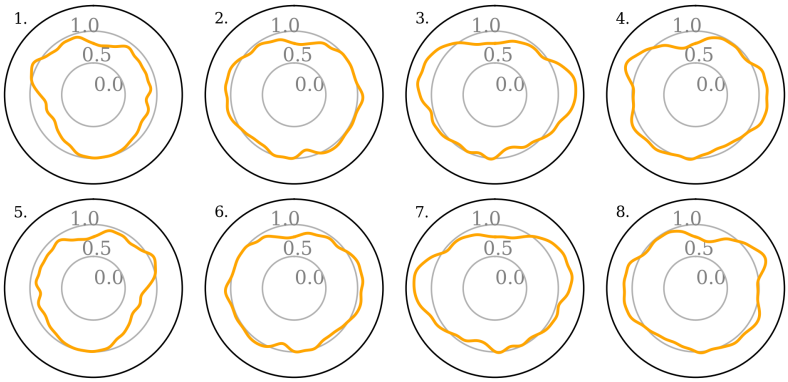

Figure 4.2.11: A body with the same power spectrum as fig. 4.2.10 is rotated 2π radians about the y-axis, which leads to apparent fluctuations in the visible z=0 plane.

We create a rough body with a given power spectrum $\mathcal{U}_{l,m}$ and then rotate this 2π radians around $\vec{\mathbf{r}} = (0, 1, 0)$ and record 100 images from the $z = 0$ plane evenly spaced throughout the rotation. From these disks we perform a Fourier transform and then the fitting as per our usual methods. We use a pink noise power spectrum, $\mathcal{U}_{l,m} \propto l^{-1}$, as this noise spectrum is often found in biological systems [144, 145]. We see in fig. 4.2.12 that the rotation of the rigid body quantitatively resembles the thermal fluctuations of the droplet surface, but the measured spectrum is clearly distinct and cannot be fit to the theoretical spectrum for a fluctuating droplet.

Modeling rotational Brownian motion

A better model for the rotations of a rigid body in our system is a series of small rotations about a random axis, similar to thermal Brownian motion of a diffusing particle. Therefore,

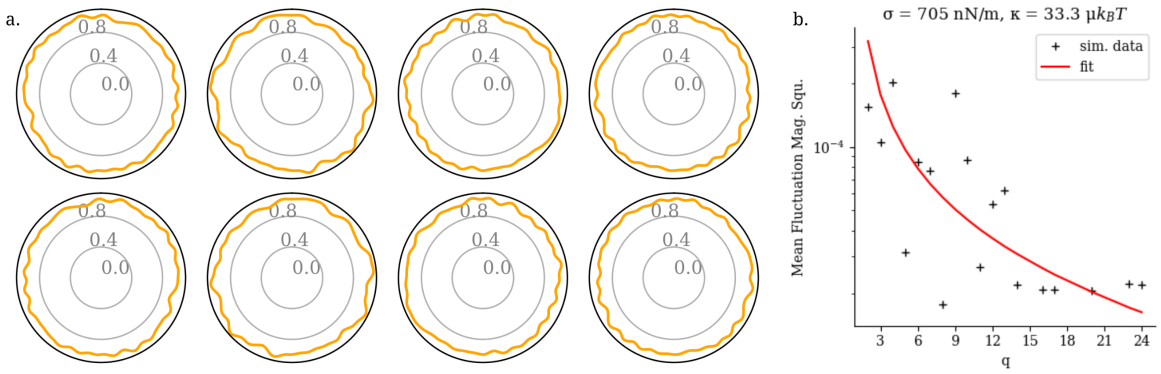

Figure 4.2.12: (a) Apparent fluctuations of a granule-like rigid body due to rotation. **(b)** However, the measured fluctation spectrum does not fit well to that of a fluctuating LLPS droplet.

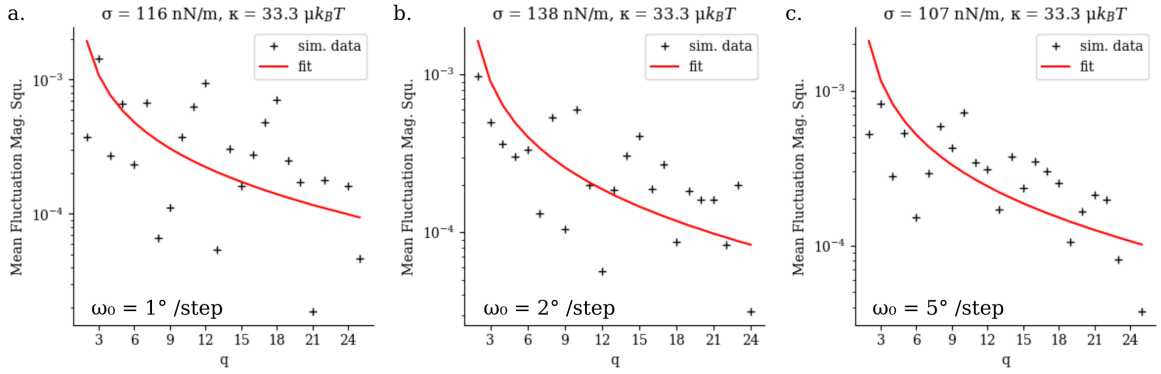

Figure 4.2.13: Apparent fluctuation spectrum of a rough body due to random rotation as given in eq. (4.2.21). The resulting spectra are still distinguishable from thermal fluctuations.

we describe the rotation at each time step as

$$q_{l,m}^{i+1} = q_{l,m}^{i} q_r^i \ , \tag{4.2.21}$$

where the rotation quaternion, q_r^i, is randomly generated at each time point, with rotation angle, ω, chosen from a normal distribution with standard deviation ω_0 and rotating about a random axis.

We create a rough body as above and simulate 100 rotation steps over several repeats varying rotation angle ω_0. The results of which are shown in fig. 4.2.13 when the rough body is initialised with a pink noise spectrum. The resultant apparent spectrum is noisier the standard deviation ω_0 is. However, in all cases we can still distinguish them from the expected spectrum if the droplet surface fluctuates. In fig. 4.2.14 we demonstrate that that the poor fitting to the theoretical spectrum is also present in a body created with white noise spectrum that has no dependence on l.

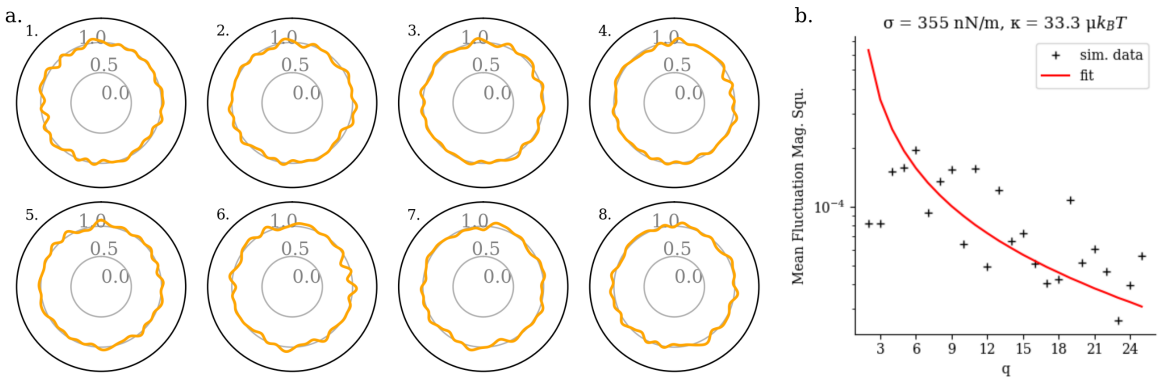

Figure 4.2.14: Apparent fluctuation of a rough bodies with a white noise shape spectrum, due to random rotation as given in eq. (4.2.21). The power spectrum is still distinct from thermal fluctations.

4.2.3 Fixed cells

The second experimental concern raised in this section is that the apparent fluctuating surface is due to microscopy noise rather than thermal fluctuations.

Paraformaldehyde (PFA) can be used to fix the cells by cross-linking proteins[6], which freezes the granules mid fluctuation. This gives a nearly identical model system to contrast to living cells, but where any perturbations will be solely due to microscopy noise. Here we present two means by which we can distinguish the microscopy noise in fixed cells from the boundary fluctuations in live cells.

4.2.3.1 Each point in the spectrum of fixed granules is randomly offset

While a granule within a fixed cell will retain its granule-like shape, we expect its *time averaged* (squared) spectrum, $\langle|\mathcal{V}_q|^2\rangle$, to be distinguishable from a fluctuating granule.

We expect that, in a live cell, each of perturbation modes will fluctuate with the form

$$\mathcal{V}_q(t) = \mathcal{V}_{q,0}\sin(\omega_q t)\ , \tag{4.2.22}$$

where $\mathcal{V}_{q,0}$ is the amplitude of the fluctuation and ω_q is the (temporal) frequency of the fluctuation.

As already covered in sec. 4.2.1.2, during the live cell analysis we image for a time, T, which we assume to be much longer than the fluctuation period. We can then calculate the time

6. Methods section 2.1.2.1

Figure 4.2.15: Comparison of the fluctuation spectrum for live **(a)** and fixed cells **(b)**. For the fixed cells all of the points are offset by a random factor, allowing them to be clearly distinguished from a granule in a live cell.

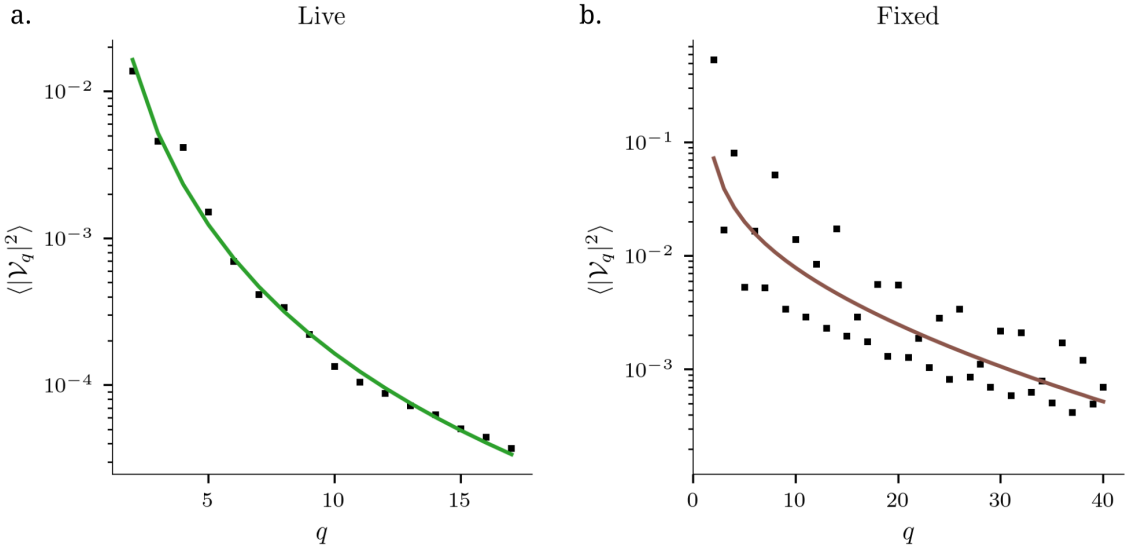

average as

$$\langle|\mathcal{V}_q|^2\rangle = \frac{1}{T}\int_0^T \mathcal{V}_q^2 \,\mathrm{d}t \tag{4.2.23a}$$

$$\langle|\mathcal{V}_q|^2\rangle = \mathcal{V}_{q,0}^2 \frac{1}{T}\int_0^T \sin^2 \omega_q t \,\mathrm{d}t \tag{4.2.23b}$$

$$\langle|\mathcal{V}_q|^2\rangle = \frac{1}{2}\mathcal{V}_{q,0}^2 \ . \tag{4.2.23c}$$

However, for the fixed cell case, we instead image cells that are frozen at a given time, τ, in the fluctuations, leading to

$$\langle|\mathcal{V}_q|^2\rangle_{\text{fixed}} = \frac{1}{T}\int \mathcal{V}_{q,0}^2 \sin^2(\omega_q \tau) \,\mathrm{d}t \tag{4.2.24a}$$

$$\langle|\mathcal{V}_q|^2\rangle_{\text{fixed}} = \mathcal{V}_{q,0}^2 \sin^2(\omega_q \tau) \ . \tag{4.2.24b}$$

We see that the measured mean squared amplitude for the fixed cells can be similar to the live cell case, eq. (4.2.23c). However, each term is offset by a random phase factor in the $\sin^2(\omega_q \tau)$ term. Therefore, we might expect the fit to the theoretical spectrum to be much poorer because there is a great deal of noise in each point as they are shifted by this phase factor. This can be shown in fig. 4.2.15.b where we compare the fit of a granules in a live cell to one within a fixed cell.

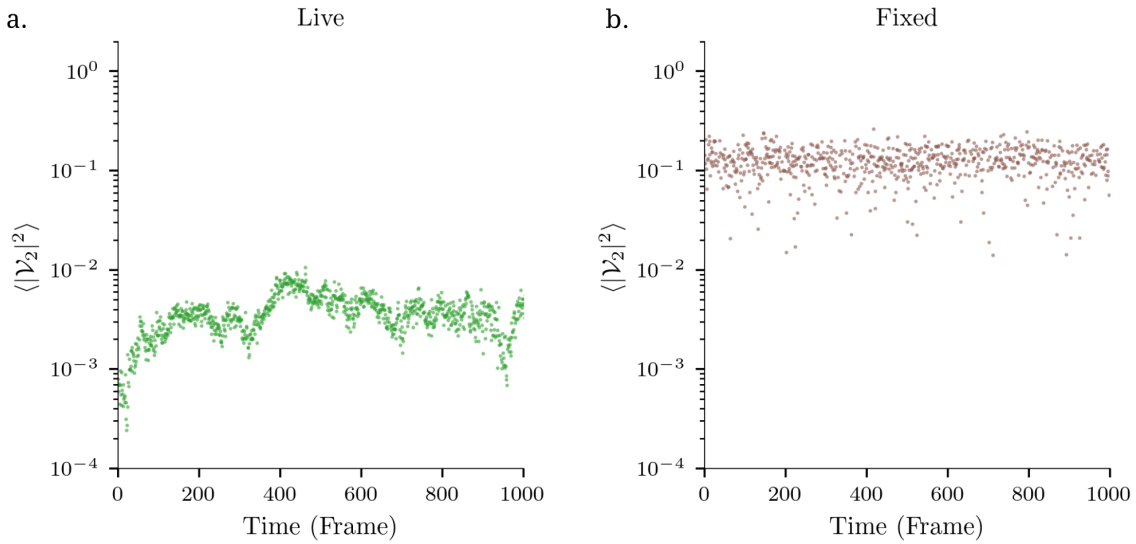

Figure 4.2.16: (a) In a living cell the magnitude of the second order term varies smoothly with time as would be expeceted for a rippling surface. This can clearly be distinguished from **(b)** a fixed cell where there is only a noise component that has no structure with time.

4.2.3.2 The temporal fluctuations can be distinguished in live and fixed cells

We may also distinguish fluctuations in live granules to noise in the fixed cells by studying the behaviour of the mode amplitudes with time. While the exact nature of the fluctuations in the live cell is highly complex, there will be structure in the amplitudes, increasing and decreasing smoothly with time as the surface ripples. In contrast, imaging noise will naturally be uncorrelated with time.

Examples of the magnitude of the second mode with time can be seen in fig. 4.2.16 for live and fixed cells respectively. We see that the results for live cells show a clear structure with time, whereas for the fixed cells, they are entirely random and do not reflect the motion of a physical surface. This further allows us to distinguish our measurements from background noise.

4.3 Image Analysis

Now that we can be confident that the perturbations we observe are thermal fluctuation of the stress granules, we discuss how we measure the fluctuation magnitudes from the microscope images, and how these are converted into our calculated values of surface tension and bending rigidity. Details on how the images are collected are covered in the methods section 2.1.3.

4.3.1 Edge Detection

A critical step in our analysis is drawing the boundary around detected stress granules. There are several ways in which this may be achieved, and so we wish to compare possible approaches. We do this by simulating a fluctuating droplet, degrading the images to model typical microscope effects, and comparing the measured surface tension and bending rigidity values.

While some approaches define the boundary as a selection of pixels, this is unsuitable for our analysis for reasons outlined in the methods section. Instead, we need a method that returns the radius of the interface from the granule centre as a function of angle. We must also consider the limitations of microscopy imaging: images will have noise applied, and high-resolution features will be blurred.

Our first approach is to draw the boundary as the point at which the image intensity goes below a threshold, for instance, 70% of the maximum intensity of the granule. However, the choice of the threshold value is entirely arbitrary and changing it causes a change in the recovered values. This would have left our results fragile and somewhat arbitrary.

Therefore, given an image of a granule, I, we draw the boundary of the granule using the directional gradient, g. This is calculated as the dot product between the gradient of the image $\boldsymbol{\nabla} I$ and radial unit vector from the centre of the granule $\hat{\mathbf{r}}$, namely: $g = \boldsymbol{\nabla} I \cdot \hat{\mathbf{r}}$. This approach requires us to accurately calculate the gradient of the image and then the maximum of this function.

The directional gradient is a two-step operation. The first is calculating the gradient numerically $\boldsymbol{\nabla} I$. For each pixel in the image this gives a vector that points in the direction of most rapid intensity change. The magnitude of the gradient corresponds to the rate of change of the intensity, and so we would expect this to be highest at the granule boundary. The second step is the dot-product $\boldsymbol{\nabla} I \cdot \hat{\mathbf{r}}$. this refines the boundary by only taking the component of the boundary that is along the direction to the centre of the granule. In the following section we discuss and compare various numerical methods for estimating $\boldsymbol{\nabla} I$, with an emphasis on maximising accuracy and resistance to noise.

4.3.1.1 Calculating the gradient

For now, we consider the one dimensional case, where the definition of a derivative, $f'(x) = \mathrm{d}f/\mathrm{d}x$, is

$$\frac{\mathrm{d}f}{\mathrm{d}x} = \lim_{\mathrm{d}x \to 0} \frac{f(x + \mathrm{d}x) - f(x)}{\mathrm{d}x} \ . \tag{4.3.1}$$

However, in a image we cannot make $\mathrm{d}x$ arbitrarily small, instead it is the size of a pixel, h, and so we must use a discrete forward difference method,

$$\frac{\mathrm{d}f[x]}{\mathrm{d}x} \approx \frac{f[x+1] - f[x]}{h} \ , \tag{4.3.2}$$

where $f[x]$ is the intensity of pixel x in the image[1]. The accuracy of the approximation decreases as h increases.

We show in fig. 4.3.1 that this approximation can be improved by using the central finite difference,

$$\frac{\mathrm{d}f[x]}{\mathrm{d}x} \approx \frac{1}{2} \frac{f[x+1] - f[x-1]}{h} \ . \tag{4.3.3}$$

In the forward-difference method, the error scales as $\mathcal{O}(h)$; namely the error scales linearly with the pixel size. In the central difference method, the same number of points are evaluated but the error scales with $\mathcal{O}(h^2)$, making this a second order method. The improved accuracy of the central difference method is shown in fig. 4.3.1.b.

Each numerical approximation method can be summarised as a *stencil*, k, of $2N+1$ elements.

1. There are several options for what to do when we attempt to sample a pixel outside of the image; however, it is sufficient in our work to take these values to be 0.

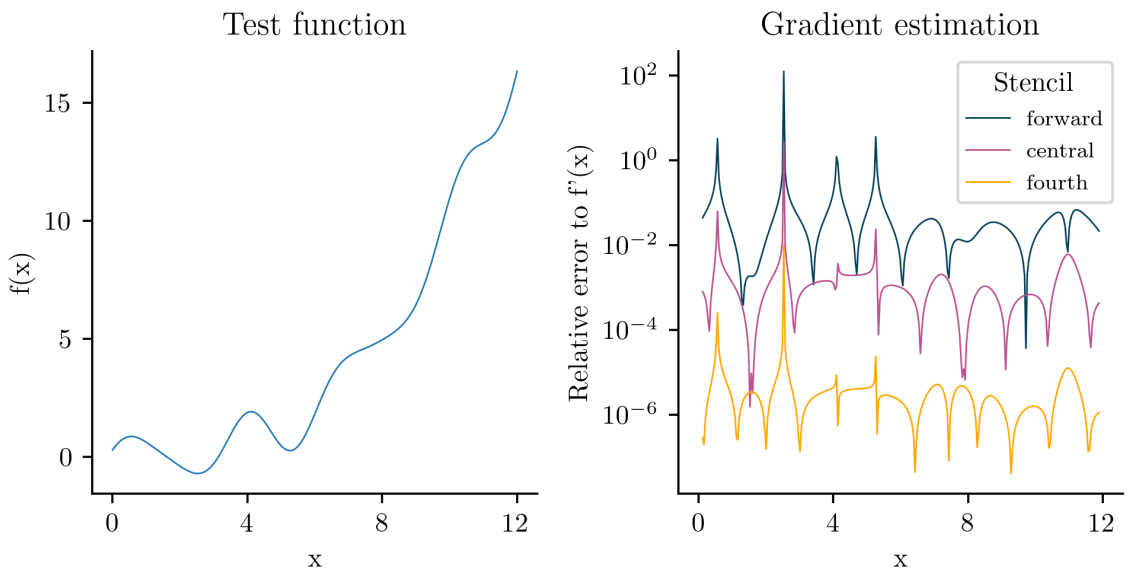

Figure 4.3.1: On the left, we see an arbitrary test function. On the right is the relative error in numerically calculating the gradient of this function. We see that there is approximately a two order of magnitude reduction in error when moving from the first order, forward difference method, eq. (4.3.2), to a second-order central difference method, eq. (4.3.3). For reference, we also include a fourth-order central difference, eq. (4.3.5), which yields another two order magnitude reduction in error.

For instance, the stencil of the forward difference method in eq. (4.3.2) can be given as $k = (\,0\;-1\;1\,)$ and the central finite difference, eq. (4.3.3), is given by $k = \frac{1}{2}(\,-1\;0\;1\,)$. The gradient of the image function, I, in the x direction, G_x, is then calculated as $G_x = k_x * I$, where $*$ is the correlation[2] operator, defined to be

$$G_x[i] = k_x * I = \sum_{n=-N}^{N} k[n] \cdot I[i+n] \;, \tag{4.3.4}$$

for a kernel of size $2N + 1$.

When we consider the two dimensional case, the gradient in the y direction, G_y, can be calculated in a similar manner.

At the cost of additional computational expense, we can evaluate more points and calculate a 4th order approximation,

$$k_{4\text{th}} = \frac{1}{12}\begin{pmatrix} -1 & -8 & 0 & +8 & -1 \end{pmatrix} . \tag{4.3.5}$$

The increased accuracy of the fourth order method, in comparison to the central difference is shown in fig. 4.3.1.

2. This is almost identical to the more well-known convolution operation, but differs by a sign change.

4.3.1.2 Smoothing

The above methods are quite sensitive to noise in the image, so it is common to include an orthogonal component $k_\perp$, that acts as a smoothing component. For instance, the Sobel operator is commonly used in image processing. It is created as a combination of gradient and smoothing operations,

$$k_\parallel = \begin{pmatrix} -1 & 0 & 1 \end{pmatrix} \quad \text{and} \quad k_\perp = \begin{pmatrix} 1 \\ 2 \\ 1 \end{pmatrix} . \tag{4.3.6}$$

These two kernels are convolved in the following order to the image[3],

$$G_x = k_\perp * (k_\parallel * I) . \tag{4.3.7}$$

Similarly, the smoothed gradient in the y direction can be calculated as

$$G_y = k_\perp^\intercal * \left[k_\parallel^\intercal * I \right] = \left(1\ 2\ 1 \right) * \left[\begin{pmatrix} -1 \\ 0 \\ 1 \end{pmatrix} * I \right] . \tag{4.3.8}$$

We then give the gradient of the image, $\boldsymbol{\nabla} I$, as

$$\boldsymbol{\nabla} I = (G_x \hat{\mathbf{x}} + G_y \hat{\mathbf{y}}) I , \tag{4.3.9}$$

from which we can calculate the directional gradient.

We also consider several kernels commonly used in image processing: `scharr` is similar to `sobel`, a 2nd order accurate central difference method that is designed exhibit better rotational in-variance [146, 147]. The `five tap` and `seven tap` methods are higher order accuracy methods that use a larger Gaussian smoothing kernel [148]. For completeness we also include the 3rd order `forward diff` and `backward diff` kernels. The stencils are included in the appendix, sec. 4.7.2.

3. We note that we could convolve the two 1d kernels into a single 2d kernel and then apply this to the image. However, for two kernels with N elements this will require N^2 options rather than $2N$, and so will be much slower. It is worth noting that not all square kernels can be separated into the linear kernels.

4.3.1.3 Calibrating the kernels

There will be some error in our estimation of the gradient terms, G_x and G_y. We will look into the structure of this error and how it will propagate to the directional gradient and then onto the detected boundary. The directional gradient is dependant on both the magnitude of the gradient and its phase. We wish to investigate if the phase of the gradient will be correctly conserved. Once we have calculated the gradient of the image in the x and y directions ($G_x I$ and $G_y I$), these are used to construct the gradient $\boldsymbol{\nabla} I$. However, due the to the smoothing introduced in the Sobel-like methods, the gradient is under-represented in diagonal directions compared to those parallel to an axis [149]. To investigate this response, we create a test image from an analytical function, for which we can calculate the deviates analytically and compare this to the numerical methods. We choose a Gaussian function, $I(x, y) = \exp\left[-(x/\sigma_x)^2 - (y/\sigma_y)^2\right]$. By varying the values of σ_x, σ_y we can change the aspect ratio of the test function to verify the kernels accuracy as a function of the boundary angle.

We compare the phase and magnitude of the approximation against the analytical solutions. We cover this in more detail in the appendix section on the kernels 4.7.2. We provide a short summary of this here, with an example in fig. 4.3.2 showing the accuracy of the `sobel` kernel. We see that there is a distinctly anisotropic response to the magnitude error, with a difference between the error at diagonal or primary directions. The phase difference tends toward the x, y axis, suggesting that these off-diagonal terms are underestimated as we might expect. This is in contrast to the isotropic response of the Scharr or seven tap kernel. Although there is a significant anisotropy in the fourth-order central difference method, the error magnitude is significantly smaller than any of the other kernels.

4.3.1.4 Simulating granule images

While useful for understanding the kernels, the Gaussian functions used above are a limited model for our stress granule images. We can use a radial function, $R(\varphi, t) = \sum \mathcal{V}_q(t) e^{iq\varphi}$, to generate the frames of the granule images by choosing a spectrum, $\mathcal{V}_q$, to resemble a fluctuating granule.

We start with an array of points, and for each of these points, we calculate the distance from the origin $r = \sqrt{x^2 + y^2}$. An initial approach is to create a binary image, where if the distance to a given point is less than the test function at the same angle, $r < R(\varphi)$, the pixel is set to 1, or 0 otherwise. However, this creates a sharp interface that gives an inadequate

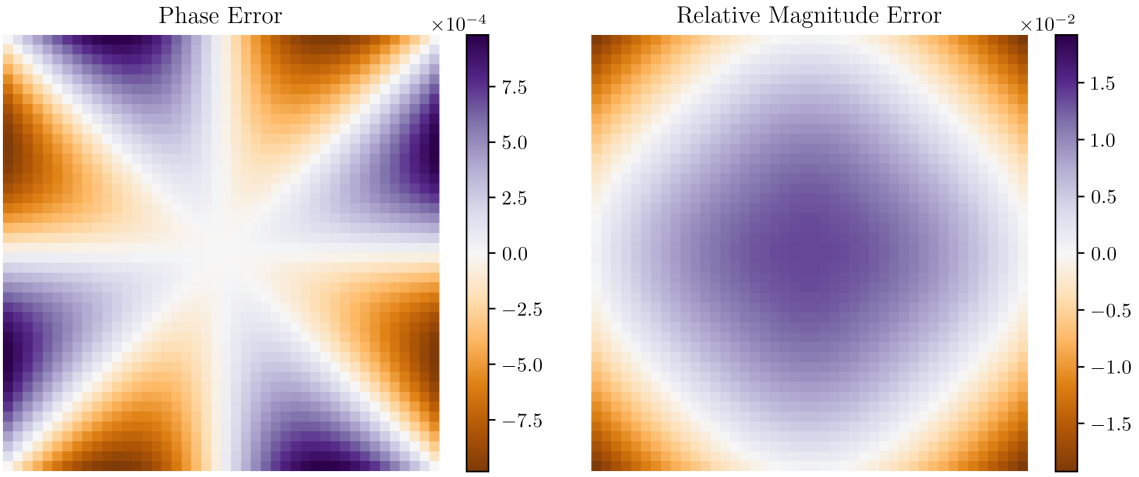

Figure 4.3.2: Gradient estimation of a Gaussian function. In this figure we plot the error in the `sobel` kernel. The phase is correct only at the primary x, y directions and diagonals, which suggests that the phase is underestimated towards the primary axis. There is a significant anisotropy in the magnitude error between the primary and diagonal errors.

description of the microscopy stress granule images that have a blurry interface. So the value of the pixel, i, is instead given as

$$i(r) = \frac{1}{2}\left[1 + \tanh\left(\frac{R - r}{\zeta}\right)\right] , \tag{4.3.10}$$

where ζ is the interface width. This function gives a value of $+1$ in the granule and -1 outside, but now transitions smoothly at the granule boundary.

In figure 4.3.3.a we show a single frame of a simulated granule. Fig. 4.3.3.b gives the cross section of this granule, which we can see is similar to the cross section of an experimentally measured granule in fig. 4.3.4. The directional gradient of this simulated granule is shown in fig. 4.3.3.c and the detected boundary is shown by white points.

These frames are then analysed following the typical pipeline to extract the measured surface tension and bending rigidity. We can complicate the imaging by adding a shot noise component—proportional to the square root of the magnitude at that the point—and varying the interface width to simulate blurring.

To compare the kernels, we simulate fluctuating granule images and calculate the error in recovering the surface tension as a function of both interface width, ξ, and noise magnitude, with 40 granules per group as summarised in fig. 4.3.5.

The fitting to a simulated granule image is demonstrated in fig. 4.3.3.d where we see the best fit between the simulated and theoretical spectrum leads to measured surface tension and

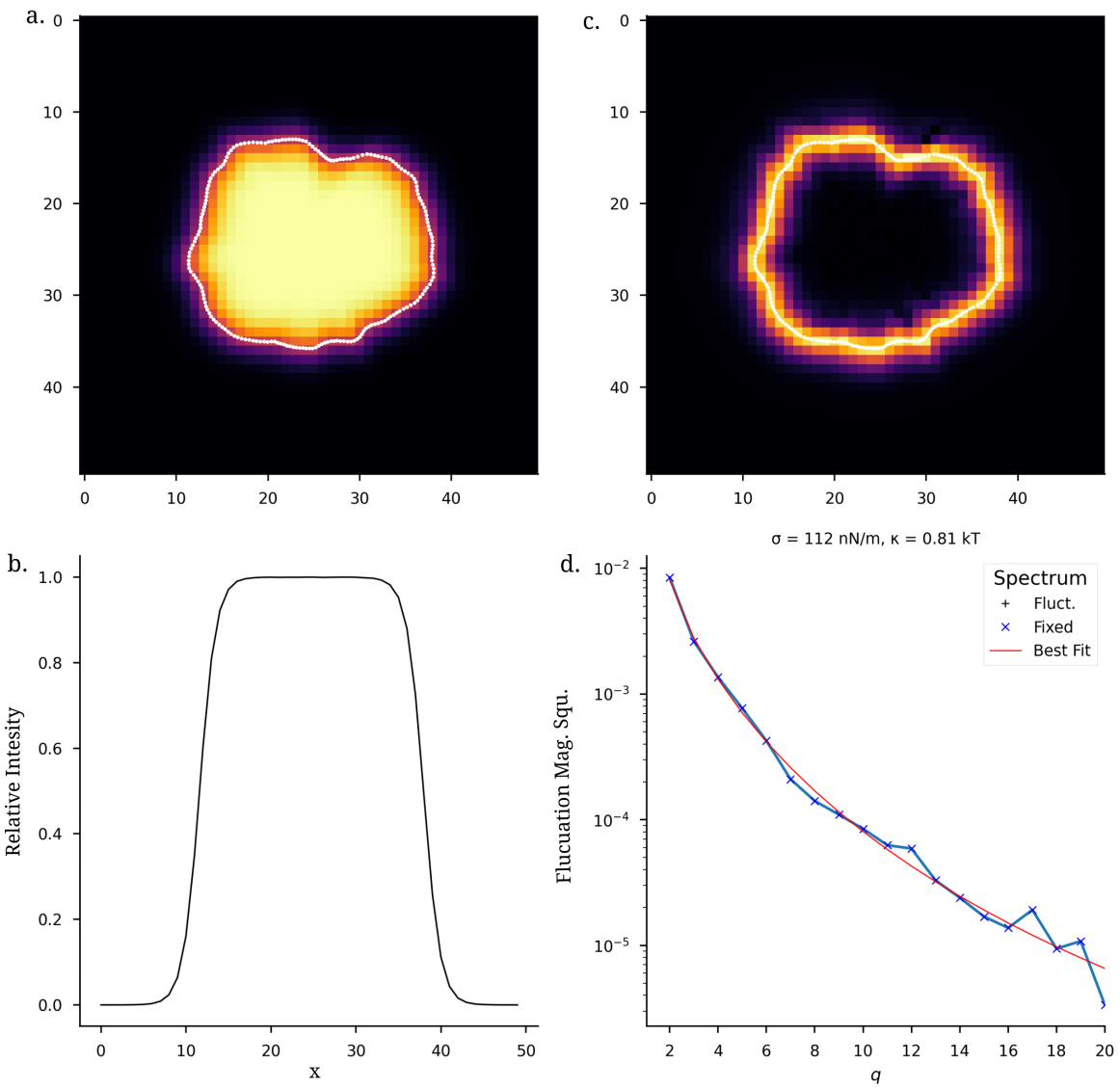

Figure 4.3.3: Edge detection on a simulated granule. **(a)** Simulated image. **(b)** The cross section of the simulated granule resembles the cross section of an experimental image. **(c)** Directional gradient of the image, as calulated by the Sobel kernel. The maximum of the directional gradient is highlighed in white, showing the granule boundary. **(d)** The fit from this boundary gives a good fit to the theoretical spectrum, but surface tension is overestimated slightly.

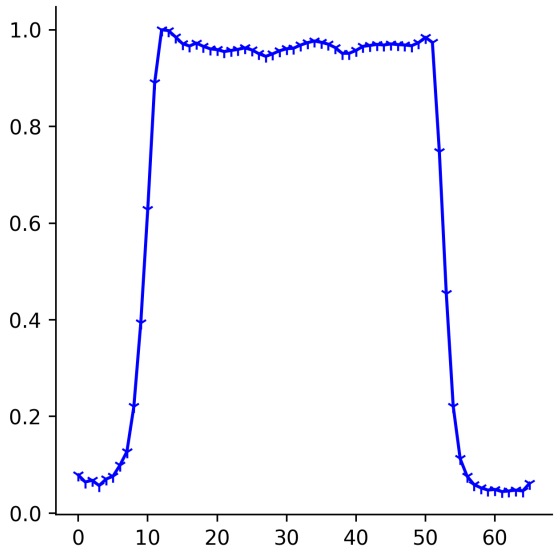

Figure 4.3.4: Cross section of an actual granule taken from ImageJ [150]. We see that is similar in profile to the one used in the simulation.

bending rigidity that are similar to the provided values of 100 nN/m and 1 k_BT respectively.

Firstly, we consider trends that are independent of the kernel. For very narrow interfaces widths, as on the left of fig. 4.3.5, all of the methods have a significant variation in the recovered surface tension. However, this interface width is comparable to the pixel size, from which we are unable to determine the boundary width accurately. As this does not reflect images from a microscope, we ignore this column. None of the kernels can recover the expected surface tension at the other extremes of interface width, corresponding to excessive blurring in the image. Simulated images that closely resemble our collected stress granule images correspond to intermediate values of interface width, such as that shown in fig. 4.3.3 for $\zeta = 0.08$ with a noise magnitude of 0.1.

Outside of these extreme cases, we see that the `five-tap` and `seven-tap`—and less so the `sobel` and `scharr`—kernel consistently underestimate the surface tension. While the `forward-third` and `backwards-third` method have a mean value close to the expected values, there is a large degree of uncertainty. We, therefore, favour the `central-fourth-order` method due to the reliable accuracy in the presence of noise and blurring.

4.3.2 Calculating the best fit values of surface tension and bending rigidity

So far, we have derived the theoretical fluctuation spectrum of a LLPS droplet in eq. (4.1.12) and have demonstrated that we are able to measure the experimental fluctuation spectrum from images of granules. The final step in the analysis is to relate these two spectra and extract

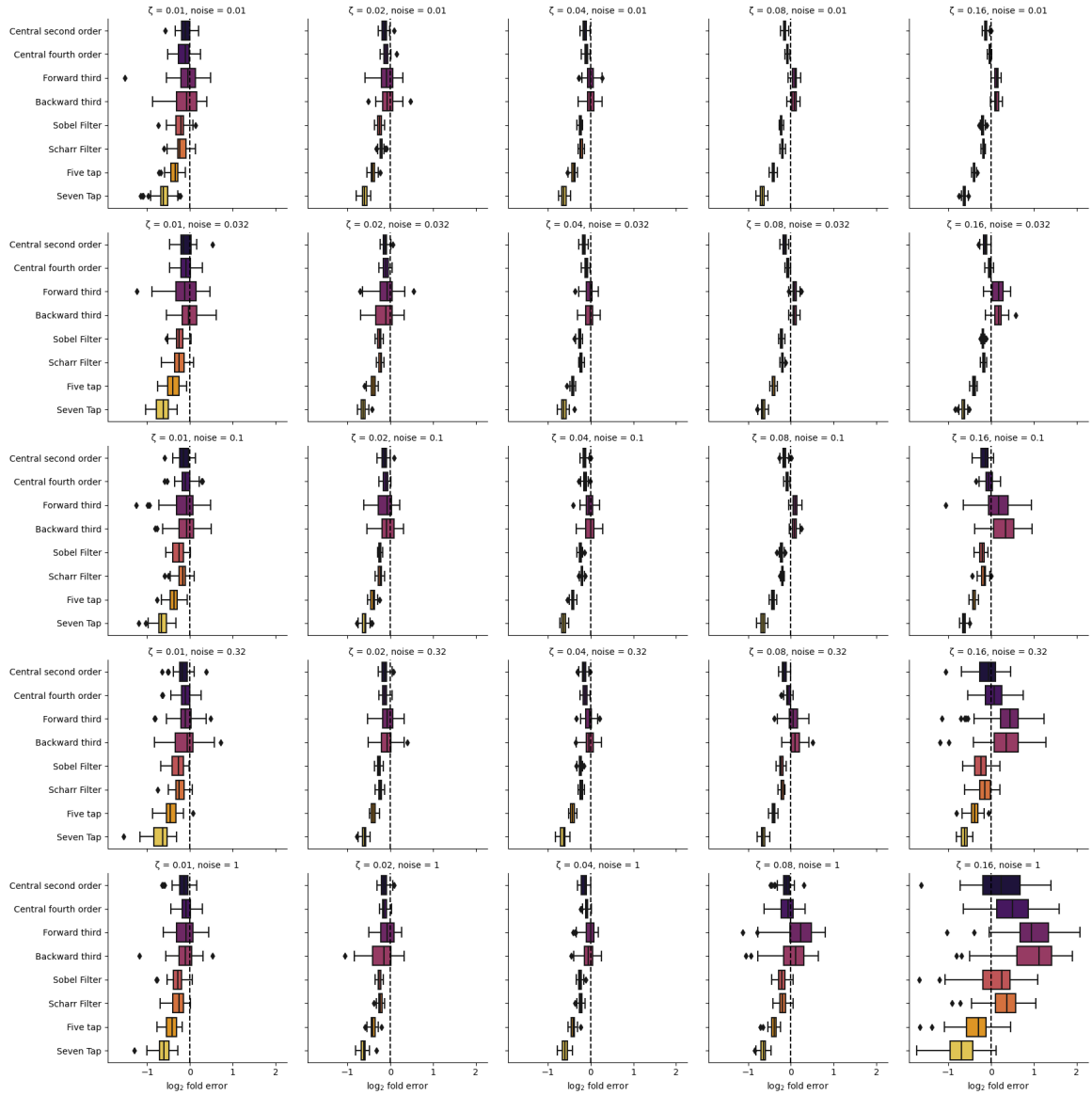

Figure 4.3.5: Relative error on the recovered surface tension for the kernels, as we change the interface width and the noise magnitudes. The far left corresponds to the flat interface case. The methods are quite unreliable here due the discrete nature of the boundary. The granules in the far right correspond to very noisy imaging conditions with a large interface width that are worse than what is seen in our experimental data.

the values of surface tension and bending rigidity.

We define the theoretical spectrum, $\mathcal{S}(\sigma, \kappa; q)$ as the right hand side of eq. (4.1.12),

$$\mathcal{S}(\sigma, \kappa; q) = \frac{k_{\mathrm{B}}T}{\kappa} \sum_{l=q}^{l_{\max}} \frac{P_{lm}^2(0) N_{lm}^2}{(l-1)(l+2)[l(l+1)+\bar{\sigma}]} \ . \tag{4.3.11}$$

During our microscopy experiments we collect a series of 1,000 frames[4] and extract the perturbations of the granules, $\hat{u}$, using the steps in the section above. From this we perform a Fourier transform aggregate with time to give the experimental fluctuation spectrum, $\mathcal{F}_q^2$. By changing the values of σ and κ we attempt to find the best fit between this theoretical spectrum and the experimentally measured fluctuation spectrum for the granule. The resultant best fit values of σ and κ are then our best estimates for the surface tension and bending rigidity of the granule.

4.3.2.1 Fitting the Spectrum

We have to be careful in the choice of how we define a best fit to the experimental spectrum. An error function, $\epsilon(\sigma, \kappa)$, gives a quantitive value for the fit. Here we show that a poor choice of the error function leads to poor fitting to the experimental spectrum.

Our first approach was to define the error as the root-mean-squared distance between the two spectra,

$$\varepsilon_{\mathrm{rms}}^2(\sigma, \kappa) = \sum_q \left(\mathcal{S}(\sigma, \kappa, q) - \mathcal{F}_q\right)^2 \ . \tag{4.3.12}$$

However, as the fluctuation magnitudes, $\mathcal{F}_q^2$, can cover multiple orders of magnitude, this leads the minimiser to prioritise only the significantly larger first orders (low q) and neglect the much smaller later orders. This leads to a very poor overall fit, as is demonstrated in fig. 4.3.6.a using experimental data from a granule that should fit well to the theoretical spectrum.

We can attempt to improve this by introducing a normalisation factor that reduces the importance of the larger first-order terms,

$$\varepsilon_{\mathrm{rms,norm}}^2(\sigma, \kappa) = \sum_q \left(\frac{\mathcal{S}(\sigma, \kappa, q) - \mathcal{F}_q^2}{\mathcal{F}_q}\right)^2 \ . \tag{4.3.13}$$

We see this leads to a much better fitting than the previous method in the first test case, with

4. Section 2.1.3 for details on the microscope and settings.

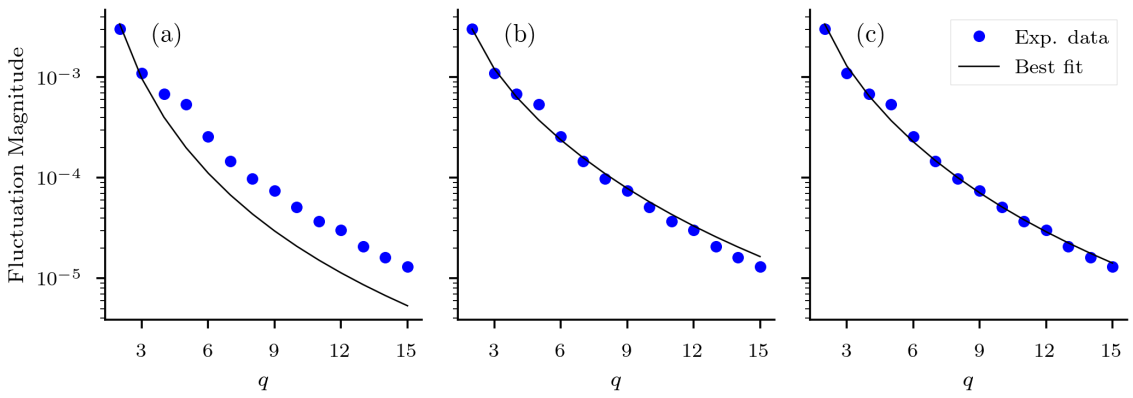

Figure 4.3.6: Examples of the different error measures between the experimental and theoretical spectrum for a typical granule with little noise, that can be fit closely to the experimental data. **(a)** The RMS distance in eq. (4.3.12) in practice puts too much weight in the lower order terms and gives a very poor fitting even in this simple case. In **(b)** and **(c)** we see that both eq. (4.3.13) and eq. (4.3.14) lead to a good fitting between the spectra, although the latter gives a better fit to the higher order terms.

a granule that fits well to the experimental spectrum in fig. 4.3.6.b. However, in fig. 4.3.7.b we demonstrate a more challenging case of noisier experimental data, where the resultant fitting is less convincing.

We also investigated an error measure that is based on the error ratio between the two points,

$$\varepsilon_{\log} = \sum_i \left| \log_{10} \left[\frac{S_i}{\mathcal{F}_i^2} \right] \right| , \tag{4.3.14}$$

which we see in fig. 4.3.6.c gives a similarly good fit to the previous measure in the simple case and improves upon the fitting in the nosier case of fig. 4.3.7.c. We therefore use this as the error function to minimise in the rest of the analysis.

4.3.2.2 Minimisation algorithm

We initially used the L-BFGS-B algorithm [110] to minimise the fitting error, ε. However, we find that there is often a large and relatively flat minimum region, as is shown by the bright region in fig. 4.3.8.a. While the local minimiser will typically reach this region, it may halt due to the very shallow gradient, before reaching the true minimum. In fig. 4.3.8.b we change the colour-map for the data to highlight the region around the global minimum[5] showing the best fit point as the brightest point in the centre of the plot.

We investigated several approaches, including changing the convergence limit for the min-

5. We keep our notation of q being the order, although $n \equiv qR$ is also used elsewhere in the literature.

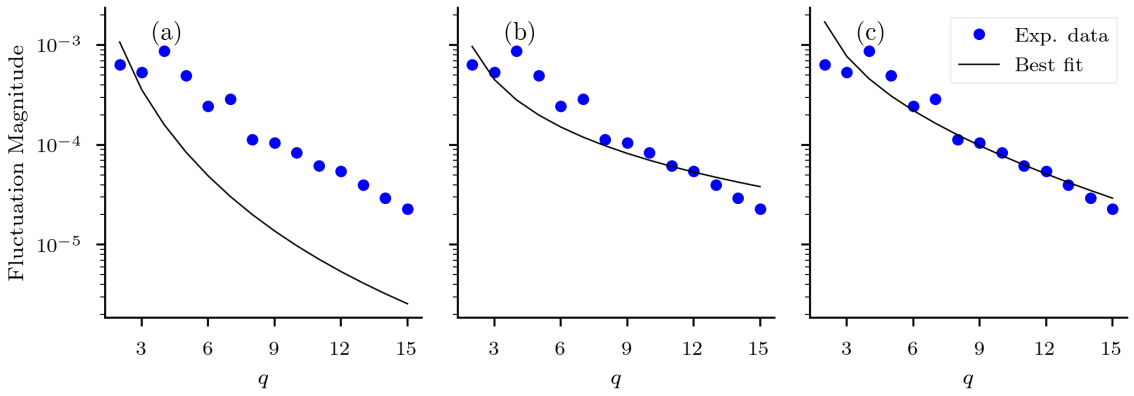

Figure 4.3.7: Examples of error measures between the experimental and theoretical spectrum for a noisy granule spectrum where the correct fitting is more ambiguous. **(a)** The rms fitting, eq. (4.3.12), gives a clearly incorrect fit. **(b)** Introducing a normalisation factor eq. (4.3.13) improves the fitting quality somewhat in this more complicated case. **(c)** The relative error measure eq. (4.3.14) gives a much better fit to the experimental spectrum.

imiser and performing multiple minimisation runs in parallel with varying starting positions. However, we find that the global minimiser approach known as basin hopping [151] was the most reliable.

Basin hopping consists of a loop of three steps after the minimiser has been run from the first time:

1. Perturb the coordinates of the previous minimum randomly to a new position
2. Use this point as the starting point of a local minimisation;
3. Compare this minimum to the minimum in the previous iteration. Based on some criterion we either continue with this new minimum or reject this step and revert back to the previous minimum.

The criterion for accepting or rejecting a step is based on the Metropolis criterion. If the new minimum is lower than the previous step then it is automatically accepted. If not there is a probability that they are accepted of $P = \exp(-(\varepsilon - \varepsilon_{\text{prev}})/T)$ where T is a "temperature" that should be similar to the differences in the minima. It is this step that allows the basin hopping algorithm to locate the true minimum, while the local minimisers stop in a false minimum.

4.3.2.3 Granule filtering

Once we have attempted to draw the boundary, we reject any boundary where there is a large discontinuous jump between two adjacent points. The discontinuities are due to two main

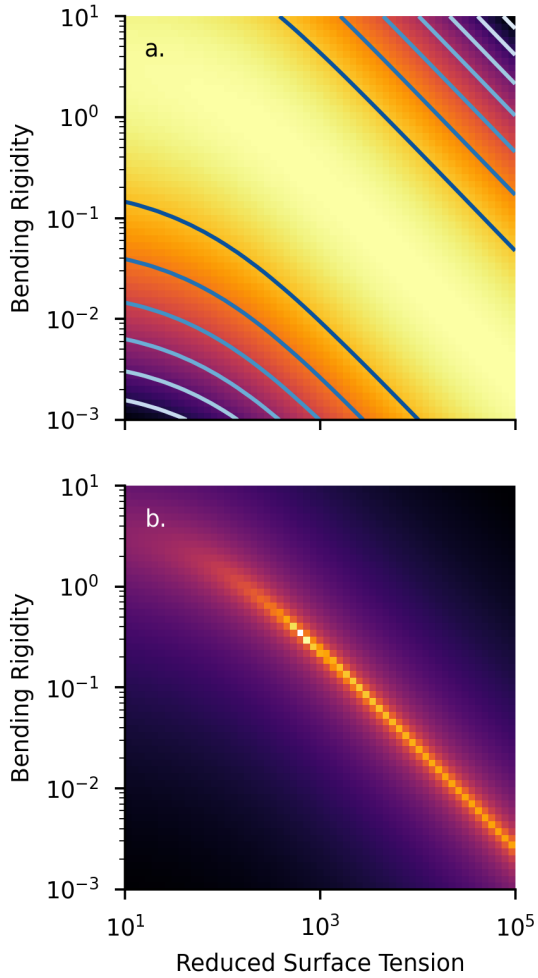

Figure 4.3.8: **(a)** Example of a heat map with a large flat minimum in the centre. **(b)** The same heatmap rescaled to highlight the structure of the minimum region. A traditional minimiser will normally stop randomly within this region, and so we require the basin hopping algorithm to locate the global minimum.

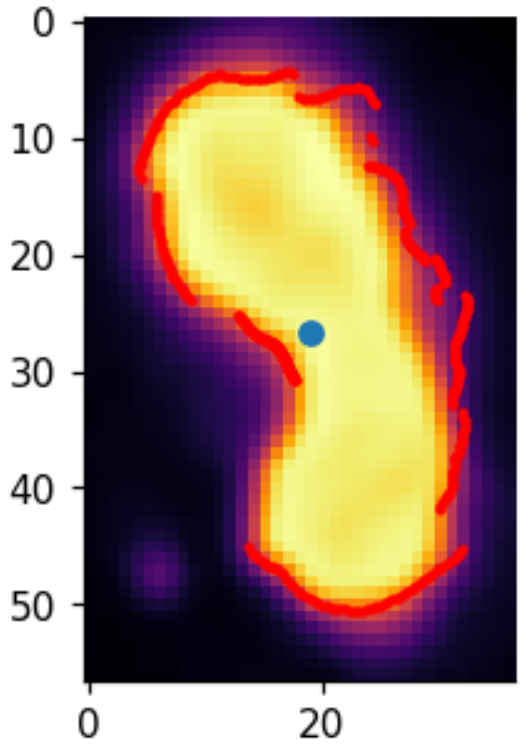

Figure 4.3.9: Example of granules unsuitable for analysis due to being mid-coalencence. The attempted boundary drawing is shown in red and the centre of the granule as a blue dot.

factors. The first is the case when the granule cannot be represented by radial function. This is the case when there are large overhangs in the granule and may be due to granule merging events, an example of which is given fig. 4.3.9. These granules break many assumptions of the derivation of the fluctuation spectrum in eq. (4.1.12).

Secondly, there may be errors in our boundary drawing, likely caused by noise in the system, but these errors are less important as these effects are reduced by time averaging across the frames.

These rejections are evaluated on a frame-by-frame basis, giving a boundary pass rate for each granule. We remove a granule from further analysis if the boundary is rejected in more than 50% of the frames. In this case, it likely that the rejections are due to an invalid granule shape–eg merging–rather than noise.

4.4 Granule Explorer

Here we present granule explorer, a software package developed to gather quantitative data on stress granules and other LLPS systems.

4.4.1 Features of the package

Granule explorer is designed both to gather data from experimental microscopy images and to interact with and explore this data. While the primary purpose of the package is to measure surface tension and bending rigidity from time series images, it can also be used to locate and quantify fluorescent LLPS droplets in still images. The package allows for comparisons between results from different different experiment conditions, making it easy to infer relevant trends and insights from the collected data.

The package provides three main analysis outputs:

Measurement of surface tension and bending rigidity Our goal with the package is to make the analysis and, in particular, the flicker spectroscopy method available to groups studying other LLPS systems, without requiring an extensive mathematical or technical background. The results, and the rest of the analysis pipeline, need to be easily shareable, understandable and reproducible by the rest of the community.

Granule location and tracking A subset of the analysis for the flicker spectroscopy is locating granules and tracking them across frames. We provide a separate pipeline to allow for automated detection and tracking of LLPS droplets in general microscopy images.

Shape analysis of granules We also provide quantitative tools to analyse the granules detected within the image, which for instance, may be used to calculate the size distribution of the granules or the eccentricity of their shape. These results can either be exported for external analysis by the user, or may be analysed using the software's data exploration and filtering tools.

4.4.1.1 Running the analysis

The package has been made available on the python package manager, `pip`, https://pip.pypa.io, and can in most cases be installed by a single command: `pip install granule-explorer` [1]. Alternatively, the `anaconda` package manager can be used to handle the installation of external dependencies, `conda install -c bioconda granule-explorer`. This latter option is recommended on servers. We will demonstrate basic functionality in this section, but a full guide and documentation is available at `granule-explorer.readthedocs.org`, including the equivalent command line tools and a guide for gathering data suitable for the fluctuation analysis.

Upon starting granule explorer, a web page will display summaries of the experiments available for analysis, with an example shown in fig. 4.4.1. From this screen, a user may add more experiments by providing microscope files and experimental information, such as the cell line imaged, that can later be used to interact with the data. Currently, we support the image formats from Ziess (`.czi`) and Andor (`.ims`) microscopes and the open format `.ome.tiff` .

Once an experiment is created, granule explorer automatically tracks the analysis progress. When output files are not found, such as for the FXR1 experiment shown in fig. 4.4.2, a link is provided that will automatically start the analysis processes. Once this is completed, clicking on a card will give a detailed break down on the experiment.

This shows data at the level of individual granules, including the measured surface tension and bending rigidity. Each step of the analysis produces diagnostic figures that allow visual verification of the methods and parameters used for individual granules. In particular, this includes the quality of the granule boundaries drawn and the quality of the fitting to the spectrum as illustrated in fig. 4.4.2. Granule data may be exported from this screen in human readable `.csv` format for external analysis. The page also allows editing of the experimental metadata and inspection of the configuration files used.

A key part of granule explorer is the metadata attached to each experiment. This may take the form of categorical data, such the cell line or treatment used, or may be free-from, such as the user provided descriptions of the cell line. The categorical data may be used to organise and link experiments, as can be seen in fig. 4.4.3.

1. These hyperlinks are non-functional for now, as the code repositories are private while the thesis is under review, please contact the author for access.

Figure 4.4.1: Screenshot showing the experiment list, with a short summary for each experiment showing the progress of the workflow.

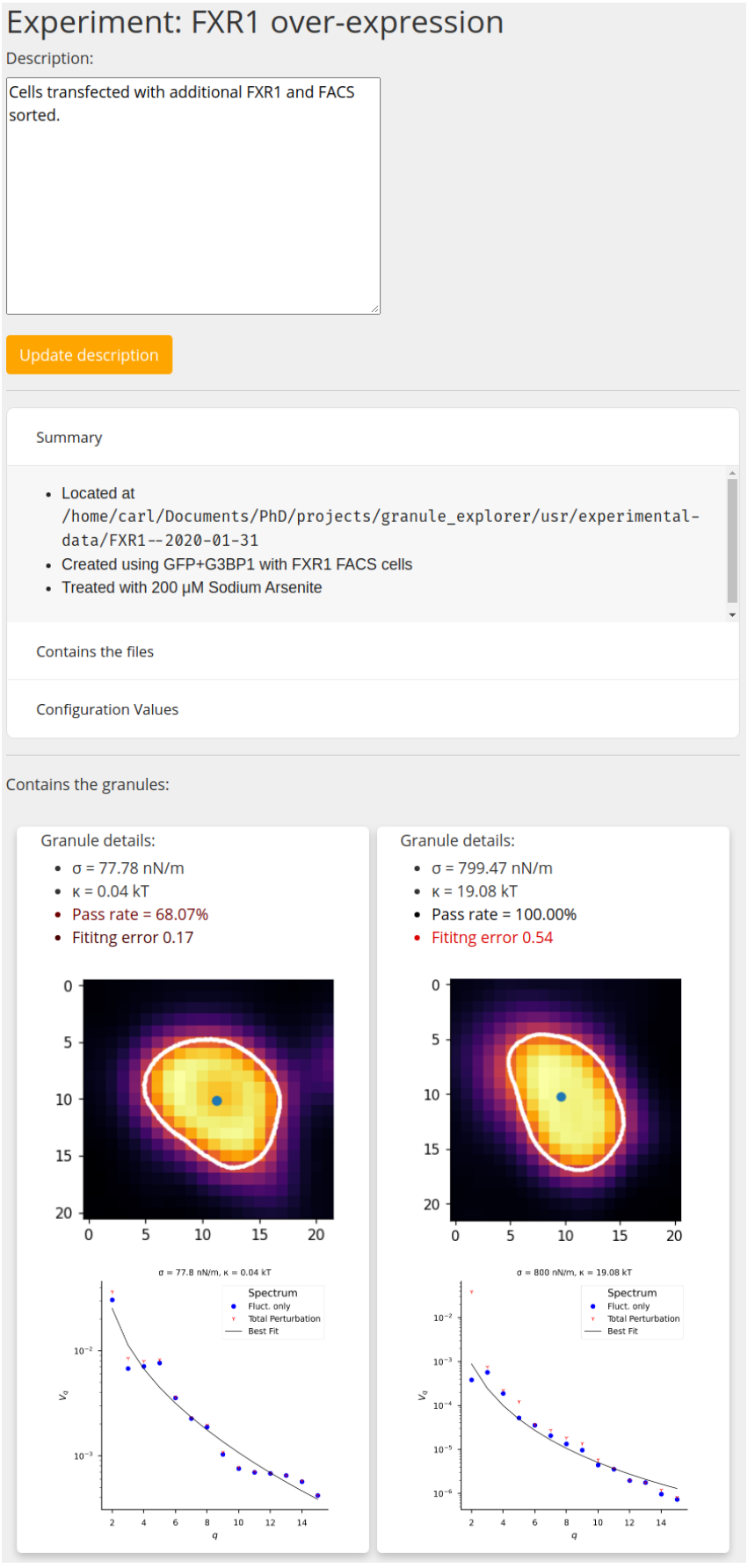

Figure 4.4.2: Screenshot showing how the experiment can be broken down in detail, allowing the user to inspect individual granules within a experiment, including images of the spectrum fitting and the boundary detection.

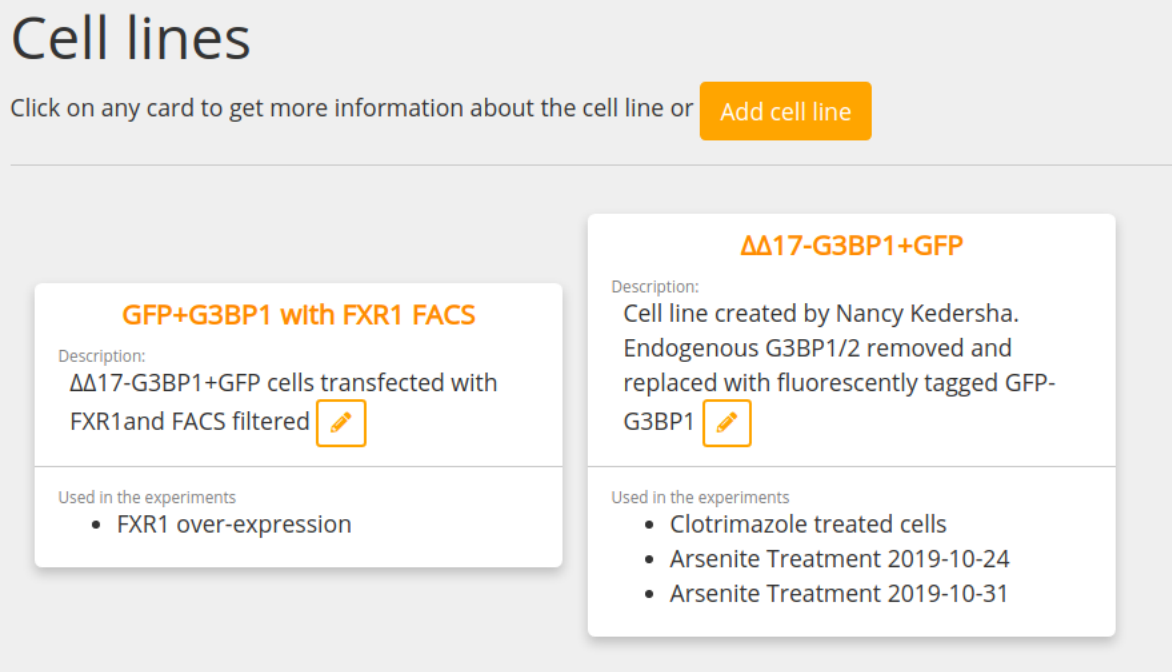

Figure 4.4.3: Example screenshot of the cell line summary in the granule explorer, showing the user provided description of the cell line and links to the experiments in which the cell line is used.

4.4.1.2 Data Insight

Typically the result of a scientific study is a set of figures that summarises the results of the analysis. Currently, the majority of these plots are static and presenting the data in this way can mean that a great deal of information can be lost and it is nearly impossible to link points in plots to entries in raw data easily. In contrast, interactive data visualisation helps the author to quickly explore the data and investigate trends that may be hidden in the summary figures.

To this aim, we provide an interactive plotting tool for the granule database. This aggregates data across multiple experiments and allows interactive filtering of granule properties, to a range of radii and maximum fitting error, but also the selection of individual granules for inspection. Figure 4.4.4 is an example screenshot of this plot, where we see data split by the user provided treatment.

Selecting any point in the top scatter plot will provide more detail for the given granule, including the fit spectrum shown in the bottom half of the figure.

4.4.2 Reproducible research

When designing scientific software, it is essential to consider not only the tools made available to the user but also that other groups can reproduce and verify this work. For instance, while

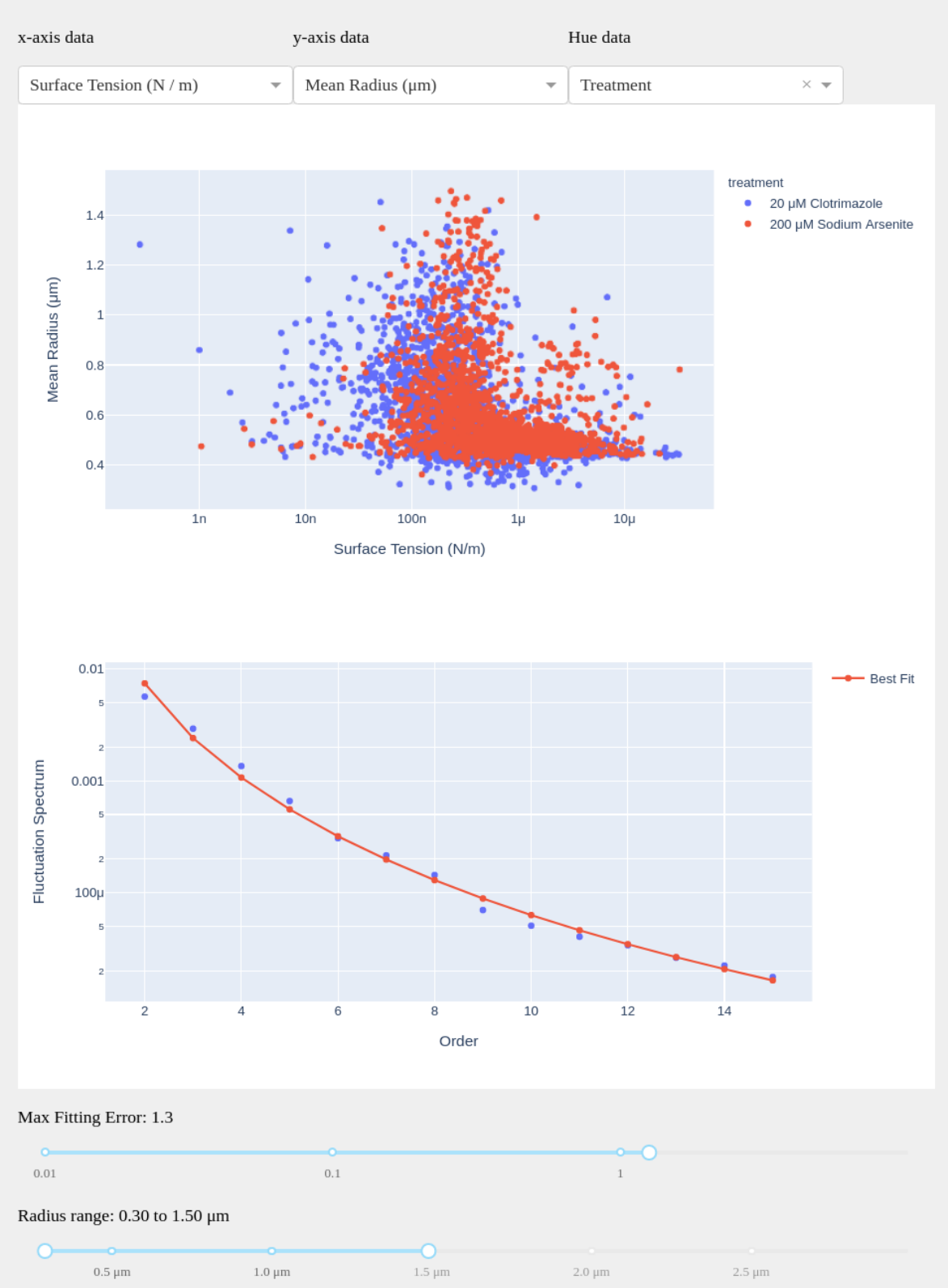

Figure 4.4.4: Screenshot of the data exploration tools. The plot columns and colour split of the data may be change by using the drop down menu at the top of the graph including surface tension, bending rigidity or radius of the granules. The user provided categories, such as the stress treatment, may be used to split the data. Finally, the quality of the fit and boundary detection pass rate may also be plotted. Sliders along the bottom of the figure allow for interative filtering of the data.

the granule detection steps can also be implemented in a general microscope image processing software such as ImageJ/Fiji [152, 150] or CellProfiler [153], the analysis with these packages have to be automated using custom-written scripts, which then require further steps to merge them with the rest of the workflow. Therefore, it may still be difficult for other users to reproduce the workflow, even when the raw data is made available [154]. In the worst-case scenario, parameters may be provided interactively by the user and then not recorded or published, making validation impossible.

In the granule explorer package, each experiment's entire analysis is contained within one directory tree containing: the configuration files used to generate the results, intermediate files, final figures and data tables. Combined with the use of the `snakemake` workflow management system [155], means that each step of the analysis and every parameter used, is explicitly recorded. `snakemake` performs the analysis steps automatically, from microscope files to final results and figures. This not only makes the analysis simple to run for non-technical users, but also means that the exact analysis can be reproduced and verified by external groups.

The package is also published in `github.com` for version control. We ensure that analysis can be repeated exactly, even if major changes have since been introduced into newer versions of the code.

4.4.3 Publishing the package

A core step of making code available involves taking steps to ensure that the software will run on a user's machine without undue difficulty. We, therefore, link the code with a continous integration (CI) service, Travis CI, `http://travis-ci.org`, which automates installation and testing of the software on several test Linux and macOS virtual machines[4] whenever a change is pushed to the code repository. This allows us to be confident that the software runs not only on the computers we used to develop the code but also on many different setups that are common in the community.

A core part of a CI setup is testing of the code, this is provided at the level of individual functions by unit tests. These test the smallest logical blocks of the code are producing the expected output from given test data, from verifying that images are loaded correctly from sample microscope files to fluctuation magnitudes are being correctly averaged with time. The simulations in section 4.2 are then used to validate the interaction between these functions.

Importantly, CI is run every time the code repository is updated, which means that we can

be confident that any new code does not break older components and the new code does what is expected. This becomes increasingly important as other authors begin to contribute.

4.5 Experimental Results

4.5.1 The base shape of the stress granule must be accounted for

We initially performed the analysis using the theory covered in section 4.1, without any other corrections, on stress granules induced with 200 µM sodium arsenite in U2OS cells. This gave us a mean surface tension of approximately 100 nN/m as shown in fig. 4.5.2.b, which was at least an order of magnitude lower than the surface tension values for the similar biological condensates discussed in sec. 4.1.

This assumes that the base shape of the granule is spherical. However, visual inspection of the granule in fig. 4.5.1.a and tracking of the granule boundary with time in fig. 4.5.1.b shows that this is not a good assumption. Therefore, we include the correction covered in sec. 4.2.1.2 to separate the fluctuating and constant components of the granule boundary. Instead of fitting the experimental spectrum directly to the theoretical spectrum, we instead fit the theoretical spectrum to the fluctuating component,

$$\mathcal{F}_q^2 = \left\langle |\mathcal{V}_q|^2 \right\rangle - |\langle \mathcal{V}_q \rangle|^2 \ . \qquad \text{(4.2.8 revisited)}$$

Not including this correction means that the average shape of the granule is erroneously included in the fluctuation magnitudes, which leads to an overestimation of the lower fluctuation orders as shown in fig. 4.5.2.a. Overestimating the size of the fluctuations in this way leads us to underestimating the difficultly in deforming the surface and a corresponding underestimation of the granule surface tension by an order of magnitude as is shown in fig. 4.5.2.b. We see the experimental fluctuation spectrum with this correction fits well to the theoretical spectrum.

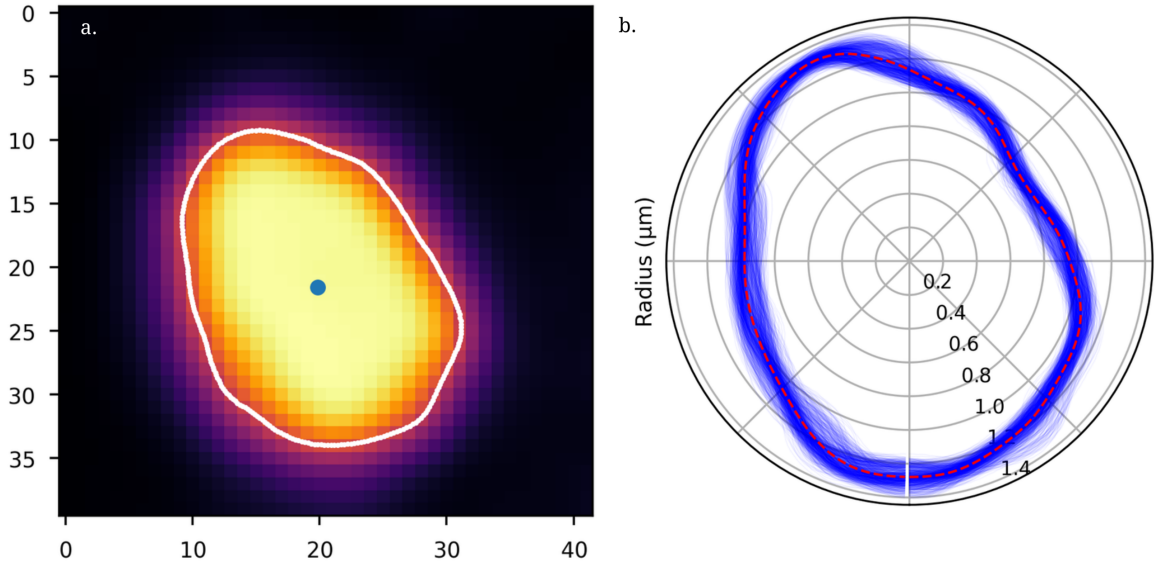

Figure 4.5.1: Quasi-spherical nature of stress granules in cells treated with 200 μM sodium arsenite. **(a)** Cropped first frame of the microscope image from an arsenite treated cell, with the granule boundary drawn in white. **(b)** The fluctuating boundary of the same granule is shown in blue for each frame of the analysis. The mean shape is shown in red and is highly non-spherical.

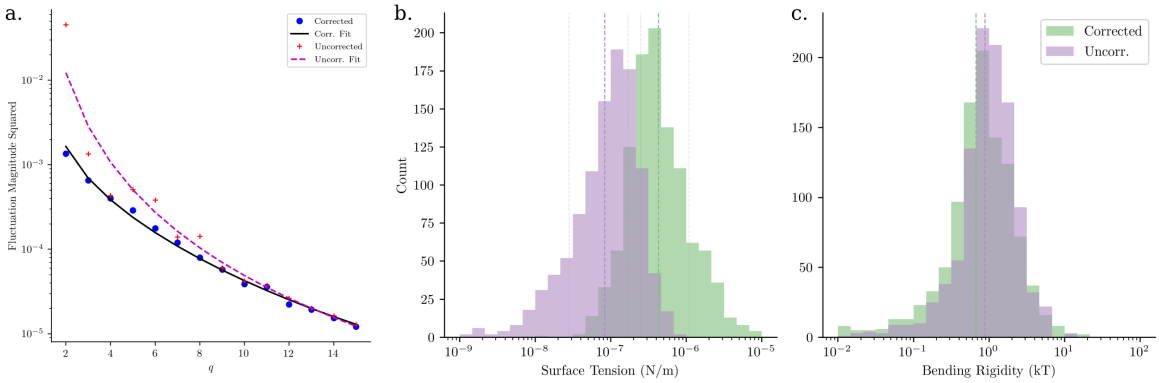

Figure 4.5.2: Comparison of the fluctuation analysis with and without corrections to the base shape of the granule. **(a)** The total experimental perturbations (uncorrected) are plotted with a red cross while the fluctuating components (corrected) are shown as blue dots. The non-spherical nature of leads to large overestimation of the lower order terms and poor fitting to the spectrum. **(b)** Not accounting for the quasi-spherical base shape leads to an underestimation of the surface tension by an order of magnitude as the surface tension dominates for the lower order terms. **(c)** As the bending rigidity dominates the higher-order terms, it is mostly unaffected by removing the constant terms from the experimental spectrum.

4.5.2 Surface tension alone is not enough to explain granule shape

In a membraneless organelle, we would expect that the bending rigidity is negligible and to test this, we take the limit of $\kappa \to 0$ in eq. (4.1.12) to give a spectrum that depends only the surface tension,

$$\lim_{\kappa \to 0} \left\langle |\mathcal{V}_q|^2 \right\rangle = \frac{k_\mathrm{B}T}{\sigma R^2} \sum_{l=q}^{l_\mathrm{max}} \frac{N_{lq} P_{lq}^2(0)}{(l-1)(l+2)} \ . \tag{4.5.1}$$

In fig. 4.5.3.a we see that this surface tension only spectrum does not fit the observed fluctuations for this sample granule, and while it may be adjusted to fit well to the to first few orders, it is unable to account for the higher order terms.

For completeness, we can also take the limit of $\sigma \to 0$ in eq. (4.1.12), to give a spectrum that depends only on the bending rigidity,

$$\lim_{\sigma \to 0} \left\langle |\mathcal{V}_q|^2 \right\rangle = \frac{k_\mathrm{B}T}{\kappa} \sum_{l=q}^{l_\mathrm{max}} \frac{N_{lq} P_{lq}^2(0)}{(l-1)(l+2)(l+1)l} \ . \tag{4.5.2}$$

This spectrum alone is also not enough to explain the observed fluctuations. In particular, we see that it fits best to the higher order terms. We can explain this as bending rigidity contributes a component that scales with q^4 while surface tension with q^2, causing the bending rigidity to dominate for the high q terms. Therefore, for this granule we require both surface tension and bending rigidity to capture the full fluctuation spectrum.

We wish to see if this applies to all granules. Therefore in fig. 4.5.3.b and fig. 4.5.3.c, we compare the fitting error for when the full spectrum with surface tension and bending rigidity are used, and when only the surface tension or bending rigidity is accounted. The change in fitting error is shown with a horizontal line for each granule example, with black dots indicating cases where the full spectrum is considerably better and the orange dots where the fit qualities are similar. From these steps, we find that surface tension and bending rigidity are both equally important in the model, and removing either significantly lowers the fitting quality. However, while there is a clear interpretation for the surface tension in the LLPS droplet, the nature of the bending rigidity is unclear.

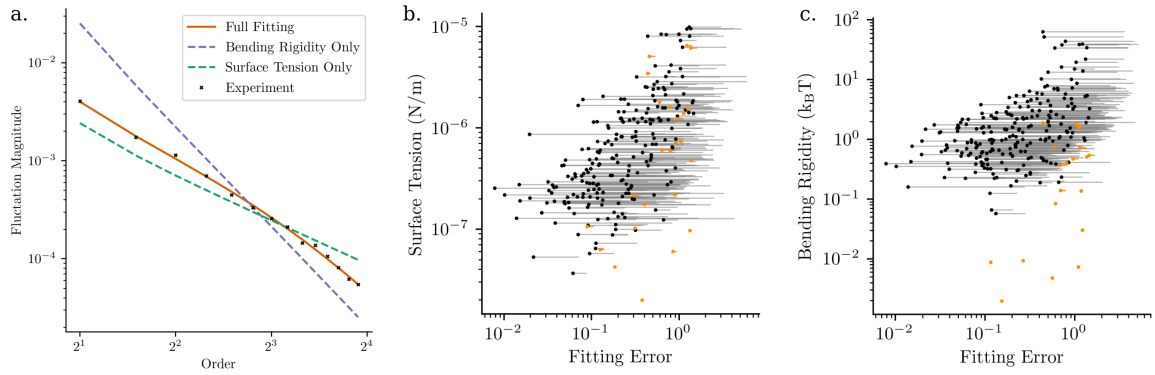

Figure 4.5.3: (a) An example experimental fluctuation spectrum, showing fits to theoretical spectra. The surface tension-only spectrum (green dashed) can only fit the lower order terms but not the full experimental spectrum, whereas the bending rigidity-only spectrum fits well for only the higher order terms. Therefore, we see that we must include both surface tension and bending rigidity in the model. **(b)** For a sample of granules, we show the change in fitting error when surface tension is removed with a horizontal line In all cases we see that the fitting quality is worse when the surface tension is removed. **(c)** Similarly to above, we show the change in fitting error when bending rigidity is removed from the model. For clarity we plot only 300 arsenite treated granules in panels **(a)** and **(b)**, approximately one-tenth of the total number of measured granules and the same trend applies to granules caused by other treatments.

4.5.3 Comparison between granule treatments

In this section, we compare the results for the granules with arsenite and clotrimazole treatments. After filtering the granules as discussed in section 4.3.2.3, we collected data from 1,796 granules in cells treated with 200 µM sodium arsenite, and 1,986 granules from 20 µM clotrimazole treated granules.[1]

The surface tension and bending rigidity of the two treatments are log normal distributed with a (geometric) mean surface tension of (0.56 ± 0.05) µN/m under the arsenite treatment and (0.36 ± 0.06) µN/m under clotrimazole as shown in fig. 4.5.4.a.

The mean bending rigidity is $(1.2 \pm 0.2)\, k_B T$ and $(1.6 \pm 0.3)\, k_B T$ for clotrimazole and arsenite treatments respectively. While this is much lower than $20\, k_B T$ we might expect for a bi-layer vesicle [156], it is similar to the thermal energy of the system and non-neglible. The distribution of bending rigidity values is shown in fig. 4.5.4.b.

We use the granule radius as a marker of granule maturity rather than the time since treatment as granule formation depends on the cell cycle. Therefore, not all cells will start to form granules at the same time after treatment. Additionally, one mechanism of granules growth is by coalescence which leads to a sizeable stochastic influence in granule size with time. When examining the surface tension of the droplet as a function of radius we see that

1. Materials and methods section 2.1.2.

the mean surface tension of the granule decreases rapidly with the radius until around 0.6 μm, beyond which the surface tension of the granules is independent of size. For all granule radii, we see that the surface tension of the clotrimazole granules is lower than that of the arsenite treatments, but conversely, the bending rigidity is higher.

The comparison between the arsenite and clotrimazole granules underlines the importance of correcting for the granule base shape. Without these corrections, we would have concluded the arsenite granules have a lower average surface tension. To rationalise this further, we track the granule boundary with time, where we see a distinction between the two treatments. An example of a clotrimazole granule is shown in fig. 4.5.5.b and we see that the granule fluctuates a great deal, but averages out to a roughly circular shape. In contrast, the arsenite treated granule in fig. 4.5.5.a has an irregular mean shape and—due to the higher surface tension—fluctuates a small distance from that position.

This suggests that there is some internal structure in the arsenite granule not present in the clotrimazole granules. We wish to investigate if this same trend occurs across the rest of the granules. To do so, we collect the fluctuating, $\mathcal{F}_q$, and constant components, $\mathcal{C}_q$. In the clotrimazole treated cells we find that the these terms are similar in magnitude across the granules, as shown in fig. 4.5.4.e. however in the arsenite treated granules there is a much larger constant component to the granule shape that does not change with time, with a smaller fluctuating component on top of this.

4.5.4 Additional treatments

We now extend the analysis to cell lines that are over expressing stress granule granule related proteins.

Caprin1 over-expression

Caprin1 is another important stress granule related protein, that unlike FXR1 rapidly recovers during photo bleaching. This was provided by a tet/on Caprin1 system, which expresses additional Caprin1 as a function of doxycycline in the media. The cells are moved to doxycycline positive medium 24 hours before experiment, allowing time to express additional Caprin1.

Unfortunately, this analysis had to be halted due to external factors (COVID), and so only 188 Caprin1 over-expressing granules were able to be analysed. Figure 4.5.6 gives the distribution of surface tension and bending rigidity when compared to the ΔΔ17-G3BP1+GFP

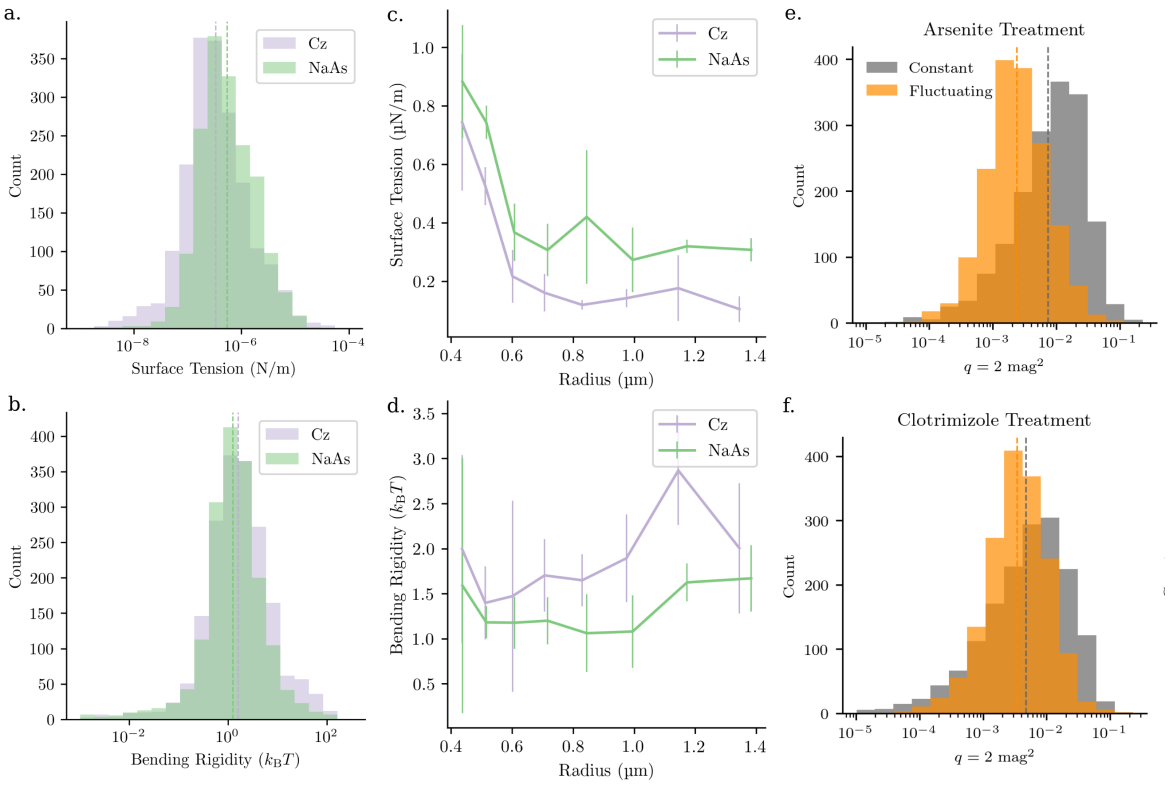

Figure 4.5.4: Comparison of arsenite and clotrimazole granules after the shape correction is applied. **(a)** and **(b)** Surface tension and bending rigitity distribution of the granules under both treatments **(c)** Surface tension of the granules as a function of radius with the standard error plotted. The surface tension is higher under the arsenite treatment. **(d)** Bending rigidity as function of radius. In constrast to the surface tension, the bending rigidity is higher in the arsenite trement. **(e, f)** Comparison of the magintudes of the 2nd order terms. In the clotrimazole treatment, the magnitude of the fluctuating and constant terms are of similar magintudes; whereas for the arsenite treatment there is much more significant contribution from the constant components.

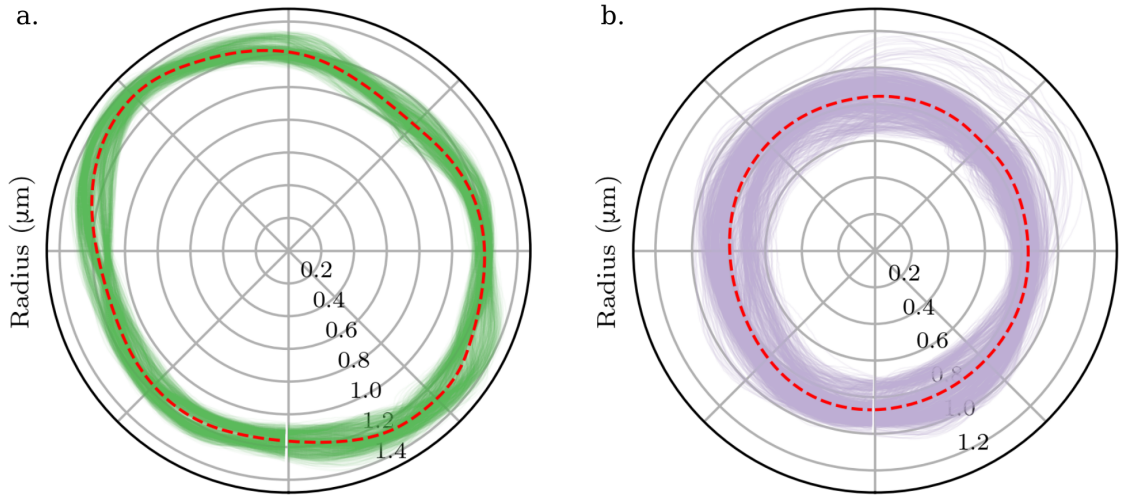

Figure 4.5.5: Tracking of the granule interface during the experiment. The position of the boundary at each frame is given by a solid line and the mean granule shape is given by the dashed red line. **(a)** Example of an arsenite treated granule, where we see that the mean shape of the granule is significantly non-circular. In contrast, the example of a clotrimazole treatment granule in panel **(b)** has a more circular mean shape, but the boundary fluctuates more.

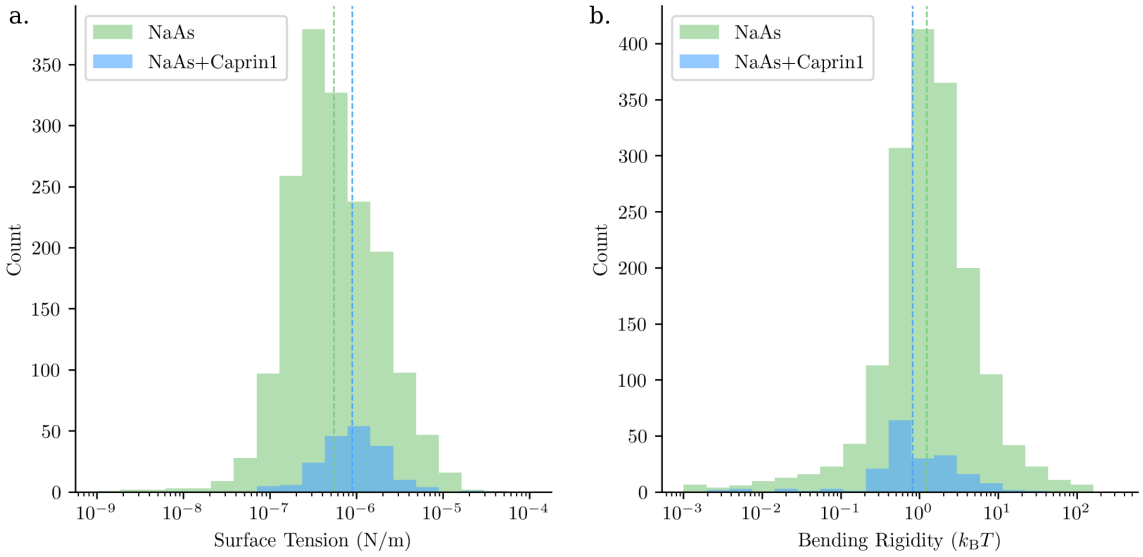

Figure 4.5.6: A limited number of granules in Caprin1 overexpressing cells. **(a)** The surface tension is higher in the overexpressing cells. **(b)** The bending rigidity is higher in the overexpressing cells. However, note that these results are not statistically significant.

cells. From the data currently gathered, the surface tension of the Caprin1 over expressing cells is higher than the control cells, but the bending rigidity is lower. However, due the limited number of granules, this may change as more data is gathered.

FXR1 over-expression

Fragile X mental retardation syndrome-related protein 1 (FXR1) is a protein found in stress granules [38, 59] that when over-expressed can lead to granules that are qualitatively more irregular. It is possible that this shape irregularity is linked to fibril formation within the granule. As discussed in the introductory chapter, this is of medical interest as fibrils will remain after granule disassembly. The accumulation of these fibrils lead to deleterious effects in the cell and are associated with neurodegenative diseases.

A gene for the expression of mCherry flourophore tagged FXR1 was transfected into the cells[2] and when combined with the endogenous FXR1, this leads to an over expression of FXR1 in the cell. The cells are then treated with the same 200 µM sodium arsenite treatment. As a function of radius, we see in fig. 4.5.7.a that under the arsenite treatment, the surface tension does not change significantly when FXR1 is over expressed in the cells. In contrast, we see in fig. 4.5.7.b, the bending rigidity in the FXR1 over expressing cells is significantly lower than in the similarly arsenite treated control cells. We perform the same analysis of splitting

2. Materials and methods section 2.1.2.2

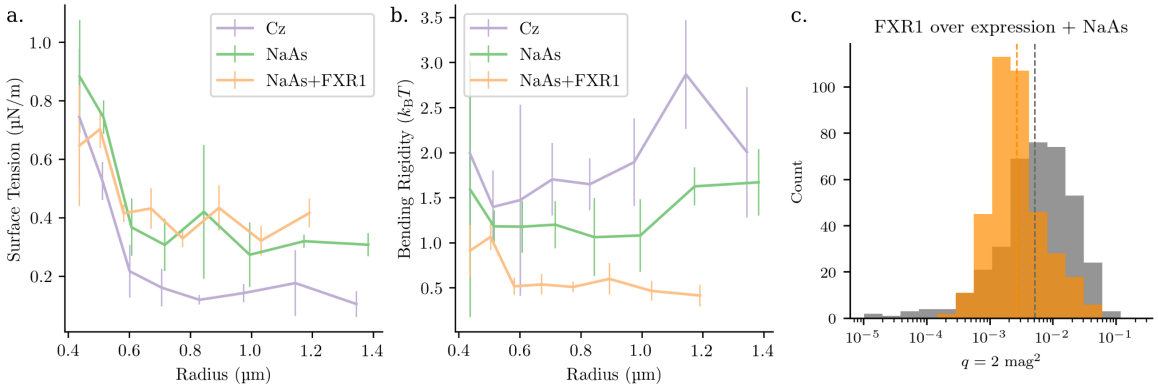

Figure 4.5.7: Properties of the granules in the FXR1 overexpressing cells treated with soduium arsenite are given in orange. The treatments of the ΔΔ17-G3BP1+GFP control cells are as given in fig. 4.5.4. **(a)** Surface tension as function of radius for stress granules. The surface tension is indistinguishable in the two NaAs treatment cases. **(b)** The bending rigidity is much lower in the FXR1 over expression cells. **(c)** The difference between the fluctuating (orange) and constant (gray) magnitudes are significantly smaller than in ΔΔ17-G3BP1+GFP cells treated with arsenite but larger than in the clotrimazole treatment.

the constant and fluctuating modes, in 4.5.7.c. We see that the constant terms are larger than the fluctuating terms, suggesting that there is a consistent irregular base shape in the granules in the FXR1 overexpressing cells, although this is not as pronounced as in the control cells.

The effect of the decrease in the bending rigidity under the FXR1 overexpression is shown in a simulation of the granule surface in fig. 4.5.8. Both simulated granules have a surface tension of 100 nN/m, but the decreased bending rigidity in the FXR1 overexpressing granule causes a much rougher appearance of the granule surface.

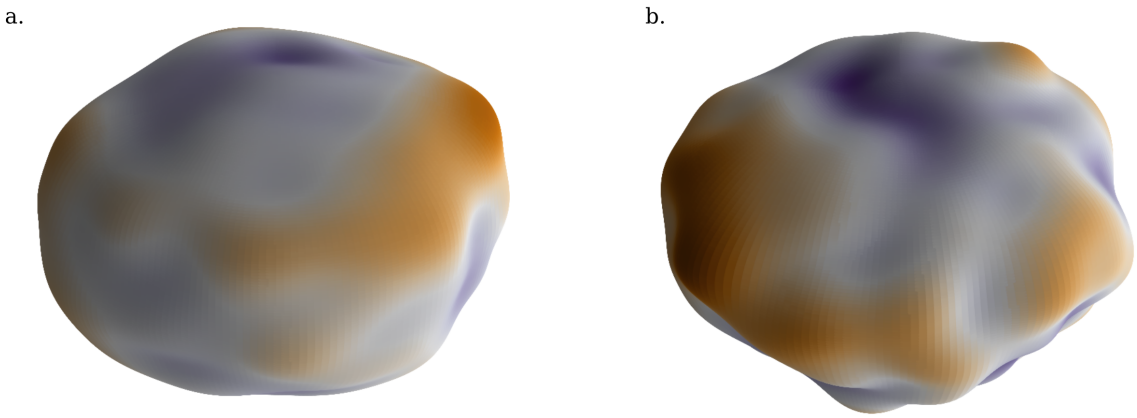

Figure 4.5.8: 3D simulations of a stress granule surface. **(a)** A simulated granule created with a bending rigidity of 1.5 $k_{\mathrm{B}}T$, corresponding to a arsenite treated granule in a control cell. **(b)** A granule with bending rigidity of 0.5 $k_{\mathrm{B}}T$, corresponding to a granule in an FXR1 overexpressing cell has a much rougher surface.

4.6 Discussion

4.6.1 Comparison to current estimates

There is currently a lack of accurate methods to measure the surface tension of LLPS droplets in-vivo, while several ways of providing order of magnitude estimates have been proposed. At present, to our best knowledge, there also has not been any report on the surface tension of stress granules.

Our measured surface tension values are $0.56\,\mu\mathrm{N/m}$ and $0.36\,\mu\mathrm{N/m}$ for the arsenite and clotrimazole treatments respectively. These values are much lower than what is found in simple liquid-liquid interfaces (typically of tens of mN/m) but it is worth noting that surface tension values as low as $0.1\,\mu\mathrm{N/m}$ can be found in colloidal mixtures [132, 133]. In fact, our results are of similar order of magnitude compared to those estimated for P granules of $1\mu\mathrm{N/m}$ using the approximation in eq. (4.1.1) [9, 2]. It also correlates well with the range of surface tension of $1\,\mu\mathrm{N/m}$ to $5\,\mu\mathrm{N/m}$ for P-granule protein PGL3 droplets measured in-vitro using optical tweezers upon variation of the salt concentration [135].

The only other approach to directly measure the surface tension of an LLPS droplet in a biological system in-vivo was by Caragine et al. [157]. This method also used the fluctuating surface of the droplet, but only the total fluctuation is considered, rather than the power spectrum. In analogy to eq. (4.1.1), the surface tension is estimated as $\sigma = k_\mathrm{B}T/\langle u^2\rangle$, where u is the total fluctuation magnitude. Again, their estimate for surface tension of $\sigma = (1.5 \pm 0.5)\,\mu\mathrm{N/m}$ for human nucleoli is still of similar order to our measurement. The approach by Caragine et al. is more limited compared to the current work for a number of reasons. First, it is based on the planar interface derivation, and it does not include the corrections to the shape of the droplets. Second, this simpler approach loses any information about the spectrum of the fluctuations. It is only by studying the fluctuation power spectrum, as is done in our method, that we are able to verify that there is the distinctive l^{-2} component that corresponds to surface tension contribution. At the same time, we have also shown that LLPS droplets are

not simple droplets. There is an additional elastic contribution that emerge as non-negligible bending rigidity component, which the Caragine approximation does not account for. Based on our own results, this typically leads to an overestimation of the role of surface tension.

4.6.2 Sources of bending rigidity

We have shown that we must include a bending rigidity contribution to fit the observed experimental fluctuation spectrum.

Our observed value of 1.2 k_BT is much lower than the typical bending rigidity of a bi-layer membrane of 20 k_BT [156, 136]; nonetheless, it is still non-negligible. A possible reason for this term is due to surfactant-like effects in LLPS droplets, in which species of molecules preferentially locate at the interface between the droplet and cytoplasm. A classic example of surfactants is lipid molecules. At a water-oil interface, their hydrophilic heads would favour facing the water, while their hydrophobic tails face into the oil. This is known to reduce the surface tension and to introduce a weak bending rigidity [15]. In the context of stress granules, we may speculate a number of molecules which may prefer to be at the droplet interface. In the core-shell model of granule formation, FXR1 is found to locate in the outer shell of the granule [72]. Indeed, overexpression of FXR1 causes a notable decrease in the bending rigidity of the granule, which may suggest that overexpression of FXR1 leads to a disruption of the structure of the shell, making it much easier to deform. In addition, it has been shown LLPS droplets are often caged by an elastic network [158] and a possible hypothesis is that the presence of micro tubules surrounding the droplets can give rise to an effective bending rigidity. At present, it is not possible to probe the detailed internal structure of the granules with confocal microscopy. It would be interesting to investigate this in the future with higher resolution microscopy, such as super resolution STED or electron microscopy methods.

4.6.3 Possible improvements

Our flicker spectroscopy method may underestimate the absolute value of the surface tension. One possible source of underestimation is due to the limitations of confocal microscopy. In particular, this is due to the blurring of the moving interface during the exposure [159, 160] and the non-zero height of the image plane [156], which has been shown to lead to underestimation of up to 50% for lipid vesicles. However, at present we are unable to make the same correction in the stress granule case without detailed knowledge about the time series fluctuations of the

droplets.

The second source of uncertainty may be due to our assumption that the fluctuations are thermal. We know that there are active, ATP-dependant processes that drive molecules within the cytoplasm, and potentially in the droplets themselves. The energy scale for active fluctuations is often larger compared to thermal sources [161, 162], which would make it seem like the interface is easier to deform. This would then lead to an underestimation of the surface tension and bending rigidity.

Delineating active and passive fluctuations is an important but challenging future work. For example, clotrimazole is a weak mitochondrial poison [12, 163] and so we might expect this to lower the level of ATP in the cell and reduce the magnitude of the non-thermal fluctuations. Contrary to this expectation, we instead find that the measured surface tension increases under the clotrimazole treatment. However, it is known that there is a compositional change to the stress granules under clotrimazole treatment, and so this may be the dominant effect [164]. A reagent such as sodium azide may be used to inhibit ATP hydrolysis [2], but at the same time this causes many other immediate deleterious effects in the cell, including a stress response that obscures ATP related effects on the granules.

4.6.4 Limiting factors in data acquisition

We see that there is a wide distribution of surface tension and bending rigidity across the measured stress granules. Therefore, we are required to image a large number of granules to reduce the uncertainty in the measurements. Due to the close agreement of the fitting between the theoretical and experimental spectra, we believe that the majority of this variation reflects biological variation between the droplets rather than uncertainty in our methods. However, there is still a limit to the rate at which we can collect data, as we require approximately one minute per microscope time series. While the spinning disk microscope does allow us to capture several granules at once, we are not able to decrease the time taken for the analysis, as we are required to image for longer than the relevant fluctuation modes.

Transfection, as is done with the FXR1 over expressing cells, is a typically a very noisy process. Only a minority of cells—typically 1 in 20—respond to the transfection and of these cells there can be orders of magnitude of intensity of the expression of the gene. This variation can be seen from the FACS sorting summary in fig. 4.6.1. These cells are typically unsuitable for analysis. The low transfection rate vastly limits the number of cells that can be analysed

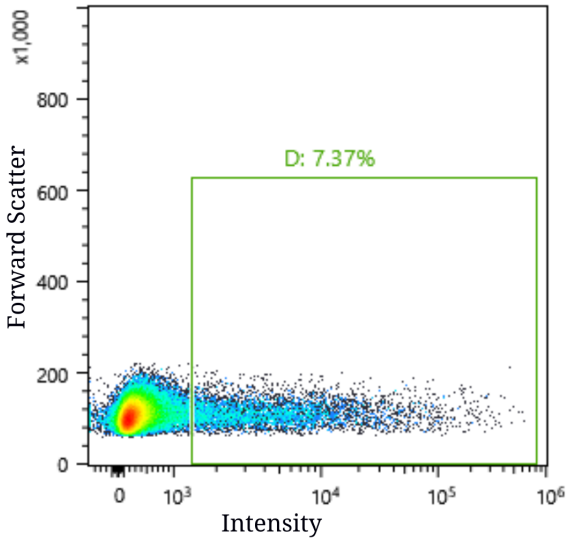

Figure 4.6.1: Screenshot from the FACS of FXR1-YFP (yellow florescent protein) transfected cells. The x-axis corresponds corresponds to the measured intensity of YFP, the y-axis is irrelevant for this discussion. We see that only approximately 7% of the cells express FXR1-YFP and of these cells there is wide range of intensity values.

in a given experiment and the wide range of fluorescence intensities also complicate imaging. While our methods are able to account for some range in the granule intensities within a single image, we are still limited by the dynamic range of the microscope itself. The expression level would also have to be disentangled from the normal biological variation and the imaging time soon becomes dominated by manually searching for cells suitable for analysis. Fluorescence-activated cell sorting (FACS) helps deal with these issues by only keeping the cells within a particular range of expression levels. However, FACS is an expensive process and is time-consuming as a correspondingly larger number of cells must be cultured to give an acceptable yield after sorting.

4.6.5 Conclusion

We believe we have a powerful method for investigating the surface tension and bending rigidity of LLPS droplets in a living cell in a minimally invasive way. The slight underestimate of the surface tension due to microscopy effects can be accounted for once the temporal fluctuation spectrum of granules is better understood. Performing the time series analysis of the fluctuations can give further insight into the structure of the granule, and we explore the benefits as well as potential experimental and theoretical challenges in the Chapter 5.

Flicker spectroscopy is currently the only method to analyse LLPS droplets in living cells. This is a critical advantage over other methods as highlighted by Jawerth et al. [135]. The properties of LLPS droplets depend not only on the composition of the droplet itself, but also on the composition of the background cytoplasm. This places a limit on in-vitro experiments, as while the droplet composition may be investigated, less attention is paid to the background

of the system, and in-vitro systems cannot approach the complexity of the cytoplasm. So far, we have demonstrated the use of flicker spectroscopy to make clear distinctions between the arsenite and clotrimazole treatments, as well as the FXR1 over-expressing cells.

Additionally, as flicker spectroscopy requires only a confocal microscope, any group should be able to collect the required data, which can then easily be analysed by the provided granule-explorer package. This then serves as a means to gather quantitative data on granule properties, and to get some insight into the structure from the ratio of constant to fluctuating terms in the fluctuation spectrum, which is not available in any other analysis. Therefore, FS may be used a first step to screen potentially interesting mutations or treatments of interest, before more time-consuming analyses such as electron microscopy or optical tweezers.

4.7 Appendix to Chapter 4

4.7.1 Spectrum derivation for a flat interface

This section illustrates how the fluctuation spectrum can be derived for the simplest case of a flat interface. For the full derivation in the spherical case, see [165, 166].

We adapt the derivation from [136]. We investigate fluctuations across a flat plane of area $L \times L$. the fluctuations of this surface are described according to the Monge representation, as it is ideally suited to modelling fluctuations on a plane. As shown in fig. 4.7.1, in the Monge representation, the shape of the surface is described by the height function $h(x, y)$ [1]

We can then expand height function by its Fourier components,

$$h(x, y) = \sum_{\vec{\mathbf{q}}} h_{\vec{\mathbf{q}}} e^{i\vec{\mathbf{q}}\cdot\vec{\mathbf{r}}} \,, \tag{4.7.1}$$

where $\vec{\mathbf{q}}$ is the frequency vector and is given as

$$\vec{\mathbf{q}} = \frac{2\pi}{L} \begin{pmatrix} n_x \\ n_y \end{pmatrix} \,, \tag{4.7.2}$$

where $n_x, n_y \in \mathbb{Z}$ and L is the length of the plane. If we assume there is no spontaneous curvature, then we may give the energy of the interface as

$$\mathcal{H} = \int_S \mathrm{d}A \left[\frac{\kappa}{2} H^2 + \sigma \right] \,. \tag{4.7.3}$$

In the small fluctuation approximation, the area element in the Monge representation is given by $\mathrm{d}A = \left[1 + (\boldsymbol{\nabla} h)^2/2\right] \mathrm{d}x\, \mathrm{d}y$. The mean curvature, H is given by, [167, 166],

$$H = \frac{1}{2} \boldsymbol{\nabla} \cdot \left(\frac{\boldsymbol{\nabla} h}{\sqrt{1 + (\boldsymbol{\nabla} h)^2}} \right) \,, \tag{4.7.4}$$

1. Similarly to our radial describution of the spherical interface, this representation is not able to model interface where there are multiple values of h for a given (x, y).

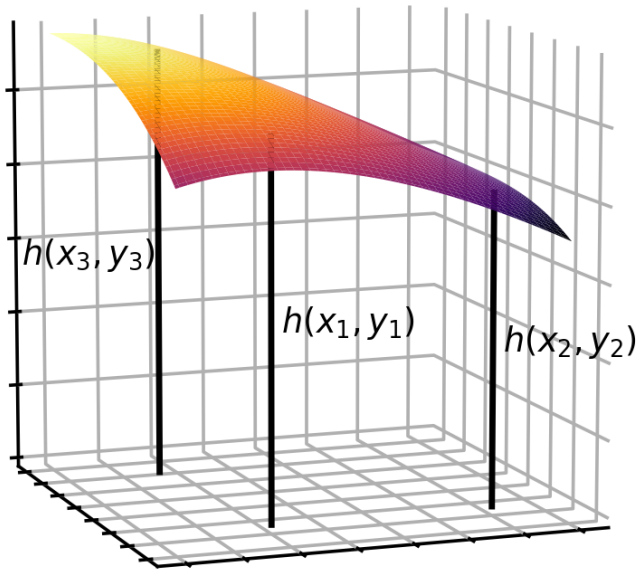

Figure 4.7.1: Three points on a interface described in the Monge representation. The interface is parameterised by its height above the $Z = 0$ plane.

which in our limit of small fluctuation, $|\boldsymbol{\nabla} h| \ll 1$, gives $H = \nabla^2 h/2$. As such, we can give the Hamiltonian, eq. (4.7.3), as

$$\mathcal{H} = \int \mathrm{d}x\, \mathrm{d}y \left(\kappa(\nabla^2 h)^2 + \sigma(\boldsymbol{\nabla} h)^2\right) . \tag{4.7.5a}$$

We now show how this can be derived. We can write the relevant gradients of the height function as follows

$$\boldsymbol{\nabla} h = \sum_{\vec{\mathbf{q}}} h_{\vec{\mathbf{q}}} i\vec{\mathbf{q}} e^{i\vec{\mathbf{q}}\cdot\vec{\mathbf{r}}} , \tag{4.7.6a}$$

$$(\boldsymbol{\nabla} h)^2 = \sum_{\vec{\mathbf{q}},\vec{\mathbf{q}}'} h_{\vec{\mathbf{q}}} h_{\vec{\mathbf{q}}'} (-\vec{\mathbf{q}}\cdot\vec{\mathbf{q}}') e^{i(\vec{\mathbf{q}}+\vec{\mathbf{q}}')\cdot\vec{\mathbf{r}}} , \tag{4.7.6b}$$

$$\boldsymbol{\nabla}^2 h = \sum_{\vec{\mathbf{q}}} h_{\vec{\mathbf{q}}} (-q^2) e^{i\vec{\mathbf{q}}\cdot\vec{\mathbf{r}}} , \tag{4.7.6c}$$

$$(\boldsymbol{\nabla}^2 h)^2 = \sum_{\vec{\mathbf{q}},\vec{\mathbf{q}}'} h_{\vec{\mathbf{q}}} h_{\vec{\mathbf{q}}'} (q^2 q'^2) e^{i(\vec{\mathbf{q}}+\vec{\mathbf{q}}')\cdot\vec{\mathbf{r}}} . \tag{4.7.6d}$$

Substituting these terms into the Hamiltonian, eq. (4.7.5a), while making use of the Kronecker delta function,

$$\delta_{\vec{\mathbf{q}},\vec{\mathbf{0}}} = \int_{L\times L} e^{i(\vec{\mathbf{q}}\cdot\vec{\mathbf{r}})}\, \mathrm{d}^2 r , \tag{4.7.7}$$

we find that

$$E_{\text{bend}} = \int_{L\times L} \mathrm{d}^2 r \sum_{\vec{\mathbf{q}},\vec{\mathbf{q}}'} h_{\vec{\mathbf{q}}} h_{\vec{\mathbf{q}}'} e^{i(\vec{\mathbf{q}}+\vec{\mathbf{q}}')\cdot\vec{\mathbf{r}}} \left[\frac{1}{2}\kappa q^2 q'^2 + \frac{1}{2}(-\vec{\mathbf{q}}\cdot\vec{\mathbf{q}}')\right] \tag{4.7.8a}$$

$$= \sum_{\vec{\mathbf{q}},\vec{\mathbf{q}}'} h_{\vec{\mathbf{q}}} h_{\vec{\mathbf{q}}'} L^2 \delta_{\vec{\mathbf{q}}+\vec{\mathbf{q}}',0} \left[\frac{1}{2}\kappa q^2 q'^2 + \frac{1}{2}(-\vec{\mathbf{q}}\cdot\vec{\mathbf{q}}')\right] \tag{4.7.8b}$$

$$= L^2 \sum_{\vec{\mathbf{q}}} h_{\vec{\mathbf{q}}} h_{-\vec{\mathbf{q}}} \left[\frac{1}{2}\kappa q^4 + \frac{1}{2}\sigma q^2\right] \tag{4.7.8c}$$

$$= L^2 \sum_{\vec{\mathbf{q}}} \left|h_{\vec{\mathbf{q}}}\right|^2 \left[\frac{1}{2}\kappa q^4 + \frac{1}{2}\sigma q^2\right] . \tag{4.7.8d}$$

In the last step, we make use of the fact that the height function is real $h(\vec{\mathbf{r}})$ is real, which requires that the Fourier modes satisfy $h_{-\vec{\mathbf{q}}} = h^*_{\vec{\mathbf{q}}}$.

By the equipartion theorem each of these degrees of freedom has the thermal energy of the system namely, $E(q) = k_{\mathrm{B}}T/2$,

$$\frac{1}{2}k_{\mathrm{B}}T = \left\langle |h_q|^2 \right\rangle L^2 \left[\frac{1}{4}\kappa q^4 + \frac{1}{2}\sigma q^2\right] , \tag{4.7.9}$$

leading us to the final result

$$\left\langle |h_q|^2 \right\rangle = \frac{k_{\mathrm{B}}T}{L^2} \frac{1}{\kappa q^4 + \sigma q^2} . \tag{4.7.10}$$

This parallels strongly to the 3d spectrum,

$$\left\langle |\mathcal{U}_l^m|^2 \right\rangle = \frac{k_{\mathrm{B}}T}{\kappa} \frac{1}{(l-1)(l+2)[l(l+1)+\bar{\sigma}]} . \tag{4.1.7 revisited}$$

In the limit of large l, we see similar power trends for the order of the spherical harmonics, l, and the fluctuation mode, q.

Perceaux used this simple flat fluctuation spectrum as an approximation to the spherical system [142], arguing that this approximation holds well for their system, vesicles with approximate surface tension $\sigma = 20\,\mathrm{nN/m}$ and $\kappa = 15\ k_{\mathrm{B}}T$. However, in that work it is shown that this approximation is breaks down for the lower perturbation orders. As these are the terms that we are able to measure most accurately, we do not make use of this approximation in our work.

Table 4.7.1: Stencils of the image derivative kernels. In this table the five and seven tap kernels are truncated at 3 decimal places for conciseness, the full values are given in [148].

Name	$k_{\parallel}$	$k_{\perp}$
Fourth order central	$(1\ -8\ 0\ 8\ -1)/12$	1
Third order forward	$(0\ 0\ 0\ -11\ 18\ -9\ 2)/6$	1
Sobel	$(1\ 0\ 1)$	$(1\ 2\ 1)/8$
Scharr	$(-1\ 0\ 1)$	$(3\ 10\ 3)/32$
Five tap	$(0.104\ 0.292\ 0.000\ -0.292\ -0.104)$	$(0.030\ 0.249\ 0.439\ 0.249\ 0.030)$
Seven tap	$(0.018\ 0.125\ 0.193\ 0.000\ -0.193\ -0.125\ -0.018)$	$(0.004\ 0.069\ 0.245\ 0.361\ 0.245\ 0.069\ 0.004)$

4.7.2 Stencils

In table 4.7.1 we list the kernels that we compare in the image gradient analysis. We are interested in not only the size of the error but also its structure. In particular, if an anisotropic response will negatively affect the calculation of the directional derivative. Here we demonstrate the action of the stencils on the Gaussian function $f(x,y) = \exp\left[-(x/\sigma_x)^2 - (y/\sigma_y)^2\right]$. We compare the numerical derivatives calculated by the kernels to the analytical derivative given as

$$\boldsymbol{\nabla} f = -\begin{pmatrix} x\sigma_x \\ y\sigma_y \end{pmatrix} f \ . \tag{4.7.11}$$

A plot of the test function and the analytical derivative are shown in fig. 4.7.2.

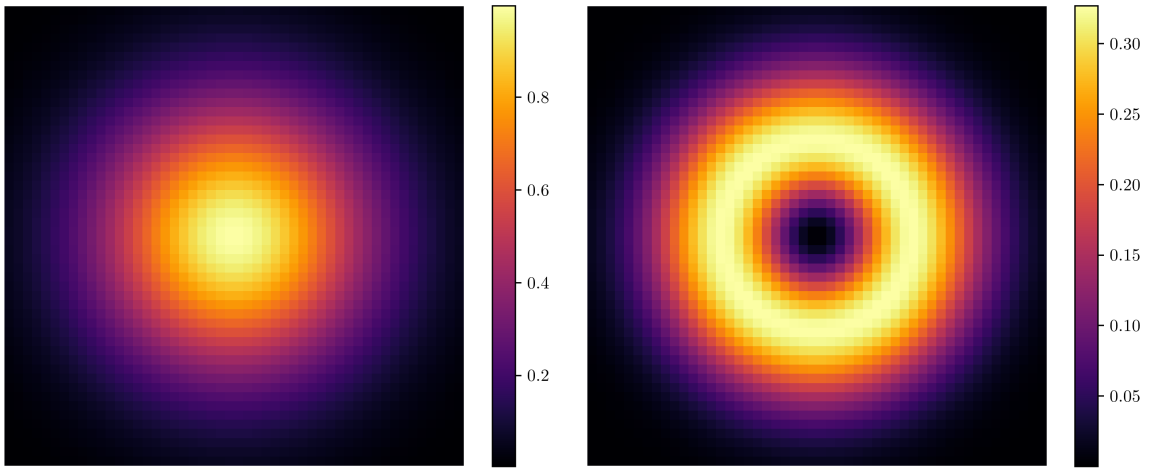

Figure 4.7.2: Gaussian test function and the magnitude of its derivative.

We have included a number of direct numerical derivatives. The magnitude and phase error of the kernels are given in fig. 4.7.3. The central fourth-order and forward third-order methods [168] have no smoothing components in the perpendicular direction. Both methods only evaluate four points per pixel, but the fourth order central method is far more accurate,

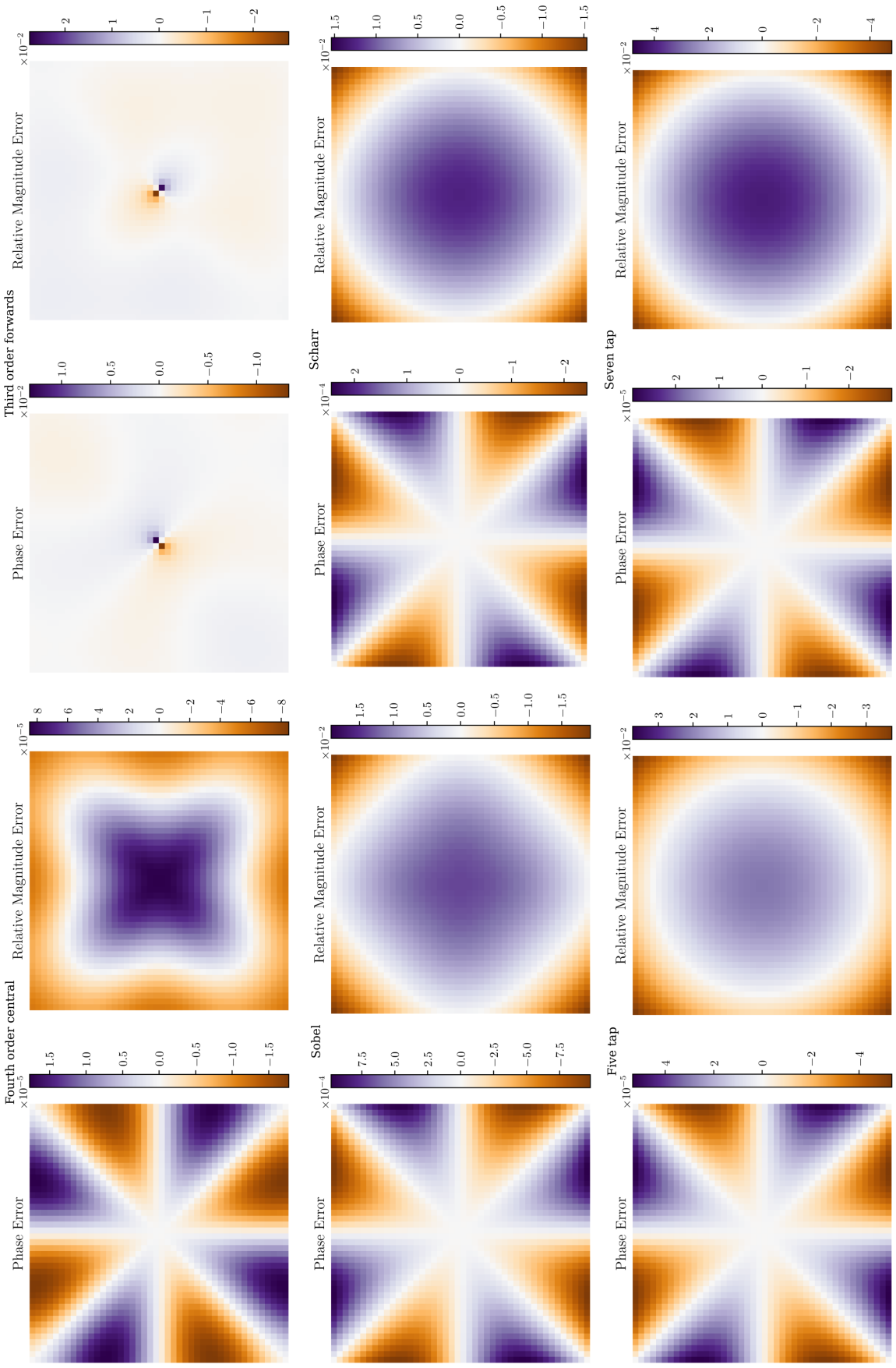

Figure 4.7.3: Magnitude and phase errors of the image derivative kernels. Although the seven tap, five tap and Scharr filters exhibit the least anisotropic responses, the fourth order central method has the lower error in both phase and magnitude.

as we might expect. These methods all display anisotropy.

The sobel filter, third order and fourth order kernels display a slight anisotropy where the diagonal terms are underestimated in comparison to the primary x, y-axes. The Scharr, five tap and seven tap kernels improve on this, with an identical response at all angles, as they are designed to [148].

4.7.3 Supplementary figures

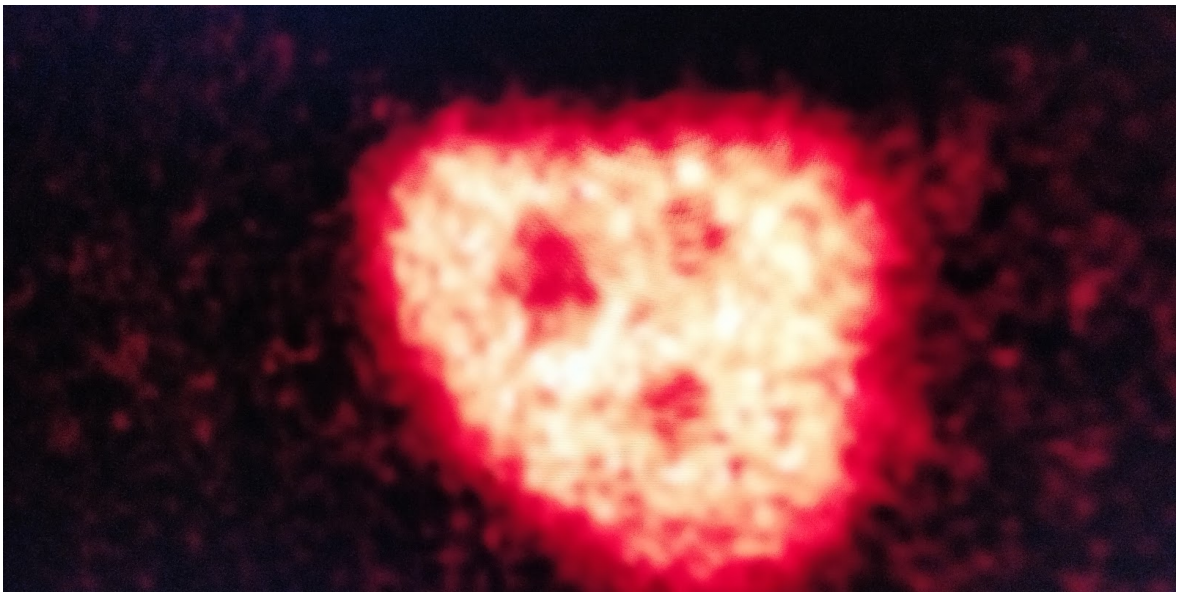

Figure 4.7.4: Example microscopy image of ternary structures within a stress granule. Dark voids are present within the bright GFP-G3BP1 region. The composition of the voids are currently unknown.

Chapter 5

Discussion

In this work we aimed to develop computational approaches to study stress granule dynamics and quantify their material properties in living cells. In Chapter 3 we introduced a reaction-diffusion model, that despite its relatively simple rules, was able to accurately capture the size and time distributions of granules formation and gain some insight into the microscopic behaviour of the granule components, in particular the nature of the material lost from the granule due to coarsening. We further outlined several scenarios that might be explored with a system of two aggregating components. The key challenge here is to parameterise the model parameters, particularly to relate them to experimental observables.

The simulation was also flexible enough to perform the in-silico experiments in Vietri et al, including diffusion while bound to a spherical surface and more complex interactions with the model geometry, such detecting if a particle a passes through a pore. We managed to make significant optimisations to the simulation, which greatly aided in the exploration of the parameter space. The optimisations of the memory reads are a significant step towards SIMD (Single Instruction, Multiple Data) optimisation in future work. Rewriting the collision detection to make use of SIMD on a CPU requires a good understanding of the underlying compiler behaviour, but would offer a substantial increase in the speed of the particle detection step as a single processor core could, optimally, calculate the distance between 4-16 particles in parallel [104]. A much more extreme approach would be to rewrite the code to run a on GPU (graphics processing unit), these are capable of thousands or millions SIMD operations in parallel, but are much worse at complex logic and would require a significant change in implementation of the diffusion and decay steps as well. However, in the best case scenario, the end result can be a one or two orders of magnitude increase in speed [102, 105].

Some packages do allow for rigid body accumulation of particles, where a particle freezes in place when it interacts with another particle, allows for the build up of complex 3d structures. Our method of accumulation into an increasingly large droplet is a more natural fit for an LLPS system, but a combination of the two approaches may help in modelling scaffold-client structures or the build up of fibrils with in the granules.

Similarly to the granule explorer, this code could also be made into a package. It would face competition from other more mature packages such as Gromacs and ReaDDY, but our software does offer a couple of unique advantages, mainly regarding the attrition of material from droplets. Although, it would be important to first refine the user interface and documentation, and optionally include quality-of-life improvements such as the ability to view the movies of

the particles mid-simulation, as is offered in packages such as Smoldyn [115].

We have demonstrated that flicker spectroscopy is a powerful method to investigate stress granules in living cells in Chapter 4. The close agreement between our measurements with the estimated values in the literature, combined with our extensive simulations allow us to be confident in these results. We have also shown that we can distinguish between different treatments and transfected cells. Even though our own efforts to apply the method to more variants have been temporarily halted due to the pandemic, we are excited to see how it will be used in the community as stress granules are an area of great interest in the literature, and their anomalous formation has been linked to both aging and neuro-degenrative diseases [169, 62, 170].

There are several interesting potential avenues for future development in the method. We did not expect there to be a significant bending rigidity in stress granules, and while we have several conjectures, these need to be investigated experimentally. It is only in the last two years that other groups in the field have produced microscopy images of ternary structure within the stress granules, thanks to development in state-of-the-art tools such as STED, STORM [72] and expansion microscopy [67]. Therefore, it may be possible to investigate these potential candidates in-vivo using microscopy directly. It is currently unknown if this term is unique to stress granules or found in other biological compartments.

A great deal of information about droplet structure could also be gained from looking at the (temporal) frequency of the fluctuation modes. When there is no viscosity, the frequency follows a simple relation that depends on the nature of the forces binding the droplet. For instance, in a droplet dominated by surface tension, the frequency, ω_q, of the mode q is given by

$$\omega^2_{q,\mathrm{st}} = q(q-1)(q+2)\frac{\sigma}{\rho R^3} \ , \tag{5.0.1}$$

where ρ is the density of the droplet [171]. While, for a droplet with a bulk charge distribution, this is instead,

$$\omega^2_{q,\mathrm{charge}} = \frac{q(q-1)}{\rho R^3}\left[\sigma - \frac{3}{2}\frac{1}{(q+2)(2q+1)}\frac{kQ^2}{\pi R^3}\right] \ , \tag{5.0.2}$$

where Q is the total charge on the granule [172]. Likewise, we can also give an expected spectrum for a droplet where the charge is only distributed on the surface of the droplet

[173]. Then in a manner similar to the flicker spectroscopy method, we would measure an experimental frequency spectrum ω_q^2 and fit this against the spectra above to recover the most suitable spectrum and the best fit parameters. This approach is of particular interest to biological compartments, as it would allow us to probe the distribution negatively charged mRNA throughout the droplet. There also exists a spectrum for a droplet surrounded by a flexible layer [174, 129] that may give insight into the nature of the bending rigidity found in stress granules. Further, insight into the frequency spectrum of stress granules would allow us to make the corrections discussed in sec. 4.6.3 and remove a source of underestimation for the measured surface tension.

However, in the spectra given in eq. (5.0.1) and (5.0.2), there is an assumption that both the droplet and the surrounding medium are non-viscous, which is an inappropriate approximation for the cytoplasm of a cell and the introduction of this viscosity term *vastly* complicates the fluctuation spectrum. This problem was first studied by Chandrasekhar [175] and the resultant fluctuation spectrum is entirely non-trivial and must be solved numerically. Fortunately, Reid [176] showed the underlying spectra can be separated from the viscosity effect, and so—at least, in practice—it is still possible to distinguish the nature of the fluctuations.

We could also expand the pool of stress granules available for analysis, as currently a significant number of the granules we image prove unsuitable. This is mostly due to the restriction that we are only able to describe radial functions[1], as at this time we parameterise the surface as $S = R(1 + \sum_{l,m} Y_{lm}\mathcal{U}_{lm})$. Instead, we might define the surface using SPHARM, this is a parameterisation used in biophysics and medical imaging that can describe any arbitrary shape [177, 178, 179]. This gives the surface, $\vec{\mathbf{S}}$, as a function of two parameters v, w,

$$\vec{\mathbf{S}}(v,w) = \begin{pmatrix} x(v,w) \\ y(v,w) \\ z(v,w) \end{pmatrix} = \sum_{l=0}^{\infty} \sum_{m=-l}^{l} \begin{pmatrix} U^x_{l,m} \\ U^y_{l,m} \\ U^z_{l,m} \end{pmatrix} Y_{l,m} \ . \tag{5.0.3}$$

This means that instead of one set of perturbation magnitudes to describe the surface, $\mathcal{U}_{l,m}$, there are now three sets $(U^x_{l,m}, U^y_{l,m}, U^z_{l,m})$. This parameterisation is chosen as the energy of the surface can be given rather simply in terms of the of derivatives $\partial\vec{\mathbf{S}}\big/\partial v$, $\partial\vec{\mathbf{S}}\big/\partial w$ and the corresponding second order derivatives [167]. This would allow us to then construct an

1. Granules for which we can define a central point and describe all the surface as a singe radius, r as function of some angle φ, this rules out granule with any "overlap" for which there would be multiple values of r.

expression for the fluctuation energy as function of $(U^x_{l,m}, U^y_{l,m}, U^z_{l,m})$, analogous to eq. (4.1.6) which could then be fit against the experimental fluctuation spectrum of any arbitrary shape to measure its surface tension and bending rigidity. Care would still have to be taken with granules that are wetting onto a membrane or in the middle of merging event, however, as changes in the surface of these granules will likely not be dominated by fluctuations.

Granule explorer should prove to be a powerful tool for other groups that wish to investigate stress granules, and the flicker spectroscopy tools are general enough to be applied to any biological LLPS system of similar size or larger. Even if the user is not interested in flicker spectroscopy, the package can also be used to detect and categorise granules in still images without the complications of a more general image processing tools.

There was a surprising amount of difference between working code used for research in an individual group and a package to share with the community. This included ensuring that there was documentation and user interface suitable for users of all computational expertise. I believe the dual command line and web-based interface has achieved that, and the ability to track individual granules and diagnostic figures throughout the analysis has helped dramatically in our own debugging. Developing the package has also personally helped to enforce good programming practices such as test-driven development and continuous integration, to ensure that the software can be installed and run easily for other users.

In future, the software might also be expanded to cover the analysis of fluctuating vesicles as there is much of an overlap in both the theory and implementation. The two most significant changes would be to the boundary detection step and the experimental spectrum. Detecting the boundary of vesicles may be somewhat easier; vesicles are much typically much larger than biological LLPS systems and, unlike droplets, there is a well-defined surface that may be detected unambiguously, so an edge detection kernel will not have to be applied. The time-series fluctuations of vesicles are also much better understood, so corrections can be made to the experimental spectrum, for instance, to account for the blurring of the interface.

Chapter 6

Appendix

A Conventions

A.1 Spherical Coordinates

We use the convention more commonly seen in physics, as shown in fig. A.1, where $0 \geq \varphi > 2\pi$ is the longitude/azimuth angle and $0 \geq \theta > \pi$ is the altitude/inclination angle.

This gives a conversion between Cartesian and spherical coordinates as

$$x = r \sin\theta \cos\varphi \tag{A.1}$$

$$y = r \sin\theta \sin\varphi \tag{A.2}$$

$$y = r \cos\theta \ . \tag{A.3}$$

A.2 Spherical Harmonics

We define the *complex* spherical harmonics as

$$Y_l^m(\theta, \varphi) = N_l^m P_l^m(\cos\theta) e^{im\varphi} \ , \tag{A.4}$$

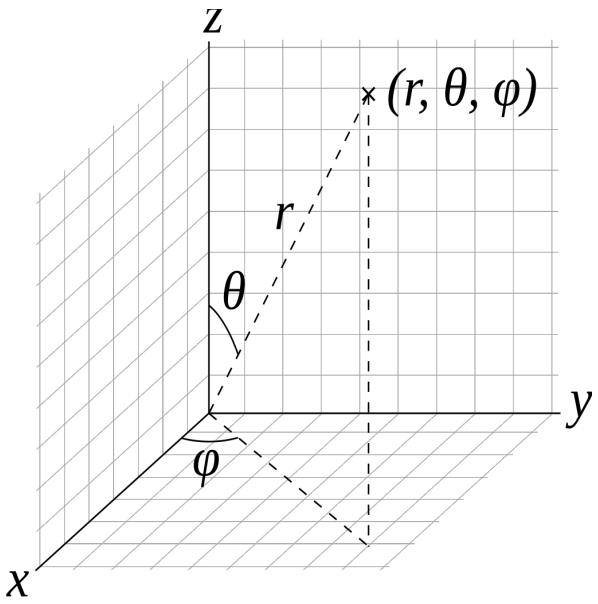

Figure A.1: Convention used for spherical harmonics. From [180]

with: P_l^m the associated Legendre polynomials with the Cordon-Shotley phase; $l \geq 0$ the degree of the spherical harmonics and $-l \geq m \geq l$ is the order of the spherical harmonic.

The normalisation is given by

$$N_l^m = \sqrt{\frac{2l+1}{4\pi}\frac{(l-m)!}{(l+m)!}} \ . \tag{A.5}$$

As we are primarily interested in real surfaces, we also make use of the real analogues of the spherical harmonics, Y_{lm}, defined to be,

$$Y_{lm} = \begin{cases} \sqrt{2}\,\mathrm{Im}\left[Y_l^{|m|}\right] & \text{if } m < 0 \\ Y_l^0 & \text{if } m = 0 \\ \sqrt{2}\,\mathrm{Re}\left[Y_l^m\right] & \text{if } m > 0 \ , \end{cases} \tag{A.6}$$

or equivalently,

$$Y_{lm} = \begin{cases} \sqrt{2}N_l^{|m|}P_l^{|m|}(\cos\theta)\sin(|m|\varphi) & \text{if } m < 0 \\ N_l^0 P_l^0(\cos\theta) & \text{if } m = 0 \\ \sqrt{2}N_l^m P_l^m(\cos\theta)\cos(m\varphi) & \text{if } m > 0 \ . \end{cases} \tag{A.7}$$

Bibliography

[1] Benjamin Wolozin and Pavel Ivanov. "Stress granules and neurodegeneration". In: *Nature Reviews Neuroscience* 20.11 (Nov. 2019), pp. 649–666.

[2] Marina Feric et al. "Coexisting Liquid Phases Underlie Nucleolar Subcompartments." In: *Cell* 165.7 (June 2016), pp. 1686–1697.

[3] Thoru Pederson. "The nucleolus". In: *Cold Spring Harbor Perspectives in Biology* 3.3 (Mar. 2011), pp. 1–15.

[4] Simon Alberti, Amy Gladfelter, and Tanja Mittag. *Considerations and Challenges in Studying Liquid-Liquid Phase Separation and Biomolecular Condensates*. Jan. 2019.

[5] A P Arrigo, J P Suhan, and W J Welch. "Dynamic changes in the structure and intracellular locale of the mammalian low-molecular-weight heat shock protein." In: *Molecular and Cellular Biology* 8.12 (Dec. 1988), pp. 5059–5071.

[6] U. Sheth. "Decapping and Decay of Messenger RNA Occur in Cytoplasmic Processing Bodies". In: *Science* 300.5620 (May 2003), pp. 805–808.

[7] Joseph G. Gall et al. "Assembly of the Nuclear Transcription and Processing Machinery: Cajal Bodies (Coiled Bodies) and Transcriptosomes". In: *Molecular Biology of the Cell* 10.12 (Dec. 1999). Ed. by Pam Silver, pp. 4385–4402.

[8] Salman F. Banani et al. "Biomolecular condensates: Organizers of cellular biochemistry". In: *Nature Reviews Molecular Cell Biology* 18.5 (2017), pp. 285–298.

[9] Clifford P Brangwynne et al. "Germline P granules are liquid droplets that localize by controlled dissolution/condensation." In: *Science (New York, N.Y.)* 324.5935 (June 2009), pp. 1729–32.

[10] C. P. Brangwynne, T. J. Mitchison, and A. A. Hyman. "Active liquid-like behavior of nucleoli determines their size and shape in Xenopus laevis oocytes". In: *Proceedings of the National Academy of Sciences* 108.11 (2011), pp. 4334–4339.

[11] Chiu Fan Lee et al. "Spatial organization of the cell cytoplasm by position-dependent phase separation". In: *Physical Review Letters* 111.8 (2013), pp. 1–5.

[12] Nancy Kedersha et al. "Stress granules and processing bodies are dynamically linked sites of mRNP remodeling". In: *Journal of Cell Biology* 169.6 (2005), pp. 871–884.

[13] Clifford P. Brangwynne. "Phase transitions and size scaling of membrane-less organelles." In: *The Journal of cell biology* 203.6 (2013), pp. 875–881.

[14] Paul Anderson and Nancy Kedersha. "Stressful initiations." In: *Journal of cell science* 115.Pt 16 (2002), pp. 3227–3234.

[15] Richard A. L. Jones. *Soft Condensed Matter*. Oxford University Press, 2002.

[16] Anthony A. Hyman, Christoph A. Weber, and Frank Jülicher. "Liquid-Liquid Phase Separation in Biology". In: *Annual Review of Cell and Developmental Biology* 30.1 (Oct. 2014), pp. 39–58.

[17] Louis Philippe Bergeron-Sandoval, Nozhat Safaee, and Stephen W. Michnick. "Mechanisms and Consequences of Macromolecular Phase Separation". In: *Cell* 165.5 (2016), pp. 1067–1079. arXiv: arXiv:1011.1669v3.

[18] Chih Yung S. Lee et al. "Recruitment of mRNAs to P granules by condensation with intrinsically-disordered proteins". In: *eLife* 9 (Jan. 2020).

[19] Andrea Putnam et al. "A gel phase promotes condensation of liquid P granules in Caenorhabditis elegans embryos". In: *Nature Structural and Molecular Biology* 26.3 (Mar. 2019), pp. 220–226.

[20] Yongdae Shin and Clifford P. Brangwynne. "Liquid phase condensation in cell physiology and disease". In: *Science* 357.6357 (Sept. 2017), eaaf4382.

[21] Kathrin Thedieck et al. "Inhibition of mTORC1 by astrin and stress granules prevents apoptosis in cancer cells". In: *Cell* 154.4 (Aug. 2013), pp. 859–874.

[22] Alex S. Holehouse and Rohit V. Pappu. "Functional Implications of Intracellular Phase Transitions". In: *Biochemistry* 57.17 (May 2018), pp. 2415–2423.

[23] John W. Cahn and John E. Hilliard. "Free Energy of a Nonuniform System. I. Interfacial Free Energy". In: *The Journal of Chemical Physics* 28.2 (Feb. 1958), pp. 258–267.

[24] Joel Berry et al. "RNA transcription modulates phase transition-driven nuclear body assembly". In: *Proceedings of the National Academy of Sciences* 112.38 (Sept. 2015), E5237–E5245. arXiv: arXiv:1404.2263v1.

[25] Elsen Tjhung, Cesare Nardini, and Michael E. Cates. "Cluster Phases and Bubbly Phase Separation in Active Fluids: Reversal of the Ostwald Process". In: *Physical Review X* 8.3 (Sept. 2018), p. 031080.

[26] Michael E. Cates and Elsen Tjhung. "Theories of binary fluid mixtures: From phase-separation kinetics to active emulsions". In: *Journal of Fluid Mechanics* 836 (Feb. 2018), P1. arXiv: 1806.01239.

[27] David Zwicker et al. "Centrosomes are autocatalytic droplets of pericentriolar material organized by centrioles". In: *Proceedings of the National Academy of Sciences* 111.26 (July 2014), E2636–E2645.

[28] Sonja Kroschwald et al. "Promiscuous interactions and protein disaggregases determine the material state of stress-inducible RNP granules". In: *eLife* 4.AUGUST2015 (Aug. 2015), pp. 1–32.

[29] Adriano Aguzzi and Matthias Altmeyer. "Phase Separation : Linking Cellular Compartmentalization to Disease". In: *Trends in Cell Biology* 26.7 (July 2016), pp. 547–558.

[30] Adva Aizer et al. "Quantifying mRNA targeting to P-bodies in living human cells reveals their dual role in mRNA decay and storage". In: *Journal of Cell Science* 127.20 (Oct. 2014), pp. 4443–4456.

[31] Nancy L. Kedersha et al. "RNA-binding proteins TIA-1 and TIAR link the phosphorylation of eIF-2 alpha to the assembly of mammalian stress granules." In: *The Journal of cell biology* 147.7 (Dec. 1999), pp. 1431–42.

[32] Woo Jae Kim et al. "Sequestration of TRAF2 into Stress Granules Interrupts Tumor Necrosis Factor Signaling under Stress Conditions". In: *Molecular and Cellular Biology* 25.6 (Mar. 2005), pp. 2450–2462.

[33] Kyoko Arimoto et al. "Formation of stress granules inhibits apoptosis by suppressing stress-responsive MAPK pathways". In: *Nature Cell Biology* 10.11 (Oct. 2008), pp. 1324–1332.

[34] M. Takahashi et al. "Stress Granules Inhibit Apoptosis by Reducing Reactive Oxygen Species Production". In: *Molecular and Cellular Biology* 33.4 (Feb. 2013), pp. 815–829.

[35] David W. Sanders et al. "Competing Protein-RNA Interaction Networks Control Multiphase Intracellular Organization". In: *Cell* 181.2 (Apr. 2020), 306–324.e28.

[36] Lutz Nover, Klaus-dieter Scharf, and Dieter Neumann. "Cytoplasmic Heat Shock Granules Are Formed from Precursor Particles and Are Associated with a Specific Set of mRNAs". In: *Mol Cell Biol.* 9.3 (1989), pp. 1298–1308.

[37] Joshua R Wheeler et al. "Distinct stages in stress granule assembly and disassembly". In: *eLife* 5.e18413 (Sept. 2016), pp. 1–25.

[38] Paul Anderson and Nancy Kedersha. "Stress granules: the Tao of RNA triage". In: *Trends in Biochemical Sciences* 33.3 (2008), pp. 141–150.

[39] Nancy Kedersha et al. "Evidence That Ternary Complex (eIF2-GTP-tRNA iMet)– Deficient Preinitiation Complexes Are Core Constituents of Mammalian Stress Granules". In: *Molecular Biology of the Cell* 13.January (2002), pp. 195–210.

[40] Rachid Mazroui et al. "Inhibition of ribosome recruitment induces stress granule formation independently of eukaryotic initiation factor 2α phosphorylation". In: *Molecular Biology of the Cell* 17.10 (2006), pp. 4212–4219.

[41] James P. White and Richard E. Lloyd. "Regulation of stress granules in virus systems". In: *Trends in Microbiology* 20.4 (2012), pp. 175–183.

[42] Nancy Kedersha and Paul Anderson. *Chapter 4 Regulation of Translation by Stress Granules and Processing Bodies*. Vol. 90. C. 2009, pp. 155–185.

[43] Mahdi Muhammad Moosa and Priya R. Banerjee. *Subversion of host stress granules by coronaviruses: Potential roles of π-rich disordered domains of viral nucleocapsids*. 2020.

[44] David E. Gordon et al. "A SARS-CoV-2 protein interaction map reveals targets for drug repurposing". In: *Nature* 583.7816 (July 2020), pp. 459–468.

[45] Natalie G Farny, Nancy L Kedersha, and Pamela a Silver. "Metazoan stress granule assembly is mediated by P-eIF2alpha-dependent and -independent mechanisms." In: *RNA (New York, N.Y.)* 15.10 (2009), pp. 1814–1821.

[46] Nancy Kedersha et al. "Dynamic shuttling of TIA-1 accompanies the recruitment of mRNA to mammalian stress granules". In: *Journal of Cell Biology* 151.6 (Dec. 2000), pp. 1257–1268.

[47] Hideaki Matsuki et al. "Both G3BP1 and G3BP2 contribute to stress granule formation." In: *Genes to cells : devoted to molecular & cellular mechanisms* 18.2 (Feb. 2013), pp. 135–46.

[48] Mariela Loschi et al. "Dynein and kinesin regulate stress-granule and P-body dynamics". In: (2009).

[49] Jordina Guillé N-Boixet et al. "RNA-Induced Conformational Switching and Clustering of G3BP Drive Stress Granule Assembly by Condensation Article RNA-Induced Conformational Switching and Clustering of G3BP Drive Stress Granule Assembly by Condensation". In: *Cell* 181 (2020), pp. 346–361.

[50] Natalie Gilks et al. "Stress granule assembly is mediated by prion-like aggregation of TIA-1". In: *Molecular Biology of the Cell* 15.12 (Dec. 2004), pp. 5383–5398.

[51] Amandine Molliex et al. "Phase Separation by Low Complexity Domains Promotes Stress Granule Assembly and Drives Pathological Fibrillization". In: *Cell* 163.1 (2015), pp. 123–133.

[52] Peipei Zhang et al. "Chronic optogenetic induction of stress granules is cytotoxic and reveals the evolution of ALS-FTD pathology". In: *eLife* 8 (Mar. 2019).

[53] Paul Anderson and Nancy Kedersha. *RNA granules: Post-transcriptional and epigenetic modulators of gene expression*. June 2009.

[54] Nancy Kedersha et al. "G3BP-Caprin1-USP10 complexes mediate stress granule condensation and associate with 40S subunits." In: *The Journal of cell biology* 212.7 (Mar. 2016), pp. 845–60.

[55] Gabriela Huelgas-Morales et al. "The Stress Granule RNA-Binding Protein TIAR-1 Protects Female Germ Cells from Heat Shock in Caenorhabditis elegans." In: *G3 (Bethesda, Md.)* 6.April (2016), pp. 1–71.

[56] Paul Anderson and Nancy Kedersha. "Visibly stressed: the role of eIF2, TIA-1, and stress granules in protein translation." In: *Cell stress & chaperones* 7.2 (Apr. 2002), pp. 213–21.

[57] Daisuke Ohshima et al. "Spatio-temporal Dynamics and Mechanisms of Stress Granule Assembly". In: *PLoS Computational Biology* 11.6 (2015), pp. 1–22.

[58] Hélène Tourrière et al. "The RasGAP-associated endoribonuclease G3BP assembles stress granules". In: *Journal of Cell Biology* 160.6 (Mar. 2003), pp. 823–831.

[59] Sebastian Markmiller et al. "Context-Dependent and Disease-Specific Diversity in Protein Interactions within Stress Granules". In: *Cell* 172.3 (2018), 590–604.e13.

[60] Hicham Mahboubi et al. "Identification of Novel Stress Granule Components That Are Involved in Nuclear Transport". In: *PLoS ONE* 8.6 (2013).

[61] Anaïs Aulas et al. "Stress-specific differences in assembly and composition of stress granules and related foci". In: *Journal of Cell Science* 130.5 (Mar. 2017), pp. 927–937.

[62] Xiuling Cao, Xuejiao Jin, and Beidong Liu. "The involvement of stress granules in aging and aging-associated diseases". In: *Aging Cell* (Mar. 2020).

[63] Alison B. Singer and Joseph G. Gall. "An inducible nuclear body in the Drosophila germinal vesicle". In: *Nucleus* 2.5 (Sept. 2011), pp. 403–409.

[64] David Andelman et al. "Structure and phase equilibria of microemulsions". In: *The Journal of Chemical Physics* 87.12 (Dec. 1987), pp. 7229–7241.

[65] Saumya Jain et al. "ATPase-Modulated Stress Granules Contain a Diverse Proteome and Substructure". In: *Cell* 164.3 (2016), pp. 487–498. arXiv: 1002.3888.

[66] S. Souquere et al. "Unravelling the ultrastructure of stress granules and associated P-bodies in human cells". In: *Journal of Cell Science* 122.20 (Oct. 2009), pp. 3619–3626.

[67] Davide Gambarotto et al. "Imaging cellular ultrastructures using expansion microscopy (U-ExM)". In: *Nature Methods* 16.1 (Jan. 2019), pp. 71–74.

[68] Fei Chen, Paul W. Tillberg, and Edward S. Boyden. "Expansion microscopy". In: *Science* 347.6221 (Jan. 2015), pp. 543–548.

[69] Luca Cirillo et al. "UBAP2L Forms Distinct Cores that Act in Nucleating Stress Granules Upstream of G3BP1". In: *Current Biology* 30.4 (Feb. 2020), 698–707.e6.

[70] Salman F. Banani et al. "Compositional Control of Phase-Separated Cellular Bodies". In: *Cell* 166.3 (July 2016), pp. 651–663.

[71] Nobuyuki Shiina. "Liquid- and solid-like RNA granules form through specific scaffold proteins and combine into biphasic granules". In: *Journal of Biological Chemistry* 294.10 (Mar. 2019), pp. 3532–3548.

[72] Hagai Marmor-Kollet et al. "Spatiotemporal Proteomic Analysis of Stress Granule Disassembly Using APEX Reveals Regulation by SUMOylation and Links to ALS Pathogenesis". In: *Molecular Cell* (Nov. 2020), p. 2020.01.29.830133.

[73] J. Ross Buchan and Roy Parker. "Eukaryotic Stress Granules: The Ins and Outs of Translation". In: *Molecular Cell* 36.6 (Dec. 2009), pp. 932–941.

[74] Avinash Patel et al. "A Liquid-to-Solid Phase Transition of the ALS Protein FUS Accelerated by Disease Mutation". In: *Cell* 162.5 (2015), pp. 1066–1077.

[75] Zachary Monahan, Frank Shewmaker, and Udai Bhan Pandey. "Stress granules at the intersection of autophagy and ALS". In: *Brain Research* 1649 (2016), pp. 189–200.

[76] Zachary M. March, Oliver D. King, and James Shorter. "Prion-like domains as epigenetic regulators, scaffolds for subcellular organization, and drivers of neurodegenerative disease". In: *Brain Research* 1647 (2016), pp. 9–18.

[77] Jaroslav Icha et al. "Phototoxicity in live fluorescence microscopy, and how to avoid it". In: *BioEssays* 39.8 (Aug. 2017), p. 1700003.

[78] Rayleigh. "XXXI. Investigations in optics, with special reference to the spectroscope". In: *The London, Edinburgh, and Dublin Philosophical Magazine and Journal of Science* 8.49 (Oct. 1879), pp. 261–274.

[79] E. Abbe. "Beiträge zur Theorie des Mikroskops und der mikroskopischen Wahrnehmung: I. Die Construction von Mikroskopen auf Grund der Theorie". In: *Archiv für mikroskopische Anatomie* 9.1 (Dec. 1873), pp. 413–418.

[80] Siân Culley et al. *SRRF: Universal live-cell super-resolution microscopy*. Aug. 2018.

[81] Rolf Theodor Borlinghaus and Constantin Kappel. "HyVolution—the smart path to confocal super-resolution". In: *Nature Methods* 13.3 (2018), pp. i–iii.

[82] Joseph Huff. "The Fast mode for ZEISS LSM 880 with Airyscan: high-speed confocal imaging with super-resolution and improved signal-to-noise ratio". In: *Nature Methods* 13.11 (2018), pp. i–ii.

[83] Eva Rittweger et al. "STED microscopy reveals crystal colour centres with nanometric resolution". In: 2009, p. 22.

[84] TA Klar. "Chpt 6. STED lithography and protein nanoanchors". In: *Optically Induced Nanostructures: Biomedical and Technical Applications*. De Gruyter, June 2015.

[85] Nobuyuki Otsu. "A Threshold Selection Method from Gray-Level Histograms". In: *IEEE Transactions on Systems, Man, and Cybernetics* 9.1 (Jan. 1979), pp. 62–66.

[86] Jui-Cheng Yen, Fu-Juay Chang, and Shyang Chang. "A new criterion for automatic multilevel thresholding". In: *IEEE Transactions on Image Processing* 4.3 (Mar. 1995), pp. 370–378.

[87] Siyue Chen et al. "Survey Over Image Thresholding Techniques". In: *J Electronic Imaging* 13.1 (Jan. 2004), p. 220.

[88] D. Marr and E. Hildreth. "Theory of edge detection". In: *Proceedings of the Royal Society of London. Series B. Biological Sciences* 207.1167 (Feb. 1980), pp. 187–217.

[89] Anaïs Aulas and Christine Vande Velde. "Alterations in stress granule dynamics driven by TDP-43 and FUS: A link to pathological inclusions in ALS?" In: *Frontiers in Cellular Neuroscience* 9.OCTOBER (Oct. 2015).

[90] L. C. Reineke et al. "Large G3BP-induced granules trigger eIF2 phosphorylation". In: *Molecular Biology of the Cell* 23.18 (Sept. 2012), pp. 3499–3510.

[91] Lucas C. Reineke and Joel R. Neilson. "Differences between acute and chronic stress granules, and how these differences may impact function in human disease". In: *Biochemical Pharmacology* 162.October 2018 (Apr. 2019), pp. 123–131.

[92] S Legros et al. "The HTLV-1 Tax protein inhibits formation of stress granules by interacting with histone deacetylase 6". In: *Oncogene* 30.38 (2011), pp. 4050–4062.

[93] D. M. Anderson, G. B. McFadden, and A. A. Wheeler. "DIFFUSE-INTERFACE METHODS IN FLUID MECHANICS". In: *Annual Review of Fluid Mechanics* 30.1 (Jan. 1998), pp. 139–165.

[94] Y. C. Li et al. "Phase-field simulation of thermally induced spinodal decomposition in polymer blends". In: *Modelling and Simulation in Materials Science and Engineering* 20.7 (Oct. 2012), p. 075002.

[95] John S. Lowengrub, Andreas Rätz, and Axel Voigt. "Phase-field modeling of the dynamics of multicomponent vesicles: Spinodal decomposition, coarsening, budding, and fission". In: *Physical Review E - Statistical, Nonlinear, and Soft Matter Physics* 79.3 (Mar. 2009), p. 031926.

[96] William M. Jacobs and Daan Frenkel. "Phase Transitions in Biological Systems with Many Components". In: *Biophysical Journal* 112.4 (Feb. 2017), pp. 683–691. arXiv: 1703.01223.

[97] Jeong Mo Choi, Alex S. Holehouse, and Rohit V. Pappu. *Physical Principles Underlying the Complex Biology of Intracellular Phase Transitions*. May 2020.

[98] Xiangze Zeng et al. "Connecting Coil-to-Globule Transitions to Full Phase Diagrams for Intrinsically Disordered Proteins". In: *Biophysical Journal* 119.2 (July 2020), pp. 402–418.

[99] Andrew T.R. Christy, Halim Kusumaatmaja, and Mark A. Miller. "Control of Superselectivity by Crowding in Three-Dimensional Hosts". In: *Physical Review Letters* 126.2 (Jan. 2021), p. 028002. arXiv: 2012.07111.

[100] Kazuhisa Ichikawa, Takashi Suzuki, and Noboru Murata. "Stochastic simulation of biological reactions, and its applications for studying actin polymerization". In: *Physical Biology* 7.4 (2010), p. 46010.

[101] Radek Erban and S Jonathan Chapman. "Stochastic modelling of reaction-diffusion processes: algorithms for bimolecular reactions." In: *Physical biology* 6.4 (2009), p. 046001. arXiv: 0903.1298.

[102] Lorenzo Dematté. "Parallel particle-based reaction diffusion: A GPU implementation". In: *Proceedings of the 9th Int. Workshop on Parallel and Distributed Methods in Verification, PDMC 2010 - Joint with the 2nd Int. Workshop on High Performance Computational Systems Biology, HiBi 2010* (2010), pp. 67–77.

[103] Johannes Schöneberg and Frank Noé. "ReaDDy–a software for particle-based reaction-diffusion dynamics in crowded cellular environments." In: *PloS one* 8.9 (2013), e74261.

[104] Szilárd Páll and Berk Hess. "A flexible algorithm for calculating pair interactions on SIMD architectures". In: *Computer Physics Communications* 184.12 (Dec. 2013), pp. 2641–2650. arXiv: 1306.1737.

[105] Lorenzo Dematte. "Smoldyn on Graphics Processing Units: Massively Parallel Brownian Dynamics Simulations". In: *Computational Biology and Bioinformatics, IEEE/ACM Transactions on* 9.3 (2012), pp. 655–667.

[106] S Green. "CUDA Particles". In: *NVIDIA Whitepaper* June (2007).

[107] G Morton. "A computer oriented geodetic data base and a new technique in file sequencing". In: 1966.

[108] C. Lauterbach et al. "Fast BVH construction on GPUs". In: *Computer Graphics Forum* 28.2 (Apr. 2009), pp. 375–384.

[109] Daryl Deford and Ananth Kalyanaraman. "Empirical analysis of space-Filling curves for scientific computing applications". In: *Proceedings of the International Conference on Parallel Processing*. Institute of Electrical and Electronics Engineers Inc., 2013, pp. 170–179.

[110] William Press et al. *Numerical Recipes: The Art of Scientific Computing*. Vol. 29. 4. 1987, p. 501.

[111] David Zwicker et al. "Growth and division of active droplets provides a model for protocells". In: *Nature Physics* 13.4 (2017), pp. 408–413. arXiv: 1603.01571.

[112] Elena S. Nadezhdina et al. "Microtubules govern stress granule mobility and dynamics". In: *Biochimica et Biophysica Acta (BBA) - Molecular Cell Research* 1803.3 (Mar. 2010), pp. 361–371.

[113] Konstantin G. Chernov et al. "Role of microtubules in stress granule assembly: Microtubule dynamical instability favors the formation of micrometric stress granules in cells". In: *Journal of Biological Chemistry* 284.52 (2009), pp. 36569–36580.

[114] Steven S. Andrews and Dennis Bray. "Stochastic simulation of chemical reactions with spatial resolution and single molecule detail". In: *Physical Biology* 1.3 (Oct. 2004), pp. 137–151.

[115] Steven S. Andrews. "Smoldyn: Particle-based simulation with rule-based modeling, improved molecular interaction and a library interface". In: *Bioinformatics* 33.5 (Mar. 2017), pp. 710–717.

[116] Stefan Wils. "STEPS: Modeling and simulating complex reaction-diffusion systems with Python". In: *Frontiers in Neuroinformatics* 3.JUN (June 2009), p. 15.

[117] J. R. Stiles et al. "Miniature endplate current rise times less than 100 microseconds from improved dual recordings can be modeled with passive acetylcholine diffusion from a synaptic vesicle." In: *Proceedings of the National Academy of Sciences* 93.12 (June 1996), pp. 5747–5752.

[118] Moritz Hoffmann, Christoph Fröhner, and Frank Noé. "ReaDDy 2: Fast and flexible software framework for interacting-particle reaction dynamics". In: *PLoS Computational Biology* 15.2 (Feb. 2019), e1006830.

[119] Johannes Schöneberg, Alexander Ullrich, and Frank Noé. "Simulation tools for particle-based reaction-diffusion dynamics in continuous space." In: *BMC biophysics* 7.1 (2014), p. 11.

[120] Alan Hammond, Mohammed Reza Yaghouti, and Fraydon Rezakhanlou. "Coagulation , Diffusion and the Continuous Smoluchowski Equation". In: (2009), pp. 1–42.

[121] Jonathan A.D. D Wattis. "An introduction to mathematical models of coagulation–fragmentation processes: A discrete deterministic mean-field approach". In: *Physica D: Nonlinear Phenomena* 222.1-2 (Oct. 2006), pp. 1–20.

[122] Jean David Wurtz and Chiu Fan Lee. "Stress granule formation via ATP depletion-triggered phase separation". In: *New Journal of Physics* 20.4 (Apr. 2018), p. 045008. arXiv: arXiv:1708.05697v3.

[123] David Zwicker, Anthony A. Hyman, and Frank Jülicher. "Suppression of Ostwald ripening in active emulsions". In: *Physical Review E - Statistical, Nonlinear, and Soft Matter Physics* 92.1 (2015), pp. 1–13.

[124] Jean David Wurtz and Chiu Fan Lee. "Chemical-Reaction-Controlled Phase Separated Drops: Formation, Size Selection, and Coarsening". In: *Physical Review Letters* 120.7 (Feb. 2018), p. 078102. arXiv: 1707.08433.

[125] Yousef Al-Kofahi et al. "A deep learning-based algorithm for 2-D cell segmentation in microscopy images". In: *BMC Bioinformatics* 19.1 (Oct. 2018), p. 365.

[126] Jean-Baptiste Lugagne, Haonan Lin, and Mary J. Dunlop. "DeLTA: Automated cell segmentation, tracking, and lineage reconstruction using deep learning". In: *PLOS Computational Biology* 16.4 (Apr. 2020). Ed. by Anand R. Asthagiri, e1007673.

[127] Marina Vietri et al. "Unrestrained ESCRT-III drives micronuclear catastrophe and chromosome fragmentation". In: *Nature Cell Biology* 22.7 (July 2020), pp. 856–867.

[128] George Marsaglia. "Choosing a Point from the Surface of a Sphere". In: *The Annals of Mathematical Statistics* 43.2 (Apr. 1972), pp. 645–646.

[129] L.E. Scriven and C.V. Sternling. "On cellular convection driven by surface-tension gradients". In: *Journal of Fluid Mechanics* (1964), p. 321.

[130] Tiemei Lu and Evan Spruijt. "Multiphase Complex Coacervate Droplets". In: *Journal of the American Chemical Society* 142.6 (Feb. 2020), pp. 2905–2914.

[131] Priya R. Banerjee et al. "Reentrant Phase Transition Drives Dynamic Substructure Formation in Ribonucleoprotein Droplets". In: *Angewandte Chemie - International Edition* 56.38 (2017), pp. 11354–11359.

[132] Dirk G.A.L. A L Aarts, Matthias Schmidt, and Henk N.W. W Lekkerkerker. "Direct Visual Observation of Thermal Capillary Waves". In: *Science* 304.5672 (May 2004), pp. 847–850.

[133] Mohamed Daoud and Claudine E. Williams. *Soft Matter Physics*. Springer Science & Business Media, 2013, 1999.

[134] L. I. Daikhin, A. A. Kornyshev, and M. Urbakh. "Capillary waves at soft electrified interfaces". In: *Journal of Electroanalytical Chemistry* 483.1 (Mar. 2000), pp. 68–80.

[135] Louise M. Jawerth et al. "Salt-Dependent Rheology and Surface Tension of Protein Condensates Using Optical Traps". In: *Physical Review Letters* 121.25 (Dec. 2018), p. 258101. arXiv: 1809.09832.

[136] Markus Deserno. "Fluid lipid membranes – a primer". In: *See https://www.cmu.edu/biolphys/deserno/pdf/membrane_* (2007), pp. 1–29.

[137] Markus Deserno. "Fluid lipid membranes: From differential geometry to curvature stresses". In: *Chemistry and Physics of Lipids* 185 (Jan. 2015), pp. 11–45.

[138] S. A. Safran. "Fluctuations of spherical microemulsions". In: *The Journal of Chemical Physics* 78.4 (1983), pp. 2073–2076.

[139] W. Häckl, U. Seifert, and E. Sackmann. "Effects of Fully and Partially Solubilized Amphiphiles on Bilayer Bending Stiffness and Temperature Dependence of the Effective Tension of Giant Vesicles". In: *Journal de Physique II* 7.8 (Aug. 1997), pp. 1141–1157.

[140] H. Engelhardt, H.P. Duwe, and E. Sackmann. "Bilayer bending elasticity measured by Fourier analysis of thermally excited surface undulations of flaccid vesicles". In: *Journal de Physique Lettres* 46.8 (1985), pp. 395–400.

[141] E. Becker, W. J. Hiller, and T. A. Kowalewski. "Experimental and theoretical investigation of large-amplitude oscillations of liquid droplets". In: *Journal of Fluid Mechanics* 231.-1 (Oct. 1991), p. 189.

[142] J. Pécréaux et al. "Refined contour analysis of giant unilamellar vesicles". In: *The European Physical Journal E* 13.3 (Mar. 2004), pp. 277–290.

[143] Ken Shoemake. "Animating rotation with quaternion curves". In: *ACM SIGGRAPH Computer Graphics* 19.3 (July 1985), pp. 245–254.

[144] P. Szendro, G. Vincze, and A. Szasz. "BIO-RESPONSE TO WHITE NOISE EXCITATION". In: *Electro- and Magnetobiology* 20.2 (Jan. 2001), pp. 215–229.

[145] Per Bak, Chao Tang, and Kurt Wiesenfeld. "Self-organized criticality". In: *Physical Review A* 38.1 (1988), pp. 364–374. arXiv: 2003.08130.

[146] Alexander Belyaev. "On Implicit Image Derivatives and Their Applications". In: British Machine Vision Association and Society for Pattern Recognition, Oct. 2011, pp. 72.1–72.12.

[147] Bernd Jähne, Horst Haußecker, and Peter Geißler. *Handbook of computer vision and applications*. Citeseer, 1999.

[148] Hany Farid and Eero P. Simoncelli. "Optimally rotation-equivariant directional derivative kernels". In: 1997, pp. 207–214.

[149] D Kroon. "Numerical optimization of kernel based image derivatives". In: *Short Paper University Twente* (2009).

[150] Johannes Schindelin et al. "Fiji: an open-source platform for biological-image analysis". In: *Nature Methods* 9.7 (July 2012), pp. 676–682.

[151] David Wales. *Energy Landscape*. Cambridge University Press, 2004.

[152] Curtis T. Rueden et al. "ImageJ2: ImageJ for the next generation of scientific image data". In: *BMC Bioinformatics* 18.1 (Dec. 2017), p. 529.

[153] Anne E Carpenter et al. "CellProfiler: image analysis software for identifying and quantifying cell phenotypes." In: *Genome biology* 7.10 (2006), R100.

[154] Laura D. Jennings-Antipov and Timothy S. Gardner. "Digital publishing isn't enough: the case for 'blueprints' in scientific communication". In: *Emerging Topics in Life Sciences* 2.6 (Dec. 2018), pp. 755–758.

[155] J. Koster and S. Rahmann. "Snakemake–a scalable bioinformatics workflow engine". In: *Bioinformatics* 28.19 (Oct. 2012), pp. 2520–2522.

[156] S. Alex Rautu et al. "The role of optical projection in the analysis of membrane fluctuations". In: *Soft Matter* 13.19 (Nov. 2017), pp. 3480–3483. arXiv: 1511.05064.

[157] Christina M. Caragine, Shannon C. Haley, and Alexandra Zidovska. "Surface Fluctuations and Coalescence of Nucleolar Droplets in the Human Cell Nucleus". In: *Physical Review Letters* 121.14 (2018), p. 148101.

[158] Robert W. Style et al. "Liquid-Liquid Phase Separation in an Elastic Network". In: *Physical Review X* 8.1 (Feb. 2018), p. 011028. arXiv: 1709.00500.

[159] P. Méléard et al. "Pulsed-light microscopy applied to the measurement of the bending elasticity of giant liposomes". In: *Epl* 19.4 (1992), pp. 267–271.

[160] Sriram Ramaswamy. "Equilibrium and non-equilibrium dynamics of the dilute lamellar phase". In: *Physica A: Statistical Mechanics and its Applications* 186.1-2 (1992), pp. 154–159.

[161] Ming Guo et al. "Probing the Stochastic, Motor-Driven Properties of the Cytoplasm Using Force Spectrum Microscopy". In: *Cell* 158.4 (Aug. 2014), pp. 822–832.

[162] Clifford P. Brangwynne, F. C. MacKintosh, and David A. Weitz. "Force fluctuations and polymerization dynamics of intracellular microtubules". In: *Proceedings of the National Academy of Sciences* 104.41 (Oct. 2007), pp. 16128–16133.

[163] Julia Penso and Rivka Beitner. "Clotrimazole and bifonazole detach hexokinase from mitochondria of melanoma cells". In: *European Journal of Pharmacology* 342.1 (Jan. 1998), pp. 113–117.

[164] J. Ross Buchan, J.-H. Yoon, and Roy Parker. "Stress-specific composition, assembly and kinetics of stress granules in Saccharomyces cerevisiae". In: *Journal of Cell Science* 124.2 (Jan. 2011), pp. 228–239.

[165] Udo Seifert. *Configurations of fluid membranes and vesicles*. Vol. 46. 1. 1997, pp. 13–137. arXiv: 9809043v1 [arXiv:cond-mat].

[166] Udo Seifert. "Configurations of fluid membranes and vesicles". In: *Advances in Physics* 46.1 (Feb. 1997), pp. 13–137.

[167] Ou Yang Zhong-Can and Wolfgang Helfrich. "Bending energy of vesicle membranes: General expressions for the first, second, and third variation of the shape energy and applications to spheres and cylinders". In: *Physical Review A* 39.10 (1989), pp. 5280–5288.

[168] Bengt Fornberg. "Generation of finite difference formulas on arbitrarily spaced grids". In: *Mathematics of Computation* 51.184 (1988), pp. 699–699.

[169] Tara Vanderweyde et al. "The Role Stress Granules and RNA Binding Proteins in Neurodegeneration". In: 59.6 (2013), pp. 1–13.

[170] Simon Alberti and Anthony A. Hyman. "Are aberrant phase transitions a driver of cellular aging?" In: *BioEssays* 38.10 (2016), pp. 959–968.

[171] Horace Lamb. "Hydrodynamics". In: 6th ed. Cambridge: at the University Press, 1993, p. 495.

[172] Niels Bohr and John Archibald Wheeler. "The mechanism of nuclear fission". In: *Physical Review* 56.5 (1939), pp. 426–450.

[173] Fang Li, Xie Yuan Yin, and Xie Zhen Yin. "Small-amplitude shape oscillation and linear instability of an electrically charged viscoelastic liquid droplet". In: *Journal of Non-Newtonian Fluid Mechanics* 264.September 2018 (2018), pp. 85–97.

[174] C. A. Miller and L. E. Scriven. "The oscillations of a fluid droplet immersed in another fluid". In: *Journal of Fluid Mechanics* 32.3 (1968), pp. 417–435.

[175] S. Chandrasekhar. "The Oscillations of a Viscous Liquid Globe". In: *Proceedings of the London Mathematical Society* s3-9.1 (Jan. 1959), pp. 141–149.

[176] W. H. Reid. "The oscillations of a viscous liquid drop". In: *Quarterly of Applied Mathematics* 18.1 (Apr. 1960), pp. 86–89.

[177] Christel Ducroz, Jean Christophe Olivo-Marin, and Alexandre Dufour. "Characterization of cell shape and deformation in 3D using Spherical Harmonics". In: *Proceedings - International Symposium on Biomedical Imaging*. IEEE, May 2012, pp. 848–851.

[178] Moo K. Chung et al. "Encoding cortical surface by spherical harmonics". In: *Statistica Sinica* 18.4 (2008), pp. 1269–1291.

[179] M. K. Chung et al. "Model building in two-sphere via Gauss-Weierstrass kernel smoothing and its application to cortical analysis, part II". In: *Technical Reprot* 1116 (2005).

[180] Andeggs. *3D Spherical.svg*. 2019.